Development of a Practical Electrical Tomography System for Flexible Contact Sensing Applications

University of Salford MANCHESTER

Stefania Russo
University of Salford

Submitted in partial fulfilment
of the requirements for the degree of
Doctor of Philosophy

School of Computing, Science & Engineering
Autonomous Systems and Robotics

March 2018

Contents

List of Publications

The content of this thesis builds on and extends the work presented in the following publications by the author:

Journal Papers

- Stefania Russo, Samia Nefti-Meziani, Nicola Carbonaro, Alessandro Tognetti. "Development of a High-Speed Current Injection and Voltage Measurement System for EIT-based Stretchable Sensors", Technologies, 2017. (172) **Journal cover image**

- Stefania Russo, Samia Nefti-Meziani, Nicola Carbonaro, Alessandro Tognetti. "A Quantitative Evaluation for Dynamically Optimizing Drive Patterns Selection in EIT-based Stretchable Sensors", Sensors, 2017. (173)

- Stefania Russo, Roy Assaf, Nicola Carbonaro, Alessandro Tognetti. "A Discriminant Analysis Classification approach for a Flexible Sensor based on Electric Tomography". **In preparation**

Papers in Peer-Reviewed Conferences

- Stefania Russo, Nicola Carbonaro, Alessandro Tognetti, Samia Nefti-Meziani. "A Quantitative Evaluation of Drive Patterns in Electrical Impedance Tomography", International Conference on Wireless Mobile Communication and Healthcare, Mobihealth, 2016. (170)

- Stefania Russo, Samia Nefti-Meziani, Gulrez T., Carbonaro N., Tognetti A. "Towards the Development of an EIT-based Stretchable Sensor for Multi-Touch Industrial Human-Computer Interaction Systems", Human-Computer Interaction International Conference, 2016. (171)

Other publications by the author outside the scope of this thesis:

List of Figures

List of Tables

List of Algorithms

Acknowledgements

I want to express my gratitude to my supervisors, Dr. Theo Theodoridis and Prof. Samia-Nefti Meziani for giving me the chance to be part of this great European project over the last three years. Also, I want to thank very much Prof. Alessandro Tognetti and Dr. Nicola Carbonaro for their the help and encouragement, that made possible the development of many aspects of this work, and especially Alessandro who have guided me during various stages of this research.
I also want to thank my close friends and colleagues Saber, Alex and Roy. You have been a very important part of this long journey. And Ipek, thanks for your sincere friendship, I will really miss you.
Roy, there are no words to describe how grateful I am to have met you. Thanks for your help in the last stages of the PhD, and especially for always being a constant source of support and encouragement for my continuous improvements.
Carolina, a special mention goes to you, my dear friend since university, who gave me the inspiration to start this PhD and the motivation to keep working in the hard times. I am waiting for a new "back together".
Francesca, my favourite franchiddese, thanks for always showing me your enthusiasm and for making me always smile. Your friendship means very much.
Thanks to Pani and Shireen, it was amazing to have you next door, and I am looking forward to see you again very soon.
A big thank to all the Smart-es which have been part of this three-years project adventure. I have enjoyed our meetings and summer schools. This PhD would have not been the same without you. Lisa, a big thank for being a great part of the team, even if for a short period. You have brought happiness and smiles into the last months of this project.
At last but not at least, I want to thank my parents, Titti and Tonino. Grazie per il vostro amore costante, e per esserci sempre, come genitori e amici. Grazie per avermi constantemente spinta a credere in me stessa. Grazie per aver sempre messo la mia felicità al primo posto senza mai chiedere nulla in cambio.

Abbreviations and Notations

	Abbreviations
AC	Alternate Current
AoS	Academy of Sciences
AD	Adjacent Protocol
ADC	Analog to Digital Converter
AEE	Average Euclidean Error
AI	Artificial Intelligence
ANN	Artificial Neural Network
BVC	Boundary Voltage Change
CMRR	Common Mode Rejection Ratio
CNF	Carbon Nano-Fibre
CNN	Convolutional Neural Network
DAC	Digital to Analog Converter
DAQ	Data Acquisition
DC	Direct Current
DNN	Deep Neural Network
DSO	Detected Size of Object
ECT	Electrical Capacitance Tomography
EIDORS	Electrical Impedance and Diffuse Optical Reconstruction Software
EIT	Electrical Impedance Tomography
ERT	Electrical Resistance Tomography
FDM	Frequency-Division Multiplexing

FE	Finite Element
FFT	Fast Fourier Transform
FIR	Finite Impulse Response
FT	Fourier Transform
HMM	Hidden Markov Models
I/O	Input/Output
IFT	Inductive Flow Tomography
IIR	Infinite Impulse Response
LDA	Linear Discriminant Analysis
MAD	Mean Absolute Deviation
MIT	Magnetic Impedance Tomography
ML	Machine Learning
MWT	Microwave Tomography
NoB	Number of Bits
NOSER	Newton's One-Step Error Reconstructor Prior
Opamp	Operational Amplifier
PCA	Principal Component Analysis
PCB	Printed Circuit Board
PDIPM	Primal-Dual Interior Point Method
PE	Position Error
PGIA	Programmable Gain Instrumentation Amplifier
PP	Pseudo Polar Protocol
PP-PP	Pseudo Polar-Pseudo Polar Protocol
PPy	Polypyrrole
PSO	Particle Swarm Optimisation
PVDF	Polyvinylidene Fluoride
QDA	Quadratic Discriminant Analysis
RLS	Regularised Least Square
RNG	Ringing
ROI	Region of Interest

RTIL	Room Temperature Ionic Liquid
SE	Size Error
SEM	Scanning Electron Microscope
SIFT	Scale Invariant Feature Transformation
SNR	Signal to Noise Ratio
SO	Size Object
SOM	Self Organising Map
STFT	Short Time Fourier Transform
SVM	Support Vector Machine
UST	Ultrasound Tomography
WMS	Wire Mesh Tomography

Notations

C	capacitance
ϵ_0	free space permittivity
ϵ_r	relative permittivity
A	area of a capacitor
d	distance between the plates of the capacitor
ϵ_{top}	strain on the top surface
R	radius of a cylinder
d_{sens}	thicknesses of sensing layer
d_{subs}	thicknesses of substrate
Y_{sens}	Young's moduli of sensing layer
Y_{subs}	Young's moduli of substrate
V_{ref}	reference voltage
$Load$	load
I_l	current supplied to the load
L	number of electrodes
S	collected samples

V^b	vector containing the raw samples
K	number of boundary measurements
sk	skipping factor
V_m	final voltage data set vector
k_{select}	logical vector for selecting boundary measurements
t_s	number of transient samples
Ω	electrical conductive body
σ	electrical conductivity
ϕ	scalar potential
$\mathbf{E}$	electric field
V_l	potential at generic l'th electrode
z_l	contact impedance
$\mathbf{n}$	unit normal
$F(\sigma)$	conductivity distribution to be recovered
$F(.)$	forward operator
σ_0	initial conductivity estimation
δV	variation in the measured potentials
J	Jacobian matrix
α	hyperparameter
R	regularisation matrix
$(\hat{x}_O)$	image of the conductivity changes
$[\hat{x}_O]_i$	image pixel values
$\hat{x}_P$	processed image
$[\hat{x_P}]_i$	pixel values of the processed image
$E[V_i]$	mean of multiple measurements
$Var(V_i)$	variance between measurements
A_{CM}	area of conductive medium
r_r	real position of the object
r_d	estimated position of the object
C	total number of classes

c	generic touch position class
X	generic data observation
p	number of features
μ_c	mean vector
Σ_c	covariance matrix
n_c	number of observations in each class
n	total number of observations in the training data
$Pr(Y\|X)$	posterior probability
Y	random variable
S_{num}	number of scans per test
T	number of tests
S_{sub}	constant used for dividing samples into sub sections
tr	true class
n_{pc}	number of predictions per each class
d	euclidean distance
d_c	distance to the boundary electrodes

Abstract

Tactile sensing is seeing an increase in potential applications, such as in humanoid and industrial robots; health care systems and medical instrumentation; prosthetic devices; and in the context of human-machine interaction. However, these applications require the integration of tactile sensors over various objects with different surface shapes. This emphasises the need of developing sensors which are flexible in contrast with the common rigid type. Moreover, flexible sensing research is considered to be in its infancy. Many technological and system issues are still open, mainly: conformability; scalability; system integration; high system cost; sensor size; and power consumption.

In light of the above, this thesis is concerned with the development of a flexible fabric-based contact sensor system. This is done through an interdisciplinary approach whereby electronics, system engineering, electrical tomography, and machine learning have been considered. This results in a practical flexible sensor that is capable of accurately detecting contact locations with high temporal resolution; and requires low power consumption. The sensor is based on the principle of electrical tomography. This is essential since this technique allows us to eliminate electrodes and wiring from within the sensing area, confining them to the periphery of the sensor. This improves flexibility all while eliminating electrode fatigue and deterioration due to repeated loading. We start by developing an electrical tomography sensor system. This comprises of a piezoresistive flexible fabric material, a data acquisition card, and a custom printed circuit board for managing both current injection and data collection. We show that current injection and voltage measurement protocols respond differently to different positions of the input contact region of interest, consequently affecting the overall performance of the tomography sensor system. Then, an approach for classifying contact location over the sensor is presented. This is done using supervised machine learning, namely discriminant analysis. Accurate touch location identification is achieved, along with an increase in the detection speed and sensor

versatility. Finally, the sensor is placed over different surfaces in order to show and validate its efficiency.

The main finding of this work is that electrical tomography flexible sensor systems present a very promising technology, and can be practically and effectively used for developing inexpensive and durable flexible sensors for tactile applications. The main advantage of this approach is the complete absence of wires in the internal area of the sensor. This allows the sensor to be placed over surfaces with different shapes without losing its functionality. The sensor's applicability can be further improved by using machine learning strategies due to their ability of empirical learning and extracting meaningful tactile information.

The research work in this thesis was motivated by the problems faced by industrial partners which were part of the sustainable manufacturing and advanced robotics training network in Europe (SMART-e).

Chapter 1

Introduction

Contents

1.1 Motivation

We experience the world around us by interacting with it using our senses. These allow us to see, hear, smell, taste, and touch. Among these various sensory modalities, tactile (touch) sensing assists us by providing an effective communication channel for the exploration and manipulation of objects. Unlike the other senses, which are located at specific body parts, touch is a sense that is spread all over the human body. Furthermore, touch plays an important role in enhancing our social interactions (66). In the book "Touch" (63), Fields argues that "touch is ten times stronger than verbal or emotional contact...touch is not only basic to our species, but the key to it".

In recent times we have become accustomed to living in a society where we are constantly interacting with several artificial systems. These assist us in our daily lives and range from everyday apparatus, to medical devices, and more recently robotic systems. However, for these devices to ubiquitously co-exist with humans, interact safely, cooperate and communicate, they need to "weave themselves into the fabric of everyday life" as Mark Weiser envisioned more than two decades ago (213). Since then, the research community has developed a great interest in this idea. This can be seen in the research on wearable and ubiquitous computing (71, 131, 36); internet of things (78, 211); in augmented reality (20); and contact sensors (24). Nonetheless, effort is still being made to bring a smooth integration of interactivity into devices that are already out there, and that were initially not meant to be interactive (152, 217, 161).

Within the vision presented above, and inspired by the way humans interact with the world through the sense of touch, we can deduce that it is desirable that artificial devices possess some kind of tactile sensation. This would enable them to interact and merge intelligently with humans (188). This idea is further confirmed by the particular interest shown by the research community in the development and integration of tactile sensors for this purpose in the last years (47, 110).

Yet the way these sensors are meant to be embedded within the physical systems is still a challenging task. This aspect would indeed dictate the overall performance of the final system. In fact, conventional rigid sensing technologies are very difficult, if not impossible, to shape around their host system. Also, these tend to become increasingly vulnerable in the case of host movements, risking system failure. These disadvantages become more serious when considering safety issues,

and incur additional maintenance costs.
Therefore, compared to traditional rigid sensors, recent advancements have appeared in flexible/stretchable sensors. These are potentially easy to integrate into different surfaces, and can be highly compliant with the host system, while still providing good impact resistance, a reduction in costs, and tolerance to strains (208).
For instance, let us consider the recent demand for service and industrial robots which are capable of autonomously operating in unstructured environments alongside humans (97, 49) (i.e. rehabilitation and assistive robots, medical robots, humanoid robots, and general purpose robots). For such robots it is necessary to have a tactile, or at least a touch sensing ability in order for them to have special capabilities (190, 57), such as interpreting and understanding human intentions. This can be provided by large area flexible patches or whole–body contact sensing devices (126, 100, 51). For example, in (157) a contact sensor for application on robotic fingers of a prosthetic hand is presented.
In medical application, contact sensors have been developed in recent years to enhance the quality of interactions with patients. One example is in the context of palpation and probing devices. A review of these can be found in (106).
Another example is found in interactive textiles that are responsive to touch and other inputs from humans. Recently, Google is showing interest in developing Jacquard (162), a technology in which novel textile materials are woven into clothes to create human-responsive soft toys, furniture and clothes.
However, existing flexible contact sensor prototypes often present low accuracy and reliability, which makes it difficult to effectively utilise them in many tasks. Also, the presence of many internal structures (i.e. wires, flexible printed circuit boards (PCBs)) withing the sensing area still makes them difficult to integrate without interfering seamlessly with the host's mechanics (47). An overview of the most important tactile sensing requirements can be seen in Table 1.1.

With the above in mind, the work presented in this thesis aims to contribute to this field by paving the way for the development of a flexible contact fabric sensor system that can be practical, widely used, and easy to customise. Fabrics are in fact low-cost, extremely flexible, bendable and conformable, and can provide with a natural feeling when placed over different materials, which improves their integration.
The sensor presented in this work can be used to accurately detect contact location, has low power consumption, and provides high temporal resolution of touch

Task	Mechanical	Electrical	Engineering Others
Contact Force	Conformability	Transduction Principle	Manufacturability
Contact Location	Flexibility	Power Consumption	Maintenance
Direction and Distribution of Force	Stretchability	Communication Systems	Reliability
Contact Image	Sensor Distribution	Data Acquisition	Costs
Temperature	Sensor Number	Local Computation	Data Representation
Spatial and Temporal Resolution	Weight	Data Transfer	Sensor Fusion

Table 1.1: An overview of tactile sensors requirements

information. Also, aspects regarding the practical implementation and customisation of the sensor are addressed with the aim of providing a framework that eases the usage of this sensor.

The sensor is based on the principle of electrical tomography. This technique allows us to eliminate electrodes and wiring from within the sensing area, confining them to the sensor's periphery. It also allows for improved flexibility, and a more robust design whereby electrode fatigue and degradation due to repeated loading is eliminated. This is expected to improve the overall life cycle performance of the transducer. However, reconstructing touch inputs from measurements taken at the boundary represents a challenge for achieving good performance using the developed sensor system. Intelligent strategies for extracting contact information are therefore required and also addressed in this thesis.

The main contributions of the work presented in this thesis are summarised in the next section.

1.2 Main Contribution

In this thesis we present a number of contributions to the field of contact sensing. These can be summarised by the following: the development of a system for practical electrical tomography sensors; a study on optimal current injection

and voltage measurement protocols, which aims at improving the performance of tomography sensors; and classification of the position of touch inputs over the sensor using supervised machine learning. The key contributions are presented in further detail next.

1.2.1 Electrical Tomography Sensor System

Electrical tomography is an imaging technique that is mainly used for medical applications. The principle is to measure the internal conductivity distribution of a body through measurements taken only at its boundary. Although there exists a number of hardware systems for electrical tomography imaging, few of these are specific to contact sensor application and yet do not address all the requirements for practical contact sensors which are: simple and low-cost hardware, high temporal resolution; precise and consistent measurements.
Therefore, we propose to address all these requirements by developing an electrical tomography sensor system along with all its elements: a custom Printed Circuit Board (PCB) for performing adjustable current injection and voltages measurements; data acquisition setup and multiplexing; and the transducer element. The design and development of the system along with its results are detailed in Chapter 3.

1.2.2 Optimal Current Injection and Voltage Measurement Protocol based on the Region of Interest

A common issue in electrical tomography systems is their low spatial resolution. With particular attention to fabric sensors, in this work we contribute in overcoming this drawback by showing that protocols respond differently to different positions of the Region Of Interest (ROI). This behaviour consequently affects the overall performance of the electrical tomography sensor system. This is shown through a comparative study on the performance of a novel type of protocol and two other commonly used protocols, with regards to different ROI locations. The response of the protocols is evaluated using performance metrics that were obtained from data generated using simulation, and our sensor system from Chapter 3.
We conclude this chapter by suggesting a practical approach for future works,

where we propose to dynamically switch between different protocols following the identification of the ROI on the sensor. This work and its results are presented in Chapter 4.

1.2.3 Touch Position Identification using Discriminant Analysis

Electrical tomography techniques present drawbacks such as high sensitivity to noise, that jeopardise the applicability aspect and wide use of flexible contact sensors. As a consequence, although electrical tomography fabric sensors are ideally supposed to be easy to shape and applied over different surfaces, they are in reality difficult to be implemented in a real world scenario.
To address this limitation, in Chapter 5 we present a method for touch position identification for an electrical tomography flexible contact sensor. This is done by using a supervised machine learning algorithm for performing classification, namely discriminant analysis. This approach provides accurate contact location identification, increasing the detection speed and the sensor versatility when compared to traditional tomography approaches. Furthermore, we propose a novel data collection process for robust training of the learning algorithm. Finally, driven by the aim of proving a framework for a practical and versatile sensor, we present a detailed study on how the system performance are dependent from parameters as: number of training data; number of electrodes; dimension of the sensor; and distance of the touch input from the electrodes. The sensor is then applied in real case scenarios over different surfaces to show and validate its efficiency.

1.3 Thesis Outline

Having highlighted the purpose and scope of the thesis, the next chapter provides the introductory concepts and a literature review on flexible tactile and contact sensors with their mechanical, electrical and data managements aspects. This is followed by a literature review on fabric sensors, and their implementation for tactile sensing applications. Electrical tomography is then presented along with a literature on electrical tomography sensors. Finally, an overview on machine learning approaches in tactile sensing applications is presented.

The contents of Chapters 3, 4, 5 consist of the main body of the thesis,

the details of the previously mentioned contributions are herein presented. These chapters begin with a chapter summary and end with a discussion around the obtained results.

Chapter 3 presents our hardware design and methodology approach for the development of an electrical tomography sensor system.

In Chapter 4, we study optimal current injection and voltage measurement protocols based on the position of a contact region of interest. The chapter includes a study on a novel type of current injection and voltage measurement protocol and performance metrics used for evaluating the system's performance. For this work we use the platform developed in Chapter 3 which allows us to study the system in different configurations.

In Chapter 5 we present our method for touch position identification over our electrical tomography flexible contact sensor based on discriminant analysis. This is followed by an analysis of the results.

Finally, Chapter 6 concludes the thesis and discusses the findings and limitations of this work, and proposes future directions for research on flexible tactile sensors.

Chapter 2

Background

Contents

2.1 Chapter Summary

This chapter reviews the concepts and literature that are relevant to the work presented in this thesis.

We start with a general overview of the field of flexible tactile and contact sensing technologies. Here we cover their requirements and the different approaches used in the field. This is followed by a literature review and discussion on piezoresistive fabric sensors, their manufacturing process, and their implementation for tactile and contact sensing applications. Subsequently, we present electrical tomography imaging and its system architecture, along with an extensive literature review on recent works in electrical tomography tactile sensors. Finally, an overview of machine learning approaches is also provided with particular focus on their utilisation in tactile sensing and electrical tomography applications.

2.2 Flexible Tactile Sensors

Among the various sensing modalities, tactile (touch) sensing is particularly important since it is the link that enables physical contact with objects. Through tactile and contact sensing, we can explore the properties of the physical world surrounding us (210). Also, social interactions are strengthened through touch (66).

The human organ responsible for the sense of touch is the skin. This is the largest organ in our body, since the sense of touch is not located at any specific position but is spread all over our body. Our sense of touch is controlled by a complex network of nerve endings and sensory receptors in the skin, which is part of the somatosensory system. The skin consists of different layers (Figure 2.1) which are embedded with these sensory receptors, activated by different stimuli (30, 10, 92). The main receptors are:

- mechanoreceptors: Meissner corpuscles, Merkel's disks, Pacinian corpuscles and Ruffini endings. They respond to mechanical stress on the skin;
- thermoreceptors: free nerve endings that respond to temperature;
- nociceptors: nerve endings that respond to damage leading to pain perception;
- proprioceptors: provide the sense of position.

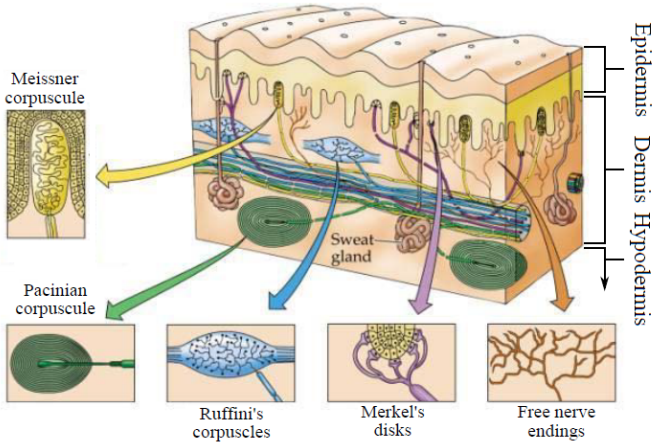

Figure 2.1: Touch receptors in human skin. Adapted from (94)

Therefore, when interacting and exploring the world, tactile sensing plays a fundamental role by providing information such as: contact parameters related to the task performed, such as an object's texture, shape, and temperature, hardness, pain (85, 62); control parameters for manipulation, grasping ans slip prevention (84, 113).

Such functionalities are behind the reason why the sense of touch is of extreme importance in our daily lives. Consequently, research on artificial tactile sensing has seen a growing interest in academic and industrial environments. This has resulted in a substantial body of literature, for example in (51, 68, 191, 48, 67). Figure 2.2 shows that the number of studies on tactile sensing has recently witnessed an explosion of interest by the research community.

This growing interest is motivated by many factors, in particular the need to introduce sensing technologies into several contexts, such as: safe human-robot interaction; medical applications; the service and manufacturing industries; augmented reality; and the internet of things. See Gallace et al. (67) and Lee (109) for a review on tactile sensing technology developments and their application areas.

However, despite the amount of research and financial investments in this area, the effective utilisation of these technologies in real applications is still an issue. This is mainly due to the difficulties faced when integrating these sensing technologies into real world scenarios (177). In fact some research is dedicated for approaches that allow to effectively utilise these sensors. In (81), the authors propose to use concentrated and multi-disciplinary efforts, from the material proper-

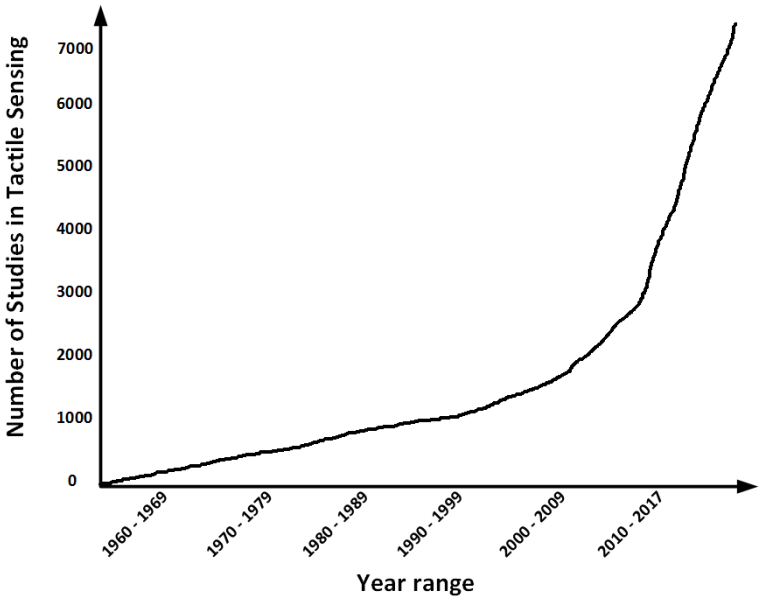

Figure 2.2: Number of studies on tactile sensing. Search performed in February 2018 on Google Scholar based on the words "touch sensor" and "tactile sensor".

ties point of view to the electronics and data communication systems. In (48, 177), the authors suggest to work on facilitating the integration of tactile sensors by improving their flexibility, modularity, costs and easiness of repair. Also, they note that construction of the sensor should be relatively fast and simple.

From the above reasons, it is clear that rigid sensing devices cannot be easily utilised for this purpose. They are not easy to integrate within their host system; they are not compatible with the surface where they are placed on; and they tend to impede the dexterity of the object itself when placed over machines with moving parts. Also, their rigidity makes them vulnerable and the effort of making them small and more compliant results in a complex and costly systems.
Flexible sensing devices on the other hand, present a new paradigm in sensing. They can potentially be easily integrated into different surfaces, and can take the shape of the host system without interfering with its mechanics. They can also be low-cost and easy to replace. Therefore, these advantages can potentially impact the integration of tactile and contact sensors into applications where this is still not feasible today (67). We can sum up the main factors that are responsible for the effective utilisation of tactile and contact sensing devices in real-life scenarios:

- Performance: transduction principle, sensitivity range, spatial and temporal resolution, and ability to measure different types of stimuli.

- Mechanical and physical aspects: weight, resistance to external factors, placement, conformability of the sensor, wiring.
- Electrical aspects: power consumption, data acquisition and communication.
- Algorithms for tactile data utilisation: data processing, feature extraction.
- Engineering aspects: maintenance, reliability, and manufacturing costs.

Other characteristics of the tactile sensor may include self-diagnosis and reliability, where "self-sensing" detection of failure can improve the effective utilisation of the sensor. In the next sections we survey some of the main factors that were discussed above.

2.2.1 Transduction Principle

The transduction method greatly affects the final response and performance of the tactile sensor. Various transduction approaches exist:

1. Resistive/piezoresistive tactile sensors: these sensors experience a change in resistance in the materials they are made of due to an external stimulus which can be for example force/pressure. These sensors have usually a medium-high bandwidth around tens of Hz (48), so they are useful when a high temporal resolution is needed (for example in tactile feedback loops or touch position detection).
2. Tunnel effect: Quantum Tunnel Composites (QTC) tactile sensors based on this type of transduction have the capability of transforming themselves from almost perfect insulators to conductors (25). This is done when they are compressed, twitched or stretched.
3. Capacitive sensors: they are based on changes in the capacitance of the sensing element (165). The capacitance is: $C = \epsilon_0 \epsilon_R A/d$, where ϵ_0 is the free space permittivity, ϵ_r is the relative permittivity, A is the area and d the distance between the plates of the capacitor. Changes in the variables present in the formula of C are used to measure strain, normal or shear forces. Capacitive sensors are easy to use, however, they are difficult to miniaturise since C depends on A linearly, so reducing the size of A would reduce the capacitance and the Signal to Noise Ratio (SNR).

4. Optical sensors: these sensors consist of a light source transmitter and detector. They transduce the change in the detected light intensity to measure the external stimuli (124). These sensors present very good advantages such as low wiring complexity, linearity, negligible drift. However they are usually fragile and not easily conformable to different surfaces.

5. Piezoelectric sensors: the sensing principle behind this transduction method if the ability of certain materials to generate a voltage in response to an applied force (89). Some of these materials are suitable for dynamic tactile sensing, due to their high bandwidth (48).

6. Ultrasonic-based sensors: they can be used to develop tactile sensors, for example to detect contact events (9).

7. Magnetism-based sensors: they measure a change in flux density when an external stimulus is applied (151). They present a good sensitivity and linear response, however, these sensors are limited to be used with nonmagnetic mediums.

2.2.2 Mechanical/Physical Aspects

The mechanical and physical characteristics of a tactile flexible sensor are extremely important for its integration. These features mainly include the sensors's mechanical flexibility and conformability; stretchability; spatial distribution; and optimal placement of sensors.

Flexibility In this thesis we consider flexible sensors, therefore a detailed explanation of flexibility is presented here.
For a tactile sensor to be defined flexible, it must be mechanically flexible, i.e. bendable or/and stretchable, and able to conform to arbitrarily curved surfaces such as the ones of a robot's body, medical instruments such as smart catheters, or, the human body.
Most available flexible sensors use miniaturised rigid sensing materials that are enclosed in soft substrates (209, 204, 42). Despite being flexible, they are still prone to failure when mounted over curved surfaces due to the presence of different internal structures which create fragility. Other solutions use standard off-the-shelf components placed on flexible Printed Circuit Boards (PCB) (47).

The sensor bendability depends on the thickness and the elastic modulus of both the substrate and sensing layer. Given a sensor bent to a cylinder of radius R, where the sensing layer and the substrate have thicknesses d_{sens} and d_{subs} and Young's moduli Y_{sens} and Y_{subs}, the strain on the top surface ϵ_{top} can be calculated as (194):

$$\epsilon_{top} = \frac{d_{sens} + d_{subs}}{2R} \frac{(1 + 2\eta + \chi\eta^2)}{(1 + \eta)(1 + \chi\eta)} \tag{2.1}$$

where $\eta = d_{sens}/d_{subs}$ and $\chi = Y_{sens}/Y_{subs}$.
The strain on the surface top of the sensor depends on the size of the discrete sensing and electronic components. This strain can increase (thus reducing bendability) when choosing materials that are too different between each other or too thick.
Therefore, as a general rule, when electronic components are embedded within the sensing area of a sensor, they increase its stiffness and therefore restrict the overall bendability. As a consequence, flexible PCB–based solutions are suitable only for covering body parts with large curvature but not for parts such as fingertips of a humanoid or a surgical instrument like smart catheter.
Other approaches consist of developing flexible electronics by using thin plastic substrates (180), however this still causes high costs, and expensive materials or fabrication processes are required.

Tactile/contact sensors made of conductive woven–like fabrics are also another type of approach. In fact, these solutions are low-cost, extremely flexible, bendable and conformable to different surfaces. Also, they tend to have a more "pleasant feeling" when used for human interactions. This topic will be further discussed in Section 2.3 and will be at the basis of this thesis.

The ability to stretch is another factor to take into consideration when dealing with flexible tactile sensors. This property can be achieved by either working on the geometrical arrangement of small sensor patches, or by using intrinsically stretchable materials as transducers. For example, in (169) and (40), microchannels filled with conductive liquid are embedded into a silicone substrate as an interesting alternative to rigid wires and sensing components. However, it is worth noticing that the presence of different structures inside the transducer can still cause fragility, or a reduction in flexibility.

Number, Shape and Placement of Sensors If working with many sensor modules, their number and the way they are placed over the object's surface greatly influence the measurement precision and the final performance of the system. Choosing the correct number of sensors and their position need to be strategically done depending on the functional needs, and the type of input stimuli that need to be detected. This idea have been already exploited more than two decades ago, where in (33), a statistical decision theory Bayesian approach is used to determine the optimal number of sensing elements to be used for recognition and localisation operations. Recently, other works have been also presented in this context. For example, in (142) a method for optimally placing tactile sensing modules for grasping applications is presented.
In general, a higher number of sensors generally means higher precision in the tactile information. However, increasing the number of sensing modules can increase noise, wiring and costs (31). For example, in (149) a tactile sensor composed of multiple scalable modules with a bus-based communication network is presented, along with its placement on curved surfaces. A serial bus communication is used to avoid excessive number of wires, but still this solution is not completely conformable to the object's surface.
In case of contact sensing solutions that come as patches made of several modules, the shape of each module contributes greatly to the final system performance. Also, the arrangement of these modules determines the way they conform to the host's surface and possibly, the way they follow its movements. Examples of hexagonal or triangular shapes can be found in (137, 141) and are shown to influence the degree of bendability that wants to be achieved.

Wiring As already mentioned, wiring is one of the main challenges that need to be addressed when developing flexible tactile sensors. In fact, excessive wiring for power supply, data acquisition and transmission can be of impediment for sensor integration in real world applications.
Intelligent routing and addressing schemes can help reduce the total number of wires. For example, in (147), a tactile sensor design that allows data acquisition from a patch of sensor modules using a single wire is presented. The wiring reduction is achieved by designing the sensor array as an analog filter and the tactile data from each module is addressed sequentially. As a consequence, the temporal resolution of the sensor is decreased.
The effect of wiring can also be of obstacle when using inherently flexible materials

as the in the case of piezoresistive fabrics. In (195), a flexible tactile sensor based on piezoresistive fabrics is presented. Resistance measurement of small sensors taxels is achieved by wovening stainless steel threads in the sensing element in a matrix structure. However, while the sensing material is inherently flexible and the wiring threads are compliant, this design still presents drawbacks when scaling the sensor to bigger sizes (the number of woven stainless steel threads has to increase in order to keep the same spatial resolution).

2.2.3 Electrical Aspects

Power consumption One important aspect to take into account is the power consumed by the sensor unit. If the sensor is made by multiple modules, each one would require power to operate, therefore if the number of modules increases then the power consumption of the system as a whole increases as well. For example, in (138) and (137) a current drawn of about 130 mA is reported per each sensing module powered at 3.3 V. This increases greatly the power consumption when adding several modules. Power consumption becomes an important factor especially when dealing with battery-powered systems. Recent studies are also focusing on promising technologies for self-power generation in tactile sensors. These include flexible solar cells (119) and stretchable mechanical energy harvesters (156). Nevertheless, these technologies can be still considered at their infancy.

Communication systems Communication systems are an essential part of a tactile sensor. In fact, the raw sensed data need to be forward to higher levels where they can be processed and decisions can then be taken. In this context, a strategic communication framework and hierarchical architecture are needed to have effective implementation of the contact sensors. For example, in (155), a computational framework is achieved with an Artificial Intelligence (AI) approach to manage the communication and electronic in the case of several sensor modules.

Data acquisition The main function of a Data Acquisition (DAQ) system is the measurement or generation of real-world physical signals. Common commercially available DAQ boards are multi-functional and they provide analog, digital, and timing Inputs and Outputs (I/O). They also present Analog-to-Digital (ADC) and Digital-to-Analog Converters (DAC). As the name suggests, ADCs

are used to translate analog electrical signals into their digital counterparts to be interpreted by the computer. After the transducer transforms the physical signal into a measurable electrical signal (such as voltage or current), the ADC samples this analog signal at a specific rate and transforms it into a digital one. Vice versa, DACs convert a digital code to an analog signal.
Usually, DAQ boards present one ADC only. When reading analog signals between multiple channels, internal multiplexers are used to switch between them to sequentially connect each one to the single ADC. As one can imagine, fast multiplexing systems generally result in measurements of multiple analog signals that are more accurate.

The Number of Bits (NoB) is a fundamental parameter that measures the dynamic range of an ADC. The NoB determines in how many levels the analog values can be represented, so it determines the resolution of an ADC. This makes 2^{NoB} different values for the conversion, therefore the more NoBs, the higher the resolution of the measurement and so the smallest amount of change that can be detected by the ADC.
The resolution of the conversion is also determined by the input range of the ADC and the gain of the amplifier that precedes the conversion step. In fact, an instrumentation amplifier (PGIA) is used to amplify the signal before the conversion so that it could use the full resolution of the ADC. This amplification depends on the input range of the analog input channel. This can be usually programmed by the user.
For example, an ADC with 16 NoBs can convert analog inputs into 2^{16} possible digital values, which are fairly spread across the predefined input range. Therefore, for an input range of -5 V to 5 V, the resulting resolution of measurement will be:

$$\frac{5\,V - (-5\,V)}{2^{16}} = 160\mu\,V \tag{2.2}$$

The rate at which the above processes are performed determines the sampling rate of a DAQ system. This is a very important parameter to take into consideration when dealing with time-varying signals, as the DAQ must be fast enough to capture and convert small changes in the signal.

If dealing with multiple sensing modules, data acquisition can be an issue. In fact, it is possible to either address each module serially to decrease complexity (but increasing time), or in parallel (but decreasing the sensing rate (149)).

Some in depth reviews of data acquisition techniques for general application include the following sources (14, 102, 212) and (153) a review is presented in the context of tactile sensors.

2.2.4 Data Management Aspects

In this section we report the various techniques used to pre-process raw signals and extract useful information from tactile data. In the context of robotics, these information are used to perform complex tasks like grasping (98); or for understanding the modality of touch and recognising emotions in social human-robot interactions (44); one example in medical applications is to provide haptic information during minimally invasive surgery robotic palpation (145).

Signal pre-processing Before processing the data and extracting important indicators, pre-processing signals is a crucial step that aims at reducing background noise, filtering out the errors of measurement systems, and improve the SNR. Common techniques for data pre-processing include mean-centring, unit variance scaling and signal filtering.
It is worth noticing that, when acquiring time-series data, or data that are changing in time, it is generally not interesting to look at the systematic shift in the data, which can in fact result from sensor drift. Hence, the trend of a signal should be discarded before signal processing. This step allows to focus only on analysing the fluctuations in the data. Furthermore, if data is collected from different sensors, each segment of data could show different numerical ranges. Therefore, it becomes necessary to standardise raw data. These steps can be achieved by employing unit variance scaling and mean centring (205).

Filtering the signal (53) can also enhance the signal quality. This is performed by removing undesirable frequencies from the signal, which reduces the interference of noise. Band-pass, band-stop, low-pass and high-pass filters can be used for signal filtering. Each of these filters works based on specific cutoff frequencies. Another classification of filters is based considering the properties of the signal that is being filtered. As the name suggests, analogue filters work on analogue signals, while and digital filters are applied on digital ones. Digital filter can also be subdivided into Finite Impulse Response (FIR) filters, and into Infinite Impulse Response (IIR) filters. For a more thorough review of signal filtering, we refer to (53, 212).

Signal processing Signal processing is a step that is used in order to extract meaningful information from the acquired data. This is usually performed so that meaningful information about the real world physics are obtained. During signal processing, important features or indicators can be extracted, constructed or selected from the signal (121, 79).
Signals are processed in one of the three different domains: the time domain, frequency domain, and time frequency domain. These approaches are application specific and dependent on the available measurements and the nature of the signal.

- Time-domain analysis is applied directly on the signal time. Features are computed from the time waveform, and they are usually statistics such as the peak to peak interval, the mean, standard deviation, crest factor, root mean square, skewness, kurtosis etc.

- Frequency-domain analysis is performed in the frequency domain of the signal. Spectrum analysis using the Fourier Transform (FT) and the Fast Fourier Transform (FFT) and commonly used. This analysis is advantageous when compared to the time domain analysis because certain frequency components of interest could be isolated, which can lead to more robust and targeted features.

- Time-Frequency domain analysis, where the analysis is performed on both time and frequency domains. In order to conduct this analysis, techniques such as the short time Fourier transform (STFT) can be applied. The advantage over the frequency domain analysis is the ability to handle non-stationary signals.

In (74), the authors present their hardware, signal processing and classification techniques in the context of tactile sensing systems for anthropomorphic robot hands. A Polyvinylidene Fluoride (PVDF) piezoelectric tactile slip sensor is used to collect data and recover an image of the applied pressure profile. STFT is used to transform data from time domain into frequency domain. Then, principal component analysis (PCA) generates input features for classification of slip modalities (slip, no-slip, noise). The slipping is detected by the change of the position of the signal over time. In this same work, contact detection and pattern classification are performed by finding the local maximum of the reconstructed image. This is done using a 3-by-3 mask on the image pixels, eliminating pixels plateaus, applying normalisation of the image's pixels with respect to the applied

pressure, dimensionality reduction with PCA, and finally classification. This is shown in Figure 2.3 These signal processing techniques were specifically applied for grasping and manipulation of objects.
In (44), the authors use signals from touch sensor and vision sensors for identifying how people show affection through touching a humanoid robot. Eight touch sensors were placed on five areas of the robot: chest, face, back, and both arms. A Microsoft Kinect vision system was used to obtain postural information from the participants. Raw data from the sensors was processed to obtain features as a combination between the tactile sensors readings and the kinect's vision systems. These features were further processed to obtain statistical indicators and classification was performed using ML techniques.
In the context of medical application, a tactile sensor for monitoring the human skin conditions has been presented in (197). Here, the features for detecting different textures are extracted by calculating the temporal average of the absolute output signal and, in the frequency domain, power spectrum density is performed to capture vibration signals.

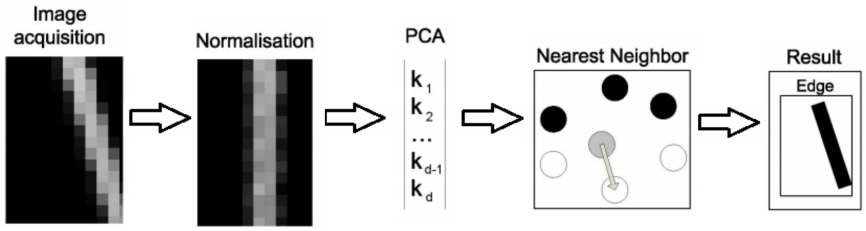

Figure 2.3: Classification system for contact patterns. Adapted from (74)

Most of the times, considering engineered features rather than the raw signals themselves can greatly improve the data interpretation and classification. This also helps reducing the amount of transmitted data and computational costs. However, special care must be taken since features extracted with data processing techniques can bring a loss of information regarding the input, therefore case specific knowledge is required when performing these techniques.

After signal processing is performed, different algorithms are then used to interpret the data, this is shown in the next paragraph. AI techniques are also commonly used (see Section 2.5 for more details).

Algorithms for Data Representation Once tactile data are collected and features are extracted, these need to be interpreted by the higher levels of a

sensing system. This topic is still an open challenge in tactile sensing contexts and several approaches are found in the literature for effective utilisation of tactile data (182, 48).

Common ways of handling these features are inspired by computational techniques developed in the area of computer vision. Here, after images are reconstructed from tactile inputs over sensing elements, contact information are extracted from the images. In (120) for example, different shapes of contact objects are distinguished based on pressure maps. A similar approach is shown in (128), where a Scale-Invariant Feature Transform (SIFT) is used to detect and describe local features in images from tactile data, and applied for object recognition. SIFT applied on an image will return keypoints, where each keypoint has an associated vector that describes the region around that point. This is shown in Figure 2.4

When dealing with whole body sensors or multiple tactile sensing cells, representing contact data for the different areas provided with these tactile sensors is still a research challenge. Humans in fact present what are called somatotopic internal maps. These are our way to create a correspondence between an area of the body where a specific sensory information is detected, and a point on the central nervous system. Similarly, research effort have been directed towards developing frameworks that map the tactile sensory data into artificial somatosensory maps (55). For example in (34), the authors propose a framework used to map sensing elements placed over a robots into a 2D somatosensory map. A similar approach is extended in (139). Here, the sensory modules present embedded light emitting diodes which are translated as visual markers into a homogeneous 3D body representation.

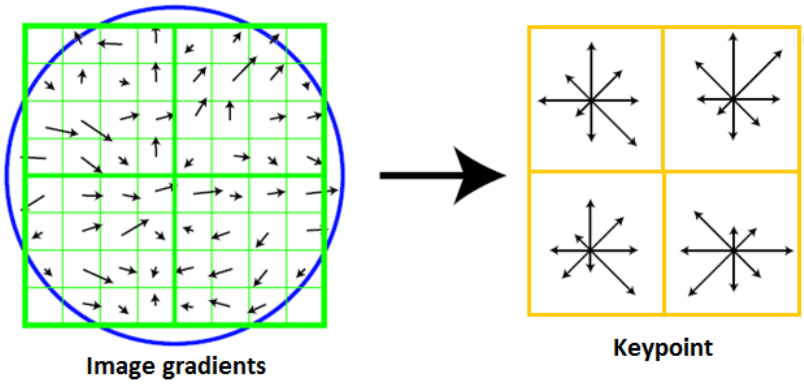

Figure 2.4: SIFT and creation of keypoint descriptors. Adapted from (125)

Sensor Fusion In the same way humans combine sensory data from different sources (61), the use of different complementary or even overlapping sensing modalities (e.g. tactile, vision, kinesthetic) can improve the "intelligent" behaviour or response of a system (127). A flowchart of a sensor fusion system can be seen in Figure 2.5. Also, the information redundancy from multiple sensors can reduce error and noise and increase robustness (115).
For example in (122) a fusion framework is developed for object recognition tasks based on visual and contact sensor data. Multivariate time-series models are used to represent the sequence of tactile data while covariance descriptors characterise the image. A similar work is also presented in (193), where the authors additionally propose a grasp planning method based on the classified objects from visual-tactile sensor fusion.

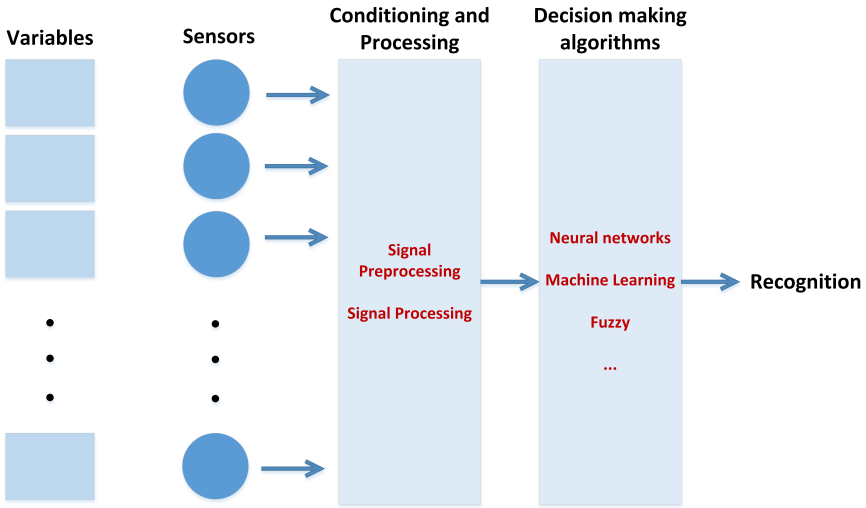

Figure 2.5: Flowchart of a sensor fusion system

2.3 Fabric Sensors

This section aims at giving particular focus on flexible contact sensors made of conductive fabrics, which represent the approach at the basis of this thesis. This particular type of sensors has got the attention of the community in tactile and contact sensors and a lot of research is been conducted on the topic (52, 192, 35). For example Google has recently shown interest in developing interactive textiles. Jacquard (162), is a technology in which novel textile materials are woven into clothes to create interactive textiles that can be used for manufacturing soft toys,

furniture and clothes that are responsive to touch and other inputs from humans. This is possible through the use of conductive threads and embedded electronics. The conductive metals are very thin and can be combined with different types of fibres. Because of this, they can be woven using traditional techniques and equipment, and wash them just like any type of other clothes.
Also Nasa (1) has shown interest in electrically conductive fibres and worked with Syscom Technology, Inc., a high-tech textile company, on the development of an electrically conductive, low-weight, strong and flexible yarn under the name of AmberStrand (Figure 2.6).
In fact, while present day flexible sensor designs still present challenges which brings them far from real applications, fabric based solutions are low-cost, easily customisable, flexible, bendable and conformable to different surfaces and they can have a more "real skin feeling" when used for human interactions.

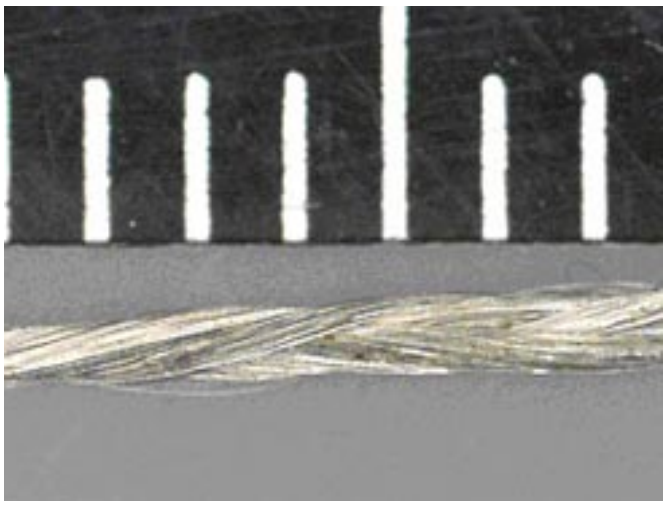

Figure 2.6: AmberStrand conductive yearn under a millimetre scale

In this work we will use the terminology fabric to define a flexible material which consists of a network of natural or artificial fibres (yarn or threads). Yarn is a processed fibre produced by spinning wool, silk, cotton, hemp, or other materials to produce long fibres. Fabrics are formed by weaving, knitting, crocheting, knotting, or felting (123). In the literature, related words as textile or cloth are often interchangeable with fabric.
The term electronic textiles (e-textiles) is often found in the literature to indicate those fabrics which feature off-the-shelf electrical components woven into them. This transforms the fabric material into a kind of flexible breadboard. A review paper on recent advances in the field of e-textiles can be found in (192). The

terms smart fabric sensors or smart fabrics are also used in general to address fabrics that present sensing properties (35).
The advancements in material processing and designing processes (164) are enabling the emergence of smart textiles to be used as multifunctional wearables, allowing them for a seamless integration into their host systems. For example, by using polymeric materials, it is in fact possible to realise sensors, actuators and power sources and develop smart fabrics that provide good wearability, low power consumption, low-cost, and eventually autonomy. A review of polymers adopted for sensing and actuation applications is found in (52).

Piezoresistive fabric materials are often employed for realising flexible contact sensors. Piezoresistive fabrics can be produced by coating individual fibres or the entire fabric with electrically conductive polymers. These coated fabrics also have other applications in the areas of electromagnetic interference shielding (101) or chemical sensing (43). Another way to develop electrically conductive fabrics is to replace some of the yarns in the fabric with integrated conductive fibres, for example through a weaving process. However, compared to the integration of conductive yarns by weaving, the advantage of coating is that it uniformly covers the individuals fibres of the fabric producing good homogeneous conductivity. This process still leaves almost unchanged the feel of the fabric itself and the substrate properties such as density and flexibility. However, the coating material and the substrate need to be specifically chosen to avoid incorrect adhesion between the coating and the fibres.
A very common way of coating fabrics with electrically conductive polymers uses Polypyrrole (Ppy, an organic conducting polymer) (77). This method is based on the polymerisation of the pyrrole monomer and aniline directly on the substrate (116).
Regarding the materials used as substrate, polyester is between the ones mostly used (80, 116). Other approaches include nylon, cotton, wool (206, 99, 150). Fabrics made of nylon-cotton with Lycra are used to produce very stretchable piezoresistive materials. Methods for applying Ppy on these fabrics are reported in (50) and are also patented by Milliken (107) and Eeonyx Corp. (15). In Figure 2.7, a scanning electron microscope (SEM) image of the polypyrrole coated textile is shown.

The piezoresistive characterisation of a PPy-coated Lycra fabric is reported in (50, 52). The tests are performed reporting the quasi-static resistance changes vs. tensile strain and vs. compressive stress. Tests for temperature sensitivity are

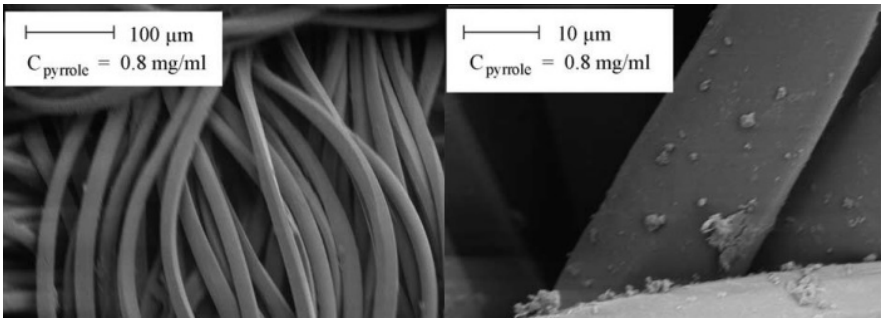

Figure 2.7: SEM image of the polypyrrole coated textile (with pyrrole concentration of 0.8 mg/mL). On the left, 100 μm scale and on the right 10 μm scale. From (116)

also reported showing that the Ppy-coated Lycra fabric sensitivity to temperature is high. Experiments with conductive and non conductive weights were also reported in (166) for a Velostat film, which is a carbon-impregnated polyolefin. In both studies, the results showed that the resistivity of the sample materials decreases when pressure is applied.
It is very important to note that in the case of flat textile materials, the resistivity is not an intrinsic physical property, independent of the particular size or shape of the raw material, but depends on the arrangement of fibres and yarns (203, 13, 12). Also, the manner in which the electrodes are arranged on the surface of a flat textile product is of great significance for sample resistance measurement results. In fact, the measuring electrodes can influence the effectively measured resistance and therefore falsify the results. (203). Therefore the textile material structure and its properties can be generalised but until a certain degree.

In the contact sensing literature, fabric sensors have been used in many applications. In (136) it is presented a textile, pressure sensor for integration into clothing to measure pressure on human body. The sensor is made of a three-layer structure forming a capacitance with a pressure sensing non-conducting dielectric (Figure 2.8). The final spatial resolution is determined by an array of up to 32 assembled sensing modules individually connected by embroidered silver coated yarn electrodes.

In (185) an in-shoe plantar pressure measurement system is developed which uses an array of fabric pressure sensors. Fabric pressure sensors are developed by embedding a knitted strain sensing fabric coated with carbon-black-filled silicon into a top-and-bottom conversion layer. Then, the sensor is enclosed by silicon rubber. The sensors are then connected with a line structure electrodes to con-

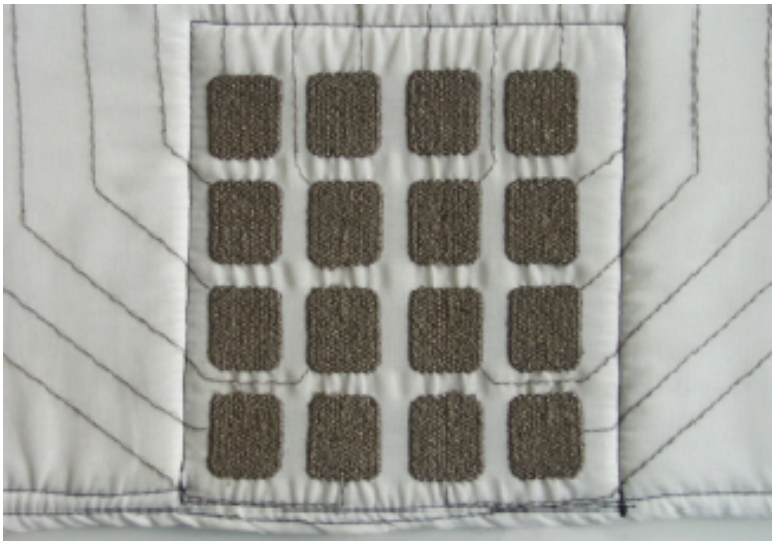

Figure 2.8: Textile pressure sensor with 16 sensing elements embroidered with conductive yarn. From (136), Copyright © 2006, IEEE.

struct a sensor array. A data acquisition system transmits wirelessly the data for processing and parameters for gait analysis and calculated.

In (32), 54 fabric contact cells are embedded in a single sensor glove patch. The contact cells are made of a piezoresistive Eeonyx fabric (15) and connection wires are linked to each patch terminating in a DAQ unit. The drawback of the resulting contact dataglove is that it not easy to customise. Also, each of the 54 taxels requires an individual input channel of the ADC (together with a fixed pull-up resistor for measuring the voltage change), which greatly complicates the hardware design and costs.

In (195), a similar approach is presented, where a contact fabric based sensor is made of a piezoresistive material. In this work, the resolution can be adjusted by changing the number of micro-mechanical taxels created by internally stitched connecting wires.

The drawback of the above approaches is that, even if they use flexible fabric solutions as transduction elements, the way the sensor patches are assembled needs readings based on row–column wires. This makes the hardware complex, possibly suffering of fragility and also creates designs that are customisable only theoretically.

In this thesis we have decided to use a piezoresistive fabric manufactured by Eeonyx, a leading textile company. The material is a LTT-SLPA bidirectionally stretchy knitted fabric (72% nylon, 28% elastane). The individual fibres within

the material are completely and uniformly coated with Ppy. The coating process is patented process from Eeonyx (15), and is tailor-made for a tunable surface resistivity and extremely durable fabric with a tensile strength of $>$ 450N and a tear resistance of 12 N, and approximate thickness of 0.38 mm, as reported by the seller. In order to tackle the drawbacks that are present in literature, we have applied a technique called electrical tomography on the piezoresistive fabric material. This approach allows to develop a flexible contact sensor without any internal wiring. Electrical tomography is presented in next section.

2.4 Tomography Systems

As already discussed in Section 2.2.2, the presence of different materials embedded in a tactile sensor is usually one of the main cause in the reduction of their flexibility and/or stretchability. Also, the number of wires that are necessary to transmit data from multiple tactile modules can be an issue. An approach that has been recently used to compensate for this drawback, which is the main topic of this thesis, is electrical tomography (187). This technique allows to place the electrodes only on the boundary of the active sensing area of a tactile sensor. As a consequence, no wiring is present inside the sensor. Therefore, electrical tomography-based sensors can be placed over different surfaces and robotic joints, allowing them to easily move.

By definition, tomography is an imaging technique used to scan the body under examination by sections, using of any kind of penetrating wave. This method is adopted in many applications with different sensing modalities, the reason being the distinctive capability of each one of them to obtain different parameters. For example, X-ray tomography is commonly used (87) together with positron emission tomography (159) in medical applications.
Electrical Resistance (ERT), Impedance (EIT) and Capacitance (ECT) tomography techniques measure the resistance conductivity or dielectric permittivity distributions within an object from electrical boundary measurements (21). EIT is mainly applied in clinical applications for patient monitoring (189) and pulmonary and cardiac functionality (27). This is because EIT is a non invasive and non-ionizing method which uses a low frequency or DC current to measure conductivity changes, differently from other medical imaging techniques. Other applications of EIT include damage detection (196) and pressure sore prevention (103).

Other sensing modalities include Wire-Mesh Tomography (WMS) used mainly in gas-liquid flow measurements (46); Magnetic Induction Tomography (MIT) (129) that measures electromagnetic properties of an object by using the eddy current effect; Inductive Flow Tomography (IFT) for showing velocity distributions in conducting liquids (111); Microwave Tomography (MWT) measures the dielectric loss distributions from several microwave transmission arrangements (181); and Ultrasound Tomography (UST) utilises ultrasound waves as physical phenomenon for imaging (60).
In this work we are mainly concerned with contact sensing systems that use EIT or ERT techniques. Therefore, from now on we will refer to them as electrical tomographic methods. These are considered ill-posed non linear inverse problems, where the aim is to reconstruct the conductivity distribution of the body under study from measurements taken at electrodes placed the boundary. The reconstructed conductivity is then showed in an image by applying an inverse reconstruction algorithm. The quality of the reconstruction depends on many factors, which are the type of reconstruction method, the hardware system, noise and the properties of the body under examination. Some of these are reviewed in next.

The concept of inverse problem analysis can be illustrated with a simple example, in Figure 2.9: let's assume we want to understand the 3-D shape of on abject by lighting it from one certain direction and studying its 2-dimensional shadows. These will only contain a small portion of information of the object's 3-D shape. However, capturing extra shadows from different directions will increase the total information we have, enabling us to estimate the shape of the object in a more accurate way. In a similar way electrical tomography reconstructs an image of the conductivity distribution of a conductive body by using electric current and measuring voltages on the boundary. Many different reconstruction algorithms exist for the production of these images. A non-exhaustive review of these is presented in the next section. More in depth discussion on the topic can be found in (222, 5, 117).

2.4.1 Reconstruction Methods

Most algorithms for the reconstruction of the internal conductivity in electrical tomography fall into one of two categories: linear approximations and iterative

Figure 2.9: A picture from the book: Gödel, Escher, Bach: An Eternal Golden Braid by Douglas R. Hofstadter.

reconstruction techniques. However, these always provide inexact results due to the ill-posed non-linear nature of electrical tomography. In fact, these reconstruction procedures represent a compromise between accuracy and computation time required for their solution. The same methods can also be divided into static (216) and differential (dynamic) imaging (3). Static reconstruction commonly involve slow iterative solutions. Dynamic methods instead, are fast and non-iterative and only reconstruct dynamic conductivity changes between two time steps.

Linear approximations techniques generally use a priori information of the system and assume that the small variations in the electrical conductivity from the initial estimate can be considered as linear. This produces fast linear reconstruction algorithms. Back-projection (19) is one example of these techniques, which has been initially developed in 1984 (18) and has seen many variants in the last years (17, 174). This method takes inspiration from X-ray computed tomographic reconstruction where the equipotential volume between a pair of electrodes is projected on the whole boundary of the body. One-step linear Gauss–Newton (GN) solver has been also widely used in electrical tomography (222). This solver works so that a minimisation technique is applied on the difference between the measured data and predicted data to obtain the approximate solution. The pre-

dicted data is obtained by computing a Finite Element (FE) model of the system. However, as the regularisation smooths the conductivity changes, there is a deterioration in the spatial resolution, affecting the ability to reconstruct sharp changes in the conductivity, so that these approaches present low spatial resolution.

Alternatively, non-linear iterative methods (222) are based on iterative inversions of the forward problem, which maps the voltages on electrodes for a given conductivity distribution based on the system's FE model. For example, Newton-Rapson algorithm (117) is a numerical minimisation method that searches for a conductivity distribution that minimises the difference between the measured boundary potentials and those obtained in the forward model by computing the FE model of the system. However, even if these non-linear iterative methods approaches generally produce less errors in the reconstruction, they present higher computational costs which makes them time-consuming and non suitable for real time tomography systems.

The above reconstruction techniques use only the data at a specific time and do not consider the possibility of a certain dependence between the conductivity changes over time. Instead, if the conductivity does not change too quickly, then it is reasonable to expect that past and future measurement are correlated to the current image and can contribute in adding more information in the reconstruction. By incorporating this knowledge, more accurate solutions can be provided. In electrical tomography, this is performed through Kalman filter algorithms (207). Kalman filter is a method for tracking and estimation (95), that is used in electrical tomography to estimate an image at each instant from current and previous data.
Other methods based on AI techniques have also been proposed and will be reviewed in Section 2.5.2.

2.4.2 Electrical Tomography System Architecture

A typical EIT system consists of one or more current sources, a switching mechanism for generating current injection patterns and a data acquisition unit for potential measurements. A generic tomography system architecture schematic is shown in Figure 2.10.

Current Sources In general tomography applications, low frequency AC signals are commonly used as current source. These signals eliminate long-term

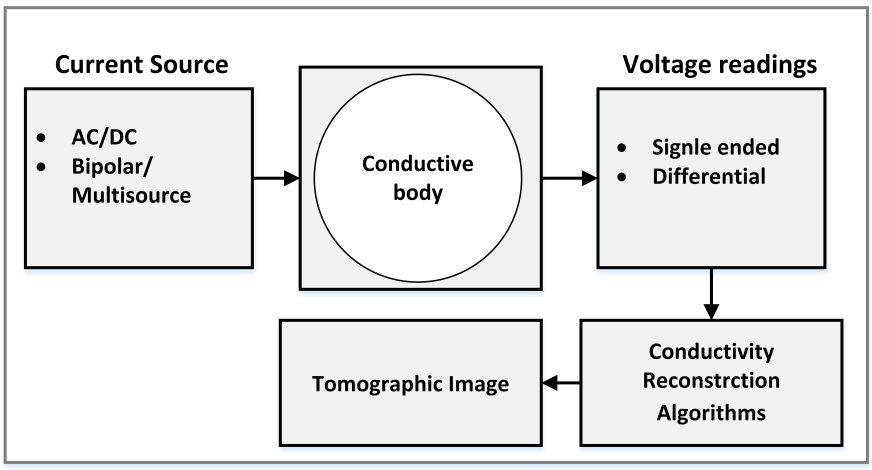

Figure 2.10: Electrical Tomography System Architecture.

polarisation effects in the electrodes and allow to measure the capacitive and resistive components of the conductive body. However, this method also requires synchronous analogue detection circuits and low-pass filters that not only significantly complicates hardware design (and increase costs), but also consumes more power and affect real-time sampling performance, which is disadvantageous for contact real-time applications.

DC currents are commonly used when a simple hardware is desirable and because of their simple implementation in battery-powered mobile hardware. In bidirectional DC currents, the current to the electrode is maintained constant during each half cycle. The current waveform is then a zero-mean square wave, and voltage measurements can be taken during the "flat" parts of the cycle once static electromagnetic conditions have been reached. The hardware is therefore more simple, because that the measurements can be treated as DC signals. In addition, this approach eliminates long-term polarisation effects at the electrodes. Unidirectional DC current excitations have also been used for flexible contact sensors applications (200). This approach requires only a single data measurement at each cycle instead of two required in the bidirectional method, doubling sampling rates.

There are different protocols for performing current injection and potential measurements (29):

- Multi-source protocols require multiple current sources that are simultaneously used for current injection while potential measurements are taken at all boundary electrodes. They have the capability to produce very accurate

image reconstructions, because they can produce high precision signals by avoiding the use of multiplexers. However, they also need as many independent current sources as there are electrodes. This is not practical as such a system is expensive and complex to build.

- Bipolar protocols protocols are those in which a single current source and sink are used to inject current through a single pair of electrodes at a time, while potential measurements are taken at all remaining electrodes pairs.

The bipolar protocol that is most commonly used is termed the adjacent or neighbouring method, shown in Figure 2.11. In this method, current is injected through a pair of adjacent electrodes while the resulting potentials are measured at all other adjacent electrode pairs. This is systematically rotated through all adjacent electrode pairs while potential measurements are taken from all remaining adjacent electrode pairs. Different bipolar protocols have been developed in the electrical tomography literature, they will be discussed in Chapter 4.

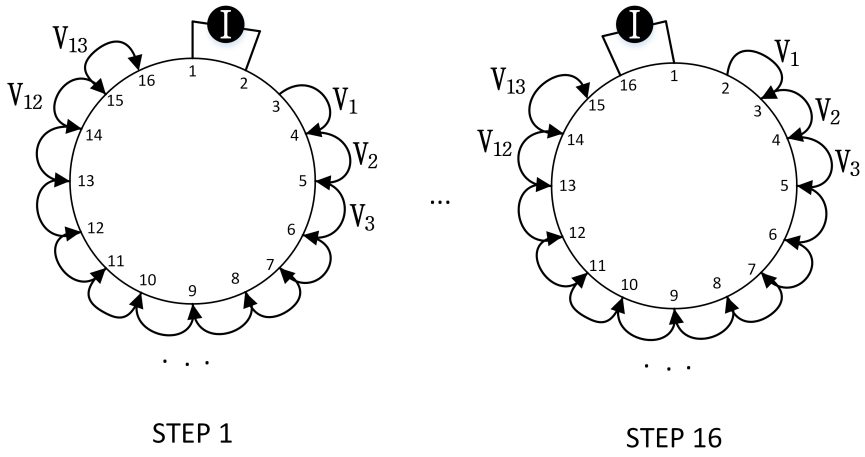

Figure 2.11: Adjacent method: first and last step of the current injection and voltage measurement sequence are shown for a 16 electrodes system.

A way of improving performance in terms of resolution and robustness to noise in the reconstructed image is to add electrodes in different locations within the conducting domain (201). In this scenario, the best improvements can be obtained by adding electrodes in the central area of the sensor, where low current density flow is expected. In (199), the authors present internal electrodes that can be used for both current injection and voltage measurements. However, in the context of flexible contact sensor applications, this approach introduces

connection wires inside the sensor, which is not advantageous.
It should be mentioned that sometimes voltages can be applied as driving signals instead of currents (82, 228). This approach tends to simplify the electronics, however it also creates more sensitivity to electrode misplacement and modelling size errors, as discussed in (88).

Voltage readings Voltage readings can be measured in either single-ended or differential mode. In case of single-ended measurements, the voltages are read with respect to ground potential. When measuring voltage between an electrode pair in differential mode, this is advantageous because it reduces the dynamic range of the sensed signal, which, in turn, reduces the dynamic range requirements for the ADC and therefore increases the resulting resolution. However, this approach also increase the common mode noise (175). This drawback can be contrasted by using instrumentation amplifiers with a high common-mode rejection ratio (CMRR).

In order to avoid incorrect measurements due to electrode impedance mismatch, voltage measurements are usually not collected from electrodes used to inject current. Also, if the current injection and voltage measurements are symmetrical, the reciprocity principle (73) shown in Figure 2.12, implies a decrease in the number of independent measurements. This principle states that the voltage difference V_{CD} on electrode pair (C, D) with electrode pair (A, B) as the ones used for current injection I, will be equal to V_{AB} measured on electrode pair (A, B) with electrode pair (C, B) used for current injection; therefore they can only be regarded as a single independent measurement. Therefore, the mutual impedance Z calculated as V/I will be the same. Because of the above there is a reduction in the total number of information available for the image reconstruction.

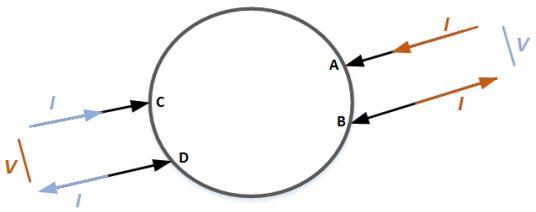

Figure 2.12: Reciprocity principle

To conclude this section, the choice of the correct electrical tomography instrumentation depends on the application. In general however, precise instrumentation plays an important role in the quality of the final result. In fact, the source

of errors in electrical tomography applications depends greatly on the way the hardware is implemented. This will be discussed in further detail in Chapter 3.

2.4.3 Electrical Tomography Sensors

Recent studies (187) have focused on the application of electrical tomography techniques on thin, stretchable and piezoresistive materials in order to create contact sensors. In this way, an image of the touch inputs over the sensor can be reconstructed from the boundary voltages.

Electrical tomography-based sensors are advantageous since they do not have that rigid network within the active sensing area, which makes them inherently stretchable. Therefore, they can be placed over surfaces with different topologies without losing their functionality.

However, electrical tomography-based sensors also present drawbacks, such as: low spatial resolution, which limits their ability to discriminate between close touch inputs (83); and medium temporal resolutions, in the range of 30-45 Hz (187). Such drawbacks will be further addressed in this thesis.

In (196) the researchers used Carbon Nano-Fibre (CNF) plates constructed by embedding CNFs in epoxy, for structural health monitoring. The conductivity of the final material depends on the formation of paths for current circulation within the fibres. By applying electrical tomography, the material was able to detect small damages within itself by identifying conductivity changes, which resulted in self-sensing capabilities. However, the current path flowing through the conductive particles network depended on fibre-to-fibre contact. This can result in a compromised accuracy of the damage location reconstruction.

In (96) the authors developed a flexible rubber mixed with conductive carbon particles. This material however was not very stretchable, presented high hysteresis, and small changes in conductivity due to pressure. Its initial resistivity was low, leading to acceptable reconstructions of the conductivity distribution.

Nagakubo et al. (144) used a pressure sensitive rubber sheet together with a second sheet showing higher resistivity changes due to pressure. The second sheet was placed on conductive rubber. In this way, when pressure was applied, the resulting combination of materials resulted in a amplification of the resistance changes. By applying electrical tomography, a stretch distribution tactile sensor was developed, able to detect inputs such as rubbing and pinching.

Yao et al. (219) used a silver plated nylon elastic fabric, that was able to stretch

in two directions and change its conductivity depending on the applied pressure. The pressure sensor responded to the application of different weights, however results showed that there was not a perfect proportionality between the applied weights and the reconstructed images.

In order to better respond to pressure and decreasing sensitivity to stretching stimuli, Silvera-Tawil et al. (186) applyied electrical tomography on two different fabric materials. One of them, placed at the bottom, was a fabric from Eeonyx presenting electrodes placed at its boundary. The second thin, silver-plated highly conductive and stretchable fabric from Less EMF Inc., was fixed on top of the first material. In this way, the resulting two-layer sensor had reduced resistivity changes due to stretch and still presented resistivity changes when pressure was applied. In order to improve the detection of concurrent pressure points, the second layer was made as a keypad with non-connected fabric squares. Also, another soft fabric was fixed on top to coat the sensor.

Alirezaei et al. (8), realised a pressure-sensitive stretch-insensitive contact sensor using an approach similar to (186) but they used conductive copper sulphide bonded nylon thread as a bottom layer. The structure was placed on top of a non-conductive fabric presenting high stretchability. The use of wavelike yarns eliminated changes in conductivity when the sensor was stretched because the total length of the threads was remaining constant. The main problem was that the conductivity change was non-linear with pressure. The authors tested the approaches on flat and 3-D surfaces.

Chossat et al. (40) developed an electrical tomography-based soft contact sensor by using a soft silicone rubber containing microchannel filled with conductive ionic liquid. The advantage of using a matrix type sensor is that the current flows in a more predictable manner. The ionic liquid used in this case is a Room Temperature Ionic Liquid (RTIL). The problem of using silicone rubber however is that is gas-permeable and can present enclosed bubbles. The experimental results showed that the spatial resolution of this approach depends on the density of the channels in the network and not on the number of electrodes.

A way to deal with problems of carbon filled silicone is found in, (221) where the authors used a carbon-filled liquid silicone rubber that changed its resistance distribution when a mechanical stimulus was applied. A main concern with this material however is its lack of real time properties due to its rebound elasticity after it is deformed, which causes slow recovery of the sensing signals.

2.5 Machine Learning

Machine learning (ML) is a branch of artificial intelligence (AI) that focuses on learning from data. In 2011, a report from the McKinsey Global Institute (133) has foreseen ML techniques as the drivers of the next big wave of innovation. Nowadays, the adoption of ML techniques in the fields of robotics, human-robot interactions (168), and medicine (148) has lead to an increase of breakthrough results in these areas (215).
ML techniques usually require a large amount of data for them to be effective, this used to be an obstacle in the way of their success. Recently however, data has become more abundant, and the computational competencies of our systems are advancing which is resulting in more efficient use of ML approaches in a wide range of applications.

Machine learning can be split into two main types, supervised and unsupervised learning, although other types exist such as semi supervised learning and reinforcement learning. In supervised learning, data (usually multidimensional), is provided along with labels. The task of the ML algorithms becomes to learn how to predict the label outputs from the provided data. Unsupervised learning algorithms instead deal with data that do not have labels. In this case, the algorithm learns to partition the data into different clusters. See (143, 41) for more detail on ML approaches.
Supervised learning is the type of machine learning that is most common and that has been most successfully applied (108). In (58), the author presents key advice on successfully applying ML approaches, specifically supervised learning. The author emphasises the importance of feature selection/engineering on the predictive performance of the algorithms.

Some broad classes of supervised learning algorithms exist. Connectionist methods describe interconnected networks. Here, Artificial Neural Networks (ANN) stand out and are considered as universal function approximators (223). Recently, advancements in ANNs allowed their efficient utility when using multiple hidden layers (108). These networks are known as Deep Neural Networks (DNN). Another class of ML is Bayesian methods. These usually refer to probabilistic graphical methods and are mainly utilised in the presence of uncertainty (105). Approaches that have been used for tactile sensor data are Markov Models as Hidden Markov Models (HMM) (23). Also, in this class stochastic filtering approaches have been used for this kind of data. These methods are Kalman

filters and Particle filters and their respective variants (225). Finally, we point to ensemble methods, bagging and boosting (56) which are a combination of different approaches. An example of such methods are the combination of multiple decision trees, or what is know as random forests. A simplified explanation of this method is that it tries to leverage different decision trees and use the aggregated results for improving prediction accuracy (114).

2.5.1 Machine Learning in Tactile Sensing Applications

ML strategies are used in tactile sensing applications due to their ability of extracting meaningful information when the underlying sensing phenomenon is particularly complex. Challenging assignments in tactile sensing are in fact discrimination of materials, interpretation of touch modalities or reconstructing tactile information when dealing with non-linear or intricate transduction behaviours. ML techniques can deal with these assignments by empirical learning.

For example, in (158) position and orientation of an object is estimated from tactile data using particle filters. In (176), a Support Vector Machine (SVM) regression supervised ML algorithm is used for estimating gesture signal over a fabric-based tactile sensor. Similarly, in (70) a PVDF piezoelectric film is used to build tactile sensor arrays on a rigid PCB substrate. The data output is then organised into a 3D tensorial representation containing space–time tactile information. A pre-processing approach is performed to reduce the dimensionality of the tensors, allowing computational simplification. Then a Regularised Least Square (RLS) and SVM pattern-recognition approaches are applied to treat raw data in tensor form. The data was collected from different touch modalities from 70 participants.

In (178), low resolution images obtained from contact sensors mounted on a robotic finger tip during object manipulations are used to identify objects. Here, k-means algorithm is used on training data as unsupervised clustering method to create a "feature vocabulary", which is then used to train a bag-of-words classifier. This classifier treats image features as if they were words, to learn a codebook histogram. Through this approach, the robot is able to discriminate between a large set of objects.

In (16), material classification is performed using deep learning applied on spatio-temporal signals of a flexible tactile sensor. The authors compare the Convolutional Neural Network (CNN) to SVM classifier, showing improved performance

in the classification when using CNN. However, a limitation of this work is the large dataset required for training the CNN. Material classification is also performed in (90) using bayes trees based on surface texture and in (93) using self-organizing neural networks maps (SOMs) according to shape and size of explored materials using tactile sensors.

It is worth noticing that the accuracy of the results of the ML approaches presented above relies heavily on the type of features used for training the leaning algorithm. These features are mostly chosen by experts in the area, therefore application specific knowledge is always required.

2.5.2 Machine Learning in Tomography Applications

In the case of tomography systems, ML approaches can be generally divided in three main ares: approaches that use ML techniques to solve the tomography reconstruction inverse problem; ML techniques used to classify the reconstructed tomographic images; and ML approaches that use tomography raw data to extract information regarding the input stimuli. This is shown in Figure 2.13.

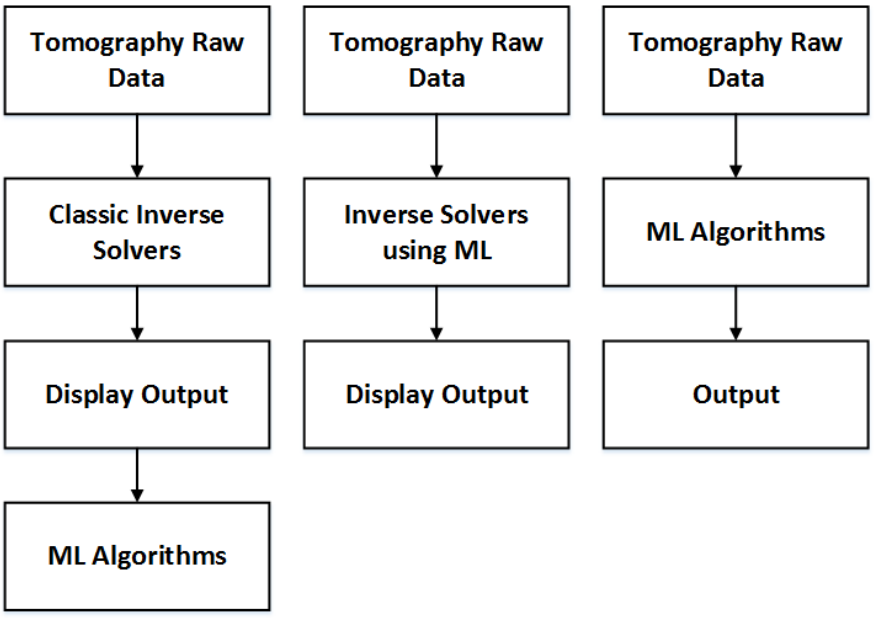

Figure 2.13: Machine learning techniques in tomography systems

ML for solving the tomography reconstruction problem One early work on using ML techniques for solving the tomography reconstruction problem is found in (2). Here, a linear reconstruction algorithm using ANN was directly

applied on tomographic forward problem, without any additional assumption or analysis. However, it was reported that this approach still makes the ANN solver sensitive to boundary mismatch and noise in the measured data.
In (135), the authors propose to first apply a linear tomographic reconstruction algorithm on the voltage data. Then, after the resulting images are reconstructed, they apply ANNs to enhance this solution, reducing the effects of noise and modelling errors. They compare the results with those from a linear solver (one-step GN), a nonlinear iterative method (PDIPM), and a method were ANN are used as a fully replacement for the inverse solver. Results show that the approach of the authors is less sensitive to noise when compared to the other methods.
Another approach using genetic algorithms can be found in (86). In (134), the authors propose to use a Particle Swarm Optimisation (PSO) method to train an ANN to solve the reconstruction problem.
A review paper presenting a more detailed discussion on ML techniques for solving the tomographic inverse problems can be found in (163), with particular applications to brain activity interpretation.

ML for classifying tomographic images In this approach tomographic reconstructed images are used as features during training of the ML algorithms. This is a particular application of the techniques discussed in Section 2.5.1.
In the literature, one example of this approach is shown in (186), where the authors use a ML classification method to distinguish between eight different types of touch applied by humans to a mannequin arm where an electrical tomography-based flexible sensor was placed. Results show that the modality of touch was correctly classified in approximately 71% of the tests. In this work, the set of features used to classify the different touch modalities was a combination between data extracted from the tomography-based sensor, and other data coming from joint sensors placed over the mannequin arm. However, this approach still relies on solving the tomography inverse problem by using the FE physical model of the sensor, keeping the drawbacks of high sensitivity to electrode misplacement and to noise that have been discussed earlier in this thesis. Furthermore, as the model is constructed based on the sensor shape and placement over the mannequin arm, the approach presented in this work would not be feasible in case of movements of the arm. Another similar approach is found in (226). Here, a wearable tomography system for hand gesture analysis is presented. Impedance reconstruction of a user's arm is performed by applying a linear back projection

algorithm on tomographic data. Then, a SVM classification algorithm is used to classify different hand gestures based on the reconstructed impedance.

ML on raw tomographic data In (140), the authors use ANNs for the estimation of key parameters from electrical capacitance tomographic data, in the context of multiphase flow processes. Simulated and real data were used to provide more data variety and generality. The raw data is then pre-processed with Principal Component Analysis (PCA) and used to train multi-layer perceptron networks. The networks were then tested with unlearned data showing how the ANNs are able to determine key flow process parameters, with fast response and good tolerance to instrumentation noise.
A very recent approach applying supervised machine learning techniques in the context of electrical tomography for bladder volume monitoring, has been published in March 20018 (59). In this work, electrical tomographic data sets were obtained from computational models and experiments and fed into SVM and k-NN classifiers, showing a minimum and maximum classification accuracy of 73.16% and 100%, respectively. Then, the SVM classifier was shown to be outperforming the k-NN with 81.66% accuracy on previously unseen simulated data.
In the context of flexible contact sensors based on electrical tomography, one of the first approaches in literature is found in (176). The authors use an SVM regression approach to recognise gesture over a fabric sensor. Five discrete pressure inputs are applied to the fabric material in position intervals at 2.5 cm each and 8 measurement voltages are recorded at each time. One of the problems in this work is that, for the way the sensing materials are arranged, when the applied pressure is very small, the resistance between layers becomes large, so the measurement becomes impossible or very noisy. For solving this problem, the authors use a pressure dependent adaptive noise filter.
In (227), the authors present an approach based on ML and tomographic scanning that can be applied to electrically conductive objects. Here, discrete position classification and continuous tracking of a user's input are performed, with a mean distance error of 9.1 mm. This is tested on several materials but not on piezoresistive fabrics. Also, one important limitation of this approach is that it requires a high number of measurements for the creation of the features, which decreases the system speed.
In (45), the authors use a CNN architecture on tomography raw sensor data to classify different spatio-temporal gaits. Their experimental tomography system

is a floor which contains 116 plastic optical fibres distributed around 3 angles of the floor. When footstep pressure is applied, the intensity of the transmitted light is modulated. The optical fibres angular projections constitute the base of the tomographic approach of the work. A linear SVM classifier is used to discard the unnecessary signals with the lowest classification performance, and then the constructed features are used to train the CNN.
In (166), the authors adopt a neural learning approach that is a Self-Organising Map (SOM) and apply it to recover contact sensory information from a Velostat sensing material. In this case, the authors use the SOM approach to reconstruct the conductivity changes from data acquired from tomographic scanning. They show that this approach is able to reconstruct images of different applied weights, as well as their spatial topography. Also, the approach shows 10 times increased speed when compared to general FE-based reconstructions.

In this work we are mainly interested in this last approach. Here, by applying ML directly on tomographic raw data, there is no need for generating an image that has to be further interpreted by the learning algorithm. Therefore, effective results with minimal computational requirements can be achieved. This is further discussed in Chapter 5.

2.6 Discussion

The aim of this chapter was to provide the relevant background necessary for the work presented in this thesis. We discussed the main requirements and the different approaches used in the field of flexible tactile sensing technologies, with particular focus of piezoresistive fabric sensors for contact sensing. Electrical tomography imaging was described along with its system architecture and implementation for the development of electrical tomography-based contact sensors. Then, machine learning approaches in the field of tactile sensors were reviewed together with their utilisation for tomographic applications.

We therefore conclude this chapter with the following note. For a contact sensor system to be effectively implemented in real world scenarios, many factors should be taken into consideration. The sensor should be simple to conform to the various shapes of the host's surface. Due to the repeated contacts with the environment, the sensor can be damaged, so faulty parts should be easy to repair or replace. Factors like the choice of the transducer, power consumption, and sensor placement are of great importance. Signal processing techniques are generally

used to improve the signal and extract important features. Algorithms for tactile information extraction can also be applied. Still, existing flexible tactile sensor prototypes often present low accuracy and reliability, complicate integration, so that their effective utilisation and implementation largely remains impractical nowadays.

In this thesis we aim at tackling some of the above issues by presenting our approach for the development of a flexible fabric-based practical contact sensor system.

Chapter 3

Electrical Tomography Sensor System

Contents

3.1 Chapter Summary

This chapter demonstrates our development of an electrical tomography sensor system. We start by discussing the drawbacks of using tomography imaging techniques and cover some of the existing tomographic sensor systems.

We then show our methods which include our sensor system along with all its elements: current injection and voltage measurement; data acquisition setup and multiplexing; and the transducer element. Moreover, our image reconstruction and data processing approach, along with a simulation study are presented. Finally, experimental results are provided along with a discussion about the system configuration and performance.

3.2 Introduction

As mentioned in Chapter 2, electrical tomography presents advantages for developing flexible contact sensors. Nonetheless, tomographic imaging presents a major drawback as described by Holder in (83). It is an inverse problem where the aim is to reconstruct the conductivity distribution of the body under study from measurements taken at the boundary. Thus, it is mathematically severely ill-posed, non-linear, and is very sensitive to small changes in potential at the boundary measurements. Therefore, the image reconstruction of the internal conductivity is apt to errors, and so tomography sensor systems suffer from low spatial resolution. However, the spatial resolution can be improved by increasing the number of electrodes (198). This is because more information is made available for solving the inverse problem. Yet this solution affects the time required for performing data collection, and therefore decreases the temporal resolution. Also, improving the image reconstruction by adding more electrodes depends on, and is limited by the precision of the measurement instrument.

The general approach to compensate for such drawbacks is to develop systems that are: precise, whereby they present a good Signal to Noise Ratio (SNR) and exhibit consistent measurements; present a high temporal resolution; and are less sensitive to noise (175). Furthermore, in order to develop practical flexible contact sensors it is also desired to develop low cost uncomplicated systems that require low power consumption. In Section 2.4.2 we give a general introduction on hardware architecture in electrical tomography systems, and discuss some of the challenges and choices that are involved when considering their design

and implementation. Moreover, in the next section we focus on reviewing the existing tomography systems in order to better position our methodology and contribution.

3.2.1 Existing Tomography Systems

Since the appearance of the first electrical tomography systems in the early 1980s (83), the instrumentation used has been constantly evolving thanks to the advances made in analogue and digital electronics. One of the most well known tomography systems was developed in Sheffield back in 1987 (29), and is between the most widely used due to its simplicity and reliability. It presents an architecture using 16 electrodes that are addressed with 4 multiplexers, and operates under a single source, single frequency current of 51 kHz, 5 mA peak-to-peak. The system collects data points for each image to be reconstructed at around 10 Hz. A series of tomography instruments have been produced by the Russian Academy of Sciences (AoS) for breast cancer detection (39, 38). The instruments use a single-source AC current at 50 kHz that is applied over 256 electrodes positioned over the tissue being measured. A 1-to-256 multiplexer is used to inject current on one of these electrodes, while two single remote electrodes are placed at the extremities of the patient to complete the circuit. Here, the increased number of electrodes introduces limitation in the real-time performance of the system, with a full data scan for image reconstruction acquired every 20 seconds. In (76), the authors use a system with 32 electrodes that implements Frequency-Division Multiplexing (FDM). Currents are simultaneously injected at different frequencies, and the resulting voltages are measured in parallel. Then, each voltage is associated to its current frequency by means of a Fourier transform. In (214) a high temporal resolution tomography system for industrial applications is presented. It is used to inject a switched DC current pulse into the electrode pairs, and to measure the voltage waveform with parallel data acquisition taken during the half part of each injection cycle. The problem with such a system is that the switching pulse decreases measurement time, therefore limiting measurement sensitivity. In (200), a DC current is applied to a fabric flexible sensor based on tomographic imaging for human-robot social interactions. A single source DC current is used for simplifying implementation, which has also been used in other works such as (7), and (144). The hardware is supplied with a 12 V power supply, and a single variable DC current source is implemented. The current is multiplexed across 16

Model	Type	N. el.	Specifications
Sheffield System (29)	AC single source	16	4 mux frame rate = 10 Hz
Russian AoS (39, 38)	AC single source	256	1 mux frame rate = 0.05 Hz
EIT FDM (76)	Multifrequency AC	32	Fourier decomposition
ERT system (214)	Switched DC	16	1 ms reconstruction Parallel data acquisition
ERT system (200)	single source DC	16	frame rate = 45 Hz Power loss= 22 mW
EIT system (219)	single source 2 kHz AC	16	Power loss= 175 mW

Table 3.1: Comparison between different existing tomography systems

electrodes, and potential measurements are taken from all channels. A temporal resolution of 45 Hz is reported alongside a power consumption of roughly 22 mW. In (219), a 16 electrode system for tomography contact sensors is developed. A single source current of 10 mA at 2 kHz is multiplexed across the electrodes and injected into a resistive material of 1 Ω/sq. This results in a power loss of about 175 mW.
The above approaches have been summarised in Table 3.1.

Although the approaches present in the above mentioned literature overcome some of the drawbacks of using tomographic systems, none of them address all the requirements mentioned in the previous section, and which are necessary for developing practical flexible contact sensors. In this work, we aim to do that by addressing all these requirements. A detailed discussion of our methodologies and development is presented next.

3.3 Methods

3.3.1 System Design and Development

Our aim is to develop an electrical tomography sensor system that is practical to implement with a simple hardware that reduces costs and power consumption. Also, it is necessary for the system to be able to provide a data frame rate in the range of 30-50 Hz, adequate for many dynamic scenarios found in tactile applica-

tions that require real-time sensing (as real-time distributed pressure monitoring applications, including gait detection). Therefore, we develop our system while considering the following aspects:

1. Single source DC currents, whereby the current is multiplexed across the electrodes are preferred over multiple source currents. This simplifies hardware, reduces costs and power consumption (104).

2. Voltage measurements are to be taken on all electrodes, discarding the ones from current carrying electrodes to reduce the effect of contact impedance mismatch. Voltages acquired in differential mode are preferred as this increases the dynamic range of the ADC and the measurement resolution.

3. An adjustable switching system between different current injection and voltage reading protocols is advantageous. This is further discussed in Chapter 4.

4. The system's Signal to Noise Ratio (SNR) is considered adequate if in the range of 45-60 dB. In electrical tomography systems, SNR is used to judge the system performance in terms of quality of the signal and consistency of measurements (65, 22). It is a ratio between the desired signal and the level of the unwanted background noise:

$$SNR = -20 \log_{10} \frac{|E[V_i]|}{\sqrt{Var(V_i)}} \tag{3.1}$$

   Where $E[V_i]$ is the mean of multiple measurements on each channel and $Var(V_i)$ is the variance of these measurements.

The hardware system for electrical tomography sensor applications presented in this work has been designed and developed between the Centre for Robotics and Autonomous Systems at the University of Salford, and the Research Centre "E. Piaggio", University of Pisa.

This sensor system can be divided into 3 main elements as shown in Figure 3.1 and which are: current injection and voltage measurement; data acquisition setup and multiplexing; and the transducer element. These elements are detailed in the next subsections.

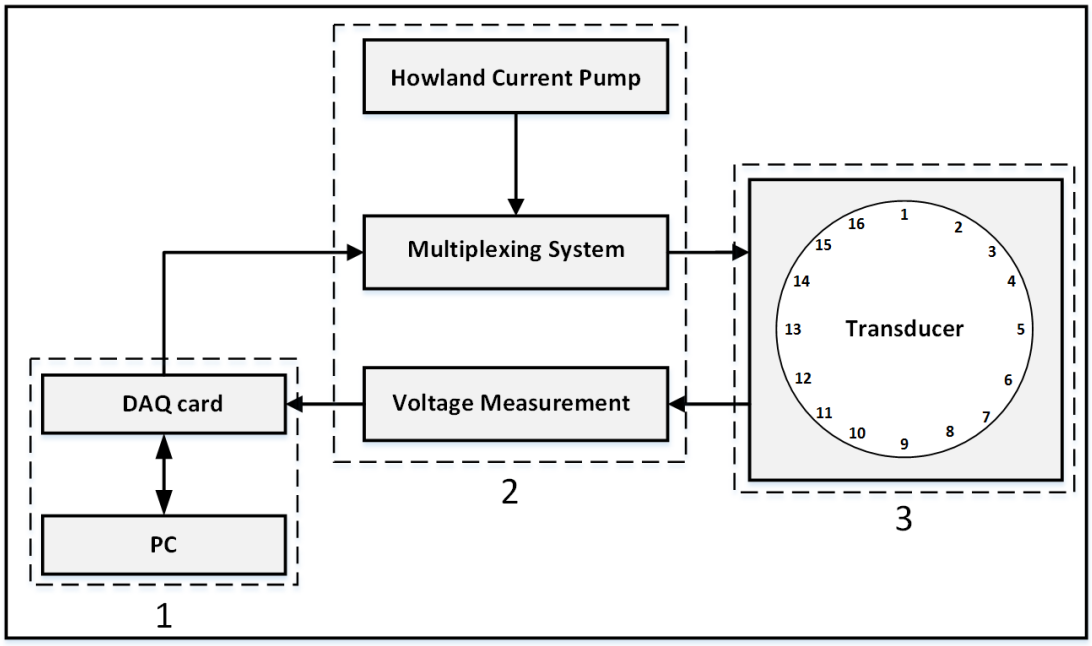

Figure 3.1: Block diagram of our electrical tomography experimental platform for current injection and voltage measurement.

3.3.1.1 Current Injection and Voltage Measurement

We have designed and developed a custom Printed Circuit Board (PCB) for performing current injection and voltages measurements. This is illustrated by block 2 in Figure 3.1, and can be seen in Figure 3.2 along with its schematic.

It presents a power supply connector; a 2-multiplexers mechanism connected to a Howland current pump that serves as a constant current generator; a sensor block for connecting with the sensor electrodes; and a connection for interfacing with a Data Acquisition card (DAQ). The PCB works by allowing for a sequential injection of a constant unidirectional DC current between electrode pairs, using a time-division multiplexing procedure. The connector to the DAQ card serves for both multiplexer control, and the collection of the voltage data. Differential voltages are read from all the electrodes at each current injection cycle. The PCB can be powered using both a USB or a wall block power supply. The design consents for a maximum of 16 electrodes, which we find adequate for the goals of our study. It also provides adjustable switching between different types of current injection and voltage reading protocols. This can be done logically by adjusting the multiplexing control, or physically by adjusting the wire connections on the voltage reading block.

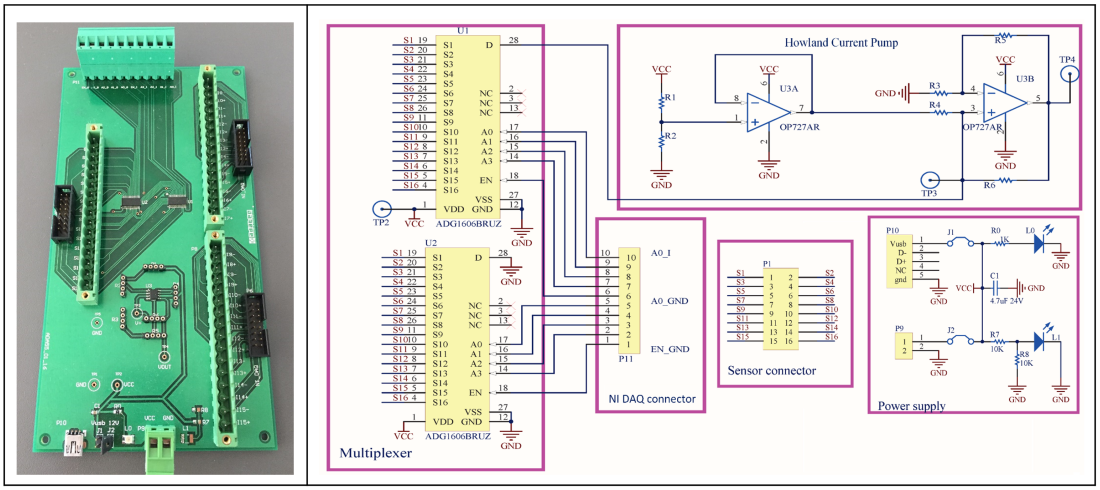

Figure 3.2: On the left, our customised Printed Circuit Board (PCB). On the right, schematics of the PCB in our proposed tomography system, with the sensor connection block, 2 multiplexers, and a Howland current pump.

The current source in a tomography system must supply current with a desired precision over a specific range of load impedance. Therefore in our approach we use the Howland current pump (183), which is illustrated in Figure 3.3. The Howland current pump consists of an Operational amplifier (Opamp) and provides constant current with high output impedance. This allows the supply of a constant DC current into various connected loads independent of their resistivity (up to a specific threshold). In Figure 3.3, V_{ref} denotes a reference voltage which is a fraction of the Opamp supply voltage. This is obtained using a voltage divider and another Opamp in negative feedback to ensure stability and a high output impedance. R_1, R_2, R_3 and R_4 are resistors used to obtain a specific current value. We choose the following configuration for these resistors:

$$R_3/R_2 = R_4/R_1 \tag{3.2}$$

This is motivated by the fact that in the case of an ideal Opamp, the output impedance of the source becomes infinite when the resistors satisfy Eq. 3.2. The current supplied to the *Load* can be expressed as:

$$I_l = V_{Ref}/R_1 \tag{3.3}$$

The configuration presented in Eq. 3.2 can provides constant current up to a specific load threshold. This is $Load < V_{out_{max}}/2I_l$, where $V_{out_{max}}$ is the maximum

voltage output of the Opamp before saturation. Because $V^+ < V_{out}/2$ and $V^+ = I_l Load$, as shown in the circuit in Figure 3.3 In our work we use a Rail to Rail dual-Opamp OP727 with a Common Mode Rejection Ratio (CMRR) of 85 dB, which requires a low current supply of 300 μA/amplifier. The main advantages of the Howland current pump are its simplicity, easiness of implementation, and ability to produce a high output impedance.

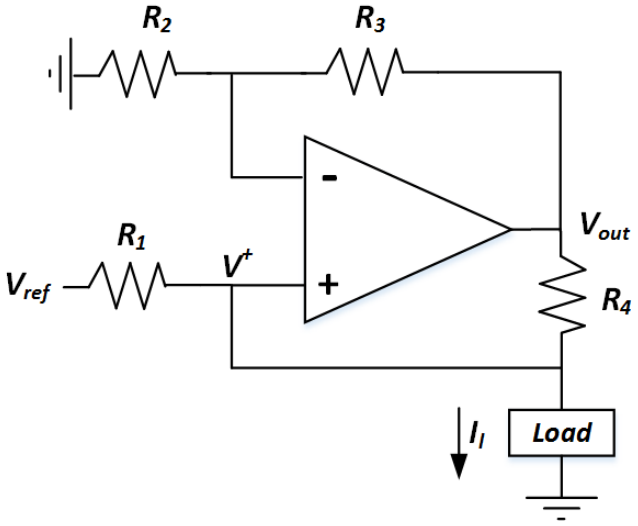

Figure 3.3: Howland current pump

The 2 multiplexers serve for switching the current supply between the electrodes. They are digitally controlled via the DAQ card which is in turn controlled via software on the PC workstation. The multiplexers are two 16:1 ADG1606, presenting a typical on resistance of 4.5O Ω and a transition time of 143 ns when switching from one address state to another. With 16 channels the multiplexers need to be controlled using 5 bit digital variables where 1 of these bits is used for enabling. This results in a total of 10 control bits. One of the multiplexers has its input connected to the current source, while the second is connected to ground. The outputs of both multiplexers are connected to the different electrode pairs.

3.3.1.2 Data Acquisition Setup and Multiplexing

Block 1 in Figure 3.1 illustrates the data acquisition and multiplexing elements of our sensor system. The DAQ card is used for both multiplexer control, and voltage data collection. For our experimental purposes we use the NI USB-6353 DAQ card. It has high input impedance, a maximum sample rate of 1.00 MS/s,

and an ADC resolution of 16 bits. The DAQ is used for performing the differential voltage readings by connecting one analog voltage input to the positive input of the device's programmable gain instrumentation amplifier (PGIA), while another analog voltage input is connected to the negative input of the PGIA. The maximum settling time for the measurements is $8\,\mu$s. This value indicates the time required for the PGIA to amplify the analog input signal to the desired range before it is sampled by the ADC, and then switched to another input analog channel. We use the MATLAB data acquisition toolbox for managing the operations of the DAQ card. This is used for collecting and saving the data, and to generate the 10-bit digital signal which controls the two multiplexers.

The total number of collected samples S for each channel is selected via our algorithm. The data acquisition is performed concurrently with the multiplexing switching that serves for current injection. Therefore, for a system with an L number of electrodes, the number of collected samples for each sequential injection will be S/L. We denote V^b to represent the generic vector containing the raw samples S which are collected from one generic electrode pair. The differential voltages collected from each electrode pair are in the form of a matrix: $S_{mat} = \{V_1^b ... V_L^b\}$. After collecting the raw data, we proceed to the pre-processing step. This procedure is shown in Algorithm 1 and detailed next.

Algorithm 1: Tomographic voltage data set extraction algorithm

S *number of collected samples per scan*;
L *number of electrodes*;
K *number of used boundary measurements*;
k_{select} logical vector for selecting useful boundary measurements;
t_s *number of transient samples*;

input : $S \times L$ samples matrix $S_{mat} = \{V_1^b ... V_L^b\}$
output: $1 \times K$ vector of voltage measurements V_m

for $i \leftarrow 1$ **to** L **by** (S/L) **do**
  $V_m \leftarrow$ compute column wise median of $S_{mat}(i + t_s$ **to** $i + (S/L))$;
end
for $i \leftarrow 1$ **to** L **do**
  $V_m \leftarrow V_m(i, k_{select})$;
end

First, each vector containing the differential voltages which were collected from an electrode pair is divided into subsections of size S/L. For each subsection we remove a number of samples t_s from the data that correspond to the number of

samples acquired before reaching static conditions. Subsequently, we compute the median on the remaining samples. The resulting value represents the voltage at that electrode pair for a specific current injection. We then discard the voltage data which correspond to the current carrying electrodes at each injection step. This is done so that we can reduce the effects of noise and contact impedance, and is achieved by using a k_{select} logical vector for selecting the useful boundary measurements depending on the type of injection-measurement protocol used. Therefore, for a generic L electrodes system, the final number of measurements at the boundary is $K = L\,(L - sk)$, where sk is the "skipping factor" that depends on the protocol used.

The final voltage data set is represented in the form of a vector V_m containing the voltage measurements: $V_m = \{V_{m1}, ..., V_{mK}\}$.

3.3.1.3 Transducer Element

The transducer element is represent by block 3 in Figure 3.1. We use a thin, stretchable, piezoresistive fabric material provided by Eeonyx. The material has a surface resistance of 30 KΩ, it is low-cost and light weight. The material is shown in Figure 3.4 a, b and is very flexible and bendable. Thus it is conformable to different surfaces and provides a pleasant "real skin feeling".

For validation purposes a 3D-printed circular frame made out of two disc layers is used to house the conductive sheet. The frame presents 16 equidistant extrusions where conductive copper stripes are placed to create the electrodes. The conductive fabric is then placed between the two discs firmly in contact with the surrounding electrodes, as shown in Figure 3.4 c. The diameter of the frame is 22 cm, and the distance between each electrode is 4.3 cm. The aim of the frame is to keep the boundary electrodes fixed while providing a flat surface for the transducer. This allows us to evaluate the performance of our system while minimising the effects of noise, electrode misplacement or motion artefacts. It also allows for the convenient replacement of the fabric material when prototyping and testing. In Chapter 5 we present a variant of the sensor that does not require the use of this hard frame.

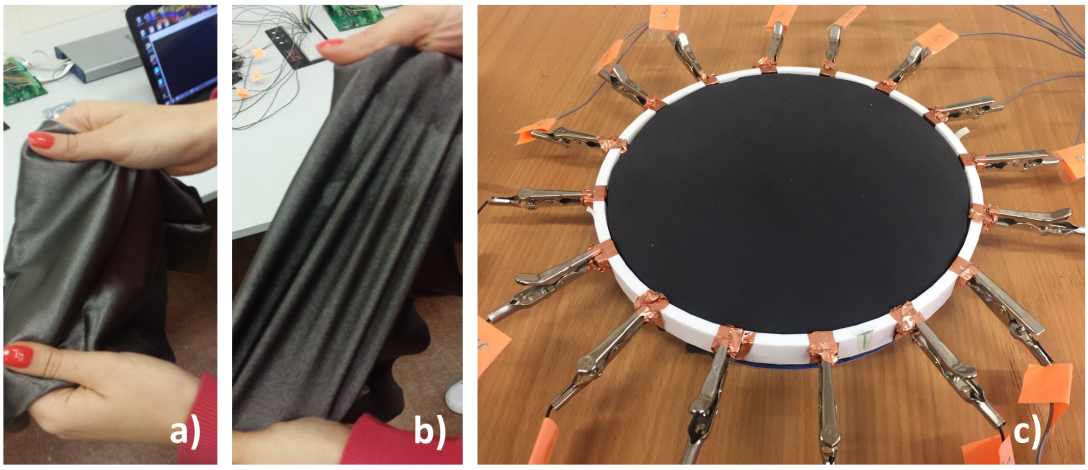

Figure 3.4: Our electrical tomography flexible fabric sensor. In (a) the conductive fabric material in shown, and in (b) the material when stretched. In (c) the conductive fabric is placed between two 3D printed discs.

3.3.2 Conductivity Reconstruction

3.3.2.1 Mathematical Formulation

The conductivity reconstruction process in electrical tomography is structured in two sub-categories: forward model computation, and inverse solution. In the forward model, an initial conductivity of the body is assumed and then the voltage data at the electrodes are calculated by solving the Laplacian elliptic partial differential equation. For a given body Ω with conductivity σ, the scalar potential is ϕ and the electric field $\mathbf{E} = -\nabla\phi$. We describe the steady-state absence of interior current sources as: $\nabla \cdot \sigma\nabla\phi = 0$. The analysis is completed with the boundary equations at the electrodes. In this work, we have used the complete electrode model:

$$\sigma\nabla\phi \cdot \boldsymbol{n} = \frac{1}{z_l}(V_l - \phi)$$

$$\int \sigma\nabla\phi \cdot \boldsymbol{n}\, \partial\Omega = 0$$

$$\sum_{l=1}^{L} I_l = 0$$

$$\sum_{l=1}^{L} V_l = 0$$

Where V_l and I_l are respectively the potential and the current at the l'th electrode, z_l is the contact impedance between the l'th electrode and the domain, and $\mathbf{n}$ is the unit normal to the periphery of the body. These differential equations are implemented by computing a Finite Element (FE) model of the system, which generates the forward operator $F(.)$ that maps the internal conductivity to the potentials at the boundary.

The second sub-category is the inverse solution. In this work, difference reconstruction methods are applied, as they are fast, non-iterative and only reconstruct dynamic conductivity changes between two time steps. Furthermore, we have employed the one-step linear GN solver, through which a minimisation technique is applied on the difference between the measured data and predicted data to obtain the approximate solution. This can be summarised by the following:

$$min(||V_m - F(\sigma)||)^2 \tag{3.4}$$

where V_m is the data set containing the potentials measured at the electrodes and $F(\sigma)$ is the conductivity distribution to be recovered through the forward operator. In order to solve Eq. 3.4, in dynamic imaging reconstruction we first calculate the initial set of boundary voltages for an assumed known initial conductivity σ_0. $F(\sigma)$ is then linearised around σ_0 in order to only reconstruct the conductivity changes $\delta\sigma$ from this initial conductivity.

$$V_m - F(\sigma_0) - \frac{\partial F(\sigma_0)}{\partial \sigma}(\sigma - \sigma_0) = 0 \tag{3.5}$$

$$\delta V \approx J\delta\sigma \tag{3.6}$$

$$\delta\sigma = J^{-1}\delta V. \tag{3.7}$$

$V_m - F(\sigma_0) = \delta V$ represents the variation in the measured potentials when a conductivity change has taken place and J is the Jacobian matrix. In this work, we determined J by adopting the calculations shown in (160), assuming a small conductivity perturbation into the FE mesh, and then solving the forward problem to the boundary changes in potential δV. There are several alternative approaches for the calculation of J. Exhaustive reviews of these can be found in (83, 28). Many entries in the Jacobian matrix have values close to zero, which creates high sensitivity to small changes in δV; this ill-conditioned problem is solved through regularisation.

Tikhonov regularisation is commonly used in electrical tomography applica-

tions and is applied in this work. Regularisation means finding a trade-off between the exact but unstable solution based on the measured data, and a more stable approximate solution controlled by an imposed prior. Here, the prior information is the assumption of smoothness of the spatial distribution of $\delta\sigma$. The formal solution through Tikhonov regularization is:

$$\delta\sigma = (J^T J + \alpha^2 R^T R)^{-1}(J^T \delta V) \tag{3.8}$$

where α is a scalar hyperparameter that controls the amount of regularisation and R is a regularisation matrix that controls the "smoothness" of the solution. There are different methods which have been developed for an optimal selection of α. Some of these are L-curve, method discrepancy principle, and generalised cross validation method (75). However in electrical tomography applications this is usually done heuristically.

For the choice of R we have employed a prior based on NOSER, an acronym for Newton's One-Step Error Reconstructor prior (118). This algorithm is based on the method of least squares, and the regularisation matrix is scaled by the sensitivity s of each element:

$$R^T R = diag[J^T J]^s \tag{3.9}$$

where $s \in [0, 1]$.

3.3.2.2 Image Reconstruction

All the parameters for the inverse solution are computed off-line, as shown in Figure 3.5. Since we are employing dynamic imaging, the images of the touch inputs over the sensor are reconstructed by comparing two voltage data sets: $V_0 = \{V_{01}, ..., V_{0K}\}$ which indicates the background set of voltages that is used as a reference; and $V_1 = \{V_{11}, ..., V_{1K}\}$ which indicates the boundary voltages measured after a conductivity change takes place due a touch input over the sensor. V_0 is obtained only once in the off-line system setup. V_1 on the other hand is updated in an online fashion.

In this work, the image reconstruction together with the numerical implementation of the forward and inverse problems are performed using EIDORS (electrical impedance tomography and diffuse optical tomography reconstruction software). This is an open source benchmark computation approach that is com-

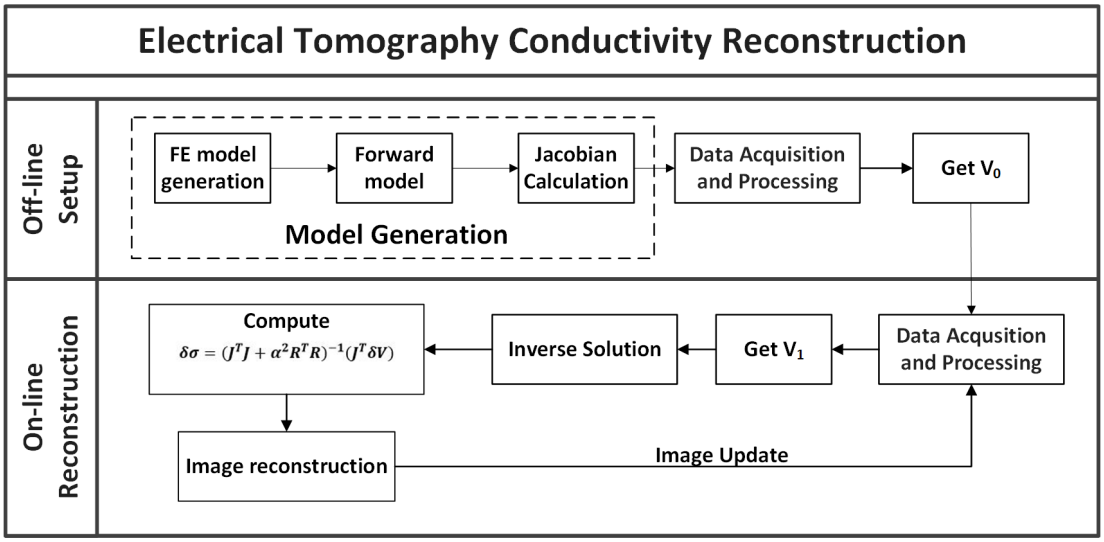

Figure 3.5: Flow chart of the image reconstruction in electrical tomography. The grey shaded boxes show the calculations done in the off-line setup of the system. Then, the second set of potentials V_1 is updated online and an image showing the conductivity changes inside the sensor is reconstructed.

monly used for electrical tomography imaging (4).

After the image ($\hat{x}_O$) which represents the conductivity changes is reconstructed, it requires post-processing as it presents artefacts due to noise and possible electrode movement. To minimise these effects, it is necessary to work on the image pixel values $[\hat{x}_O]_i$ and select the Region Of Interest (ROI) in which the maximum amount of conductivity change has taken place. The processed image ($\hat{x}_P$) is computed as follows:

$$[\hat{x_P}]_i = \begin{cases} [\hat{x_O}]_i, & \text{if} [\hat{x_O}]_i \geq f \cdot max(\hat{x_O}) \\ 0, & \text{otherwise.} \end{cases} \tag{3.10}$$

where $[\hat{x_P}]_i$ are the pixel values of ($\hat{x}_P$) and f is the threshold for the ROI selection. The ROI represents the region of ($\hat{x}_O$) where the pixels of ($\hat{x}_P$) are non zero. The choice of f has a great impact on the post-processed image, however this is commonly done in a heuristic fashion (146, 187).

3.3.2.3 Simulation Studies

Before conducting the experiments, an explorative simulation is performed to obtain a baseline for the experimental results. As illustrated in Figure 3.6, a

FE mesh of our conductive material is constructed using the physical properties of the Eeonyx fabric sample. A number of boundary electrodes equal to 16 is selected and modelled to coincide with our physical setup. A simulated touch input is applied in the central area of the mesh by simulating a change in conductivity inside the material. At this stage, the current injection and voltage measurement protocol is defined, as well as the current amplitude. A value for the hyperparameter α of 0.5 is chosen and the prior based on NOSER is also selected.

By applying the one-step linear GN solver, the software recreates the conductivity of the elements in the mesh and generates an image of the reconstructed conductivity. From the simulation results which are shown in Figure 3.6, it is visible that the simulated touch input has an influence on the conductivity changes in that area and its proximity. This is clearly demonstrating how the ability to reconstruct sharp changes in the conductivity is negatively affected by the nature of electrical tomography. Also, a light blue ring surrounding the touch input area represents the ringing artefact. This aspect is further discussed in Chapter 4.

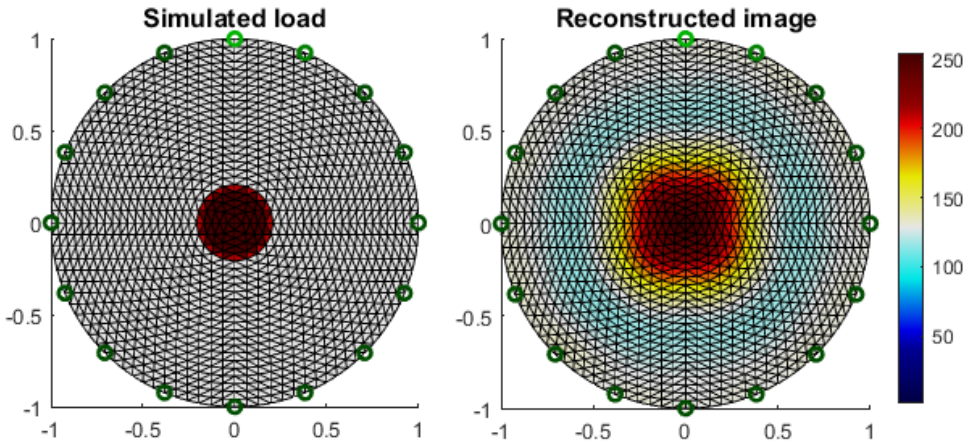

Figure 3.6: On the left, a simulated load is applied in the central area of the mesh and the reconstructed image is shown on the right.

3.4 Results

3.4.1 Experimentation

Our experimental setup consists of a 16 electrode system. We use the adjacent injection and measurement protocol which is described in Chapter 2. This protocol is chosen due to its wide usage in the electrical tomography literature. In this method, two adjacent electrodes are used for current injection, while voltage data is read between the remaining adjacent electrode pairs. Different protocols exist, a study of these can be found in (184). Also, these protocols will be further detailed in Chapter 4 along with a discussion of their performance.

When considering adjacent injection and measurement protocol, the skipping factor is $sk = 3$. Therefore, after applying the k_{select} logical vector the final voltage data set will have a dimension of $K = 208$. We use 62500 S/s as the DAQ sampling frequency. This corresponds to the fastest speed allowed by the DAQ when using 16 analog channels. This is considered as oversampling and is chosen for experimental validation purposes. We set the total number of collected samples on each analog input channel to be $S = 800$. This results in 50 samples per injection step, and guarantees that the static conditions are reached. Figure 3.7 shows an example of the voltage samples acquired through the first DAQ differential channel, namely the difference between electrodes $1 - 2$ at each current injection step. The profile of the boundary data potentials indicates the effective multiplexers' channel switching with a precise conveyance of the control digital bits. Also, the image shows that choosing $S = 800$ is enough for reaching the static conditions at each time step, and guarantees a quick switching time between the different injection steps. In fact, it is visible that the effects of transients are negligible just after a number of t_s samples equal to 25. For each current injection time step, the median value of the samples is calculated after the static conditions are reached. This is then used for creating the voltage data set V_m, and is done using Algorithm 1.

We denote the sensing rate as the rate at which the S number of samples are collected. This can be computed by dividing S by the sampling frequency per channel. In our case this corresponds to 78Hz. If we were to use a smaller number of electrodes the sensing rate would increase. This is reported in Table 3.2. However, it is worth noticing that even if a reduction in the number of electrodes greatly increases the sensing rate, this would negatively affect the spatial

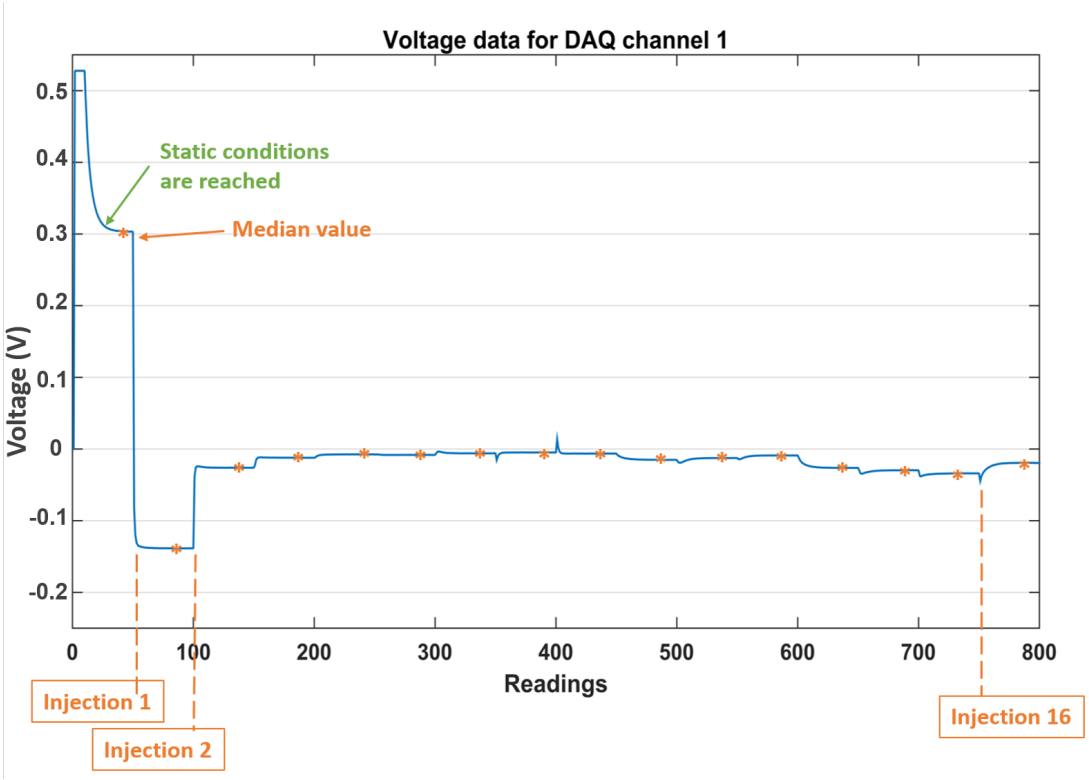

Figure 3.7: Measured voltage output signal on DAQ channel 1, obtained with 16 sequential DC current excitation signals. Median values are calculated at each injection time step for each channel after the static conditions are reached, and will contribute to create the final voltage data set.

resolution. In fact, as reported in (188), the spatial resolution is approximately 10% of the characteristic dimension of the sensor when using 16 electrodes, while an 8 electrodes system gives a resolution of 22%.

	Electrodes	
	8	16
Number of Measurements	64	256
Sensing Rate (Hz)	156	78

Table 3.2: Total number of measurements required per each scanning and the resulting sensing frame rate for different electrode counts.

In electrical tomography, the image reconstruction frame rate is the one at which the online reconstruction loop in Figure 3.5 can be executed. Therefore, this rate depends on the time necessary for the system to perform a complete cycle of electrode potentials readings, and then compute the inverse solution. Moreover, computing the inverse solution depends on the reconstruction algorithm as well as the computing performance of the workstation and is therefore beyond the scope of this thesis. An image reconstruction frame rate of 45 Hz is reported in (200) for a system consisting of 17 electrodes. In (7) a sensing rate of up to 30 Hz is reported, however the image reconstruction frame rate is not discussed. In our study, the image reconstruction frame rate is calculated to be $\simeq 30\,\mathrm{Hz}$.

We also report the power consumption of the developed system in two cases. When using a current of I=32 μA and a power supply of 16 V, this configuration gives a power consumption of about 10 mW, far lower than the ones presented in literature. This value can be further reduced to 3 mW when considering a current of 10 μA supplied via a power supply of 5 V.

In Table 3.3 the mean SNR and the Mean Absolute Deviation (MAD) among different measurement sets are shown for two tested currents of I=32 μA and I=10 μA. The results demonstrate that, if it is necessary to reduce the power consumption, the drive current amplitude can be decreased without compromising system performance in terms of noise and consistency of measurments.

3.4.2 Contact Location and Image Reconstruction

The image of the touch inputs over the sensor is reconstructed by comparing two voltage data sets: V_0 is used as a background reference and V_1 are the resulting

	Current Amplitude	
	I=32 μA	I=10 μA
SNR	55	49
MAD	0.5	0.4

Table 3.3: Mean signal to noise ratio (dB) and mean absolute deviation (mV) in the case of two different current amplitudes

potentials measured when touch is applied. This method guarantees that no initial calibration is needed.

In Figure 3.8 it is shown an example of the reconstructed image and ROI when varying the threshold factor f. It is clear how f has a great impact on the final image. This is definitely a disadvantage in electrical tomography reconstructions as case specific knowledge is required for the choice of f. In our case, we have chosen f= 0.10 for the adjacent protocol, as it was shown to be the one exhibits the best performance during experimentation.

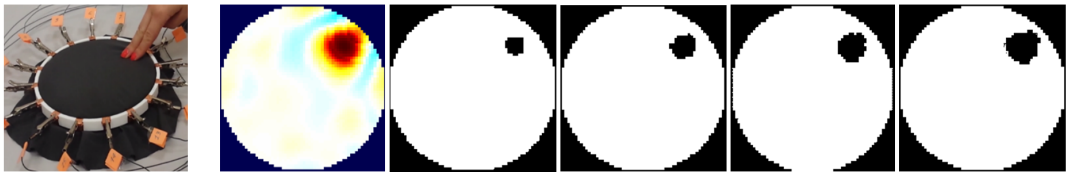

Figure 3.8: Examples of reconstructed images with different threshold factors f after a conductivity change has taken place.

Finally, in order to demonstrate the quality of the sensor system Figure 3.9 shows the reconstructed images when a touch input is applied in different positions over the sensor. In the reconstructed figures, the red colour indicates a positive changes in the conductivity, while a blue colour represents the ringing artefacts which are bands or "ghosts" near edges, and are typical of linear filters like electrical tomography systems. It appears that the location of the touch input affects the conductivity of the fabric material also in the surrounding areas. However, following our simulation results it is clear that this behaviour is mainly caused by the nature of electrical tomography. In fact, sharp conductivity changes cannot be reconstructed because of the applied regularisation. It is also worth noticing that keeping the fabric sensor and the electrodes fixed with

a supporting rigid frame can cause some stretching at the boundary, which is also recognised as a conductivity change. This further confirms the high sensitivity of electrical tomography reconstructions to small changes in potential at the boundary measurements. However, this behaviour is mainly removed in the post-processed image $\hat{x}_P$ after application of the threshold factor f.

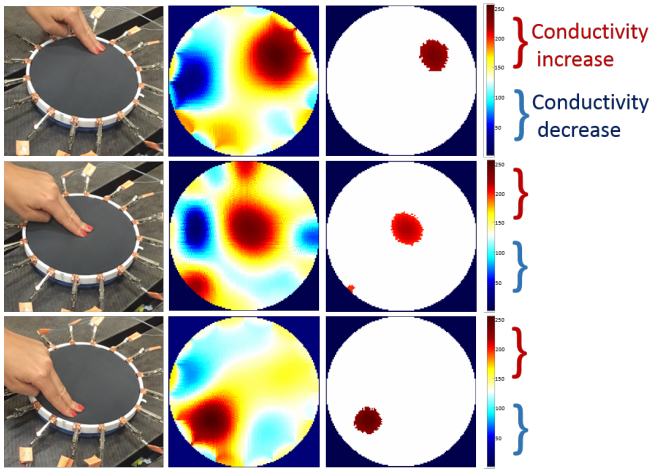

Figure 3.9: Reconstructed images for a touch input applied in different locations over the sensor. On the right, the final image showing the ROI representing the maximum conductivity change. Red colour indicates an increase in the conductivity.

3.5 Discussion

Common electrical tomography systems tend to have drawbacks such as a slow sensing rate or complicated hardware which increases power consumption and costs. In this chapter, we have presented our sensor system which comprises of: a custom Printed Circuit Board (PCB) for performing adjustable current injection and voltages measurements; data acquisition setup and multiplexing; a piezoresistive flexible fabric material which is used as the transducer element; and our approach for raw data collection, pre-processing and image reconstruction.

This system allows for the implementation of a simple hardware that reduces costs and power consumption. It also provides a frame rate adequate for dynamic scenarios found in contact applications that require real-time sensing. We show that our sensor system can provide a sensing rate up to 78 Hz when using 16 electrodes, and an image reconstruction frame rate of $\simeq$ 30 Hz, suitable for dynamic

contact applications. Consistent voltage data collection is successfully performed with a mean SNR of 55 dB, and a MAD of 0.5 mV. Also, the simple hardware design guarantees a power consumption of down to 3 mW. The system design can be configured for up to 16 electrodes with interchangeable current injection and voltage measurement protocols, which will be used for the work presented in the next chapter. Finally, touch inputs over the sensor are properly reconstructed, thereby validating the efficiency of our electrical tomography sensor system for practical contact sensor applications. Limitations and future perspectives of this work are discussed in Chapter 6.

Chapter 4

Optimal Current Injection and Voltage Measurement Protocol based on the Region of Interest

Contents

4.1 Chapter Summary

In this chapter the spatial resolution of tomography sensors is considered. This is greatly influenced by the choice of current injection and voltage measurement protocol. We introduce a novel type of protocol and study its performance along with two other commonly used protocols in electrical tomography imaging. We do this with the aim of achieving a better understanding for this choice of protocol, consequently improving the performance of our contact sensor.

We demonstrate the validity of our study by evaluating the response of the electrical tomography sensor in the case of single, and multiple input contact positions. We do this using both simulated voltage data; and experimental voltage data collected using the sensor system that is presented in the previous chapter. For evaluating the different protocols, we propose performance metrics that can be easily generalised to any electrical tomography system. Finally, we propose an extension to our work where we set the stage for future works, whereby dynamic protocol selection can be investigated.

4.2 Introduction

The spatial resolution of a tactile sensor is of course of great importance. This is especially true when the sensor is used for detecting contact location. In electrical tomography systems, the spatial resolution is greatly affected by the choice of current injection and voltage readings protocol (179, 184, 69, 54). This is because the way the current is injected and flows inside the body under examination considerably influences the transduced signal; also, choosing different boundary electrode pairs for voltage reading changes the information content of the signal. As a consequence, the reconstructed image quality varies depending on the choice of protocol.

In recent years many attempts have been made to increase the spatial resolution of a tomography system, this is typically done by optimising the injection-measurement protocols based on different performance metrics. For example, in (179) the authors study the optimal way for placing the current injection electrodes in order to maximise the voltage differences and improve the signal quality. In (88) and (6), the optimisation of current injection protocols has been studied based on the distinguishability criteria of the boundary voltage data. In (184), four bipolar injection-measurement protocols are investigated in the context of

brain electrical tomography. Optimal choice between the protocols is suggested depending on the resulting boundary voltage data, and the number of independent measurements of each protocol. In fact, a high number of independent measurements means extracting more information about the internal conductivity and helps solving the inverse reconstruction. This approach was further developed by Xu et al. (218), where the performance metrics are based on the reconstructed image quality. The authors argue that in an electrical tomography system it is more crucial to work on the algorithms for the inverse solution, rather than the protocol itself. Although this is an important factor, we still believe that optimising the current injection and voltage measurement protocol is the main deciding factor that should be considered when working with tomographic systems. This is because the protocol is responsible for the resulting tomographic signals, and therefore it presents the foundation for obtaining informative images. In the context of tomography brain imaging, the authors in (130) propose the use of a protocol which maximises the distance between the current injecting electrodes. They show that this enhances sensitivity to perturbations throughout the scanned volume, and consequently the resulting image quality.

However, the approaches considered in the above mentioned literature have not yet examined the relationship between the performance of a certain injection measurement protocol, and the Region Of Interest (ROI) where a change in conductivity is detected. By exploring this idea, in this work we aim to improve the spatial resolution of an electrical tomography system, and therefore to contribute to existing literature. With a particular focus on electrical tomography fabric sensors, we show that current injection and voltage measurement protocols respond differently to different positions of the ROI, consequently affecting the overall performance of the tomography sensor system. For doing this we consider the case of single, and multiple input contact positions. We do this by first examining simulated voltage data generated using the EIDORS benchmark software; then using the sensor system that is presented in Chapter 3. The results are then evaluated using our proposed performance metrics, which can be easily generalised to any electrical tomography system.

In the next section we discuss the theoretical considerations that are at the basis of this work. We then describe the three injection and measurement protocols which are used to perform the experimentation; we also discuss the performance metrics and experimental scenarios. We then present our findings, and conclude by setting the stage for future work, whereby dynamic protocol selection can be

investigated.

4.3 Methods

4.3.1 Theoretical Considerations

The starting point of this work is to develop a methodology by considering the physical model of our piezoresistive fabric sensor. This is necessary in order to understand how the current flows inside the material and how the different strategies for voltage measurement can influence the collected data for the image reconstruction.

The resistivity of a coated textile material depends on: the arrangement and contacts of their yarns; and the way the yarns rearrange themselves when a mechanical stimulus is applied to the fabric. This has been studied in (50, 203, 13, 12) and discussed in Section 2.3. Furthermore, following the works of (224) and (112), we assume that our conductive piezoresistive fabric behaves as an electric circuit network with a certain number of length-related and contact resistors. Here, the current flows through the continuous elements of the fibres and their contact points. When a touch input is applied over the fabric material, the gap between the conductive yarns decreases (i.e. the contact area between the knitting courses progressively increases) so there is a reduction in the overall resistance in that area. As a consequence, there is an increase in the current density through the region where a touch input is applied. Therefore, if a current injection protocol that further maximises current flow in that region is chosen, the data and image reconstruction quality would then be improved. This is further affected by the way the signal is read at the boundary electrodes, which determines its information content.

4.3.2 Current Injection and Voltage Measurement Protocols

A current injection and voltage measurement protocol is a strategy that selects the electrodes pairs on which current injection and voltage readings are performed. In a generic electrical tomography protocol, an electrode pair is chosen for current injection, in the mean time electrode pairs are systematically chosen for performing voltage measurements; this process is repeated until every electrode pair has

served for the current injection.

In this work we focus on three current injection and voltage measurement protocols. This choice of protocols is motivated next.

Adjacent protocol (AD): in the AD protocol (Figure 4.1 a), the current is injected and read between adjacent electrodes pairs. The AD protocol maximises the current flow close to the boundary electrodes. This protocol is the most common in electrical tomography applications.

Pseudo-Polar (PP) protocol: the PP protocol (Figure 4.1 b), uses almost opposite drive electrodes for current injection. The voltage readings are then measured through adjacent electrode pairs. The PP protocol presents the highest current density flow through the central area of the material.

Pseudo-Polar-Pseudo-Polar (PP-PP) protocol: in this study we introduce the PP-PP protocol (Figure 4.1 c). This protocol injects current in the same way as the PP protocol, it also performs voltage readings in that way. The PP-PP protocol has the capability of exciting and reading ample sections of the material. To the best of our knowledge, the behaviour of this protocol was never presented and studied in the electrical tomography literature.

Other types of current injection and voltage measurement protocols exist and are used in electrical tomography applications. These include trigonometric (37) and polar (opposite) (184) patterns. Trigonometric protocols, studied by Kolehmainen et al. (104) show small tolerance to errors. In trigonometric protocols voltages are measured on the current-carrying electrodes, which creates a high sensitivity to contact impedance mismatch. In polar protocols, the current injecting electrodes are 180° apart. This approach increases the area in which the current is flowing, however it reduces the number of independent measurements due to the reciprocity principle. This affects the amount of information available for conductivity reconstruction.

Following the theoretical considerations and the three current injection and voltage measurement protocols presented above, we can conclude that if the ROI is close to the electrodes, the AD protocol can maximise the current density that flows through it. This improves the image reconstruction result. In the PP protocol, the current density is higher across the centre of the conductive medium. Therefore, this protocol will show a better reconstruction when the ROI is more central. Finally, in the PP-PP protocol the current distribution is the same as

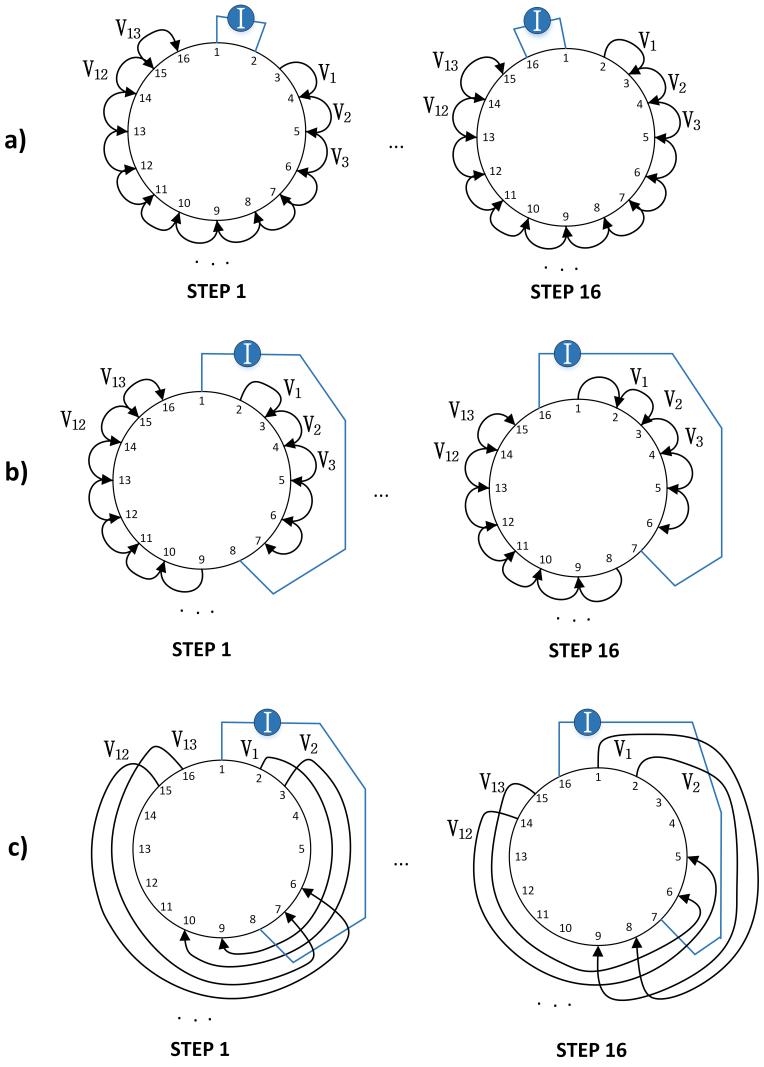

Figure 4.1: From top to bottom, the first and last of sixteen steps for the (**a**) AD, (**b**) PP and (**c**) PP-PP protocols for a 16 electrode system. For each injection step, current is applied between a pair of electrodes and the resulting voltage is measured between the remaining pairs. The current excitation and voltage measurement is then rotated until the last step.

the PP protocol, but the portion of the material being read is higher. Therefore, in the case of simultaneous multiple ROIs, where the conductivity changes are more distributed, this protocol is expected to result in an improved performance. This is because this protocol would maximise the current magnitude in the ROI and probe it from a greater field of view.

4.3.3 Performance Metrics

For evaluating the performance of the above protocols, we propose performance metrics by taking inspiration from the works of Xu et al. (218) and Yasin et al. (220). These metrics are used for image and data quality analysis; and allow us to compare the results of the three current injection and voltage measurement protocols when different ROIs are considered.

Voltage-based metrics are used to study data accuracy of the boundary voltage. Then, image-based metrics characterise the exactness of the reconstructed images, detectability and distinguishability of the targets.

Voltage-based metrics These metrics are applied on the voltage data that results from Algorithm 1. The data is in the form of a vector V_m containing voltage measurements $V_m = \{V_{m1}, ..., V_{mK}\}$.

The first performance metric which defines the quality of the signal is SNR. This has been defined in Eq. 3.1.

Then, based on the distinguishability criterion (88), we assess the performance of a protocol using our Boundary Voltage Change (BVC) metric:

$$BVC = ||V^1 - V^0|| \tag{4.1}$$

where $||.||$ denotes the Euclidean norm, V^0 denotes the voltage vector measured before conductivity changes takes place, and V^1 denotes the voltage vector measured after conductivity changes takes place. The principle is that a larger BVC indicates better protocol performance.

Image-based metrics These performance metrics are shown in Figure 4.2. They are used for assessing the quality of the reconstructed image ,and can be employed for single and simultaneous multiple ROIs. The metrics are applied on the reconstructed processed image ($\hat{x}_P$) using Eq. 3.10. Here, the ROI is found by selecting the area of the reconstructed image in which the maximum amount of

conductivity change has taken place. This selection is performed using a certain threshold factor f.

Size Error (SE) measures the difference between the Detected (DSO) and the real (SO) Size of the Object, compared to the Area of the entire Conductive Medium (A_{CM}):

$$SE = \left| \frac{DSO - SO}{A_{CM}} \right| \tag{4.2}$$

where the DSO is obtained by calculating the number of pixels in the ROI.

Position Error (PE) shows the mismatch between the detected position of the object and its real position. This is calculated as:

$$PE = |r_r - r_d| \tag{4.3}$$

where r_r and r_d indicate the real and estimated positions of the object respectively. Since r_r and r_d are found by extracting the centroid of the pixels contained in the ROI, the PE metric does not depend significantly on the choice of the threshold factor f.

Electrical tomography reconstructed images generally present an arc of light blue around the ROI. Ringing is typical of linear filters, caused by the overshoot-undershoot behaviour of the system: the conductivity change creates an overshoot in its values, then the response bounces back below the steady-state level, causing the first ring, it then oscillates back and forth above and below the steady-state level. The Ringing (RNG) metric measures the amount of these bands or "ghosts" of opposite sign surrounding the main reconstructed target area. RNG is calculated by measuring the area of opposite sign A_{INV} surrounding the reconstructed target:

$$RNG = \frac{A_{INV}}{A_{CM} - DSO} \tag{4.4}$$

Desired RNG values are small and uniform, because ringing artefacts might interfere with the detection of contact points.

The above performance metrics are independent of data collection rate, current amplitude, frequency, protocol, and number of contact positions. As a result, this evaluation approach can be easily generalised to specify the performance of different electrical tomographic applications.

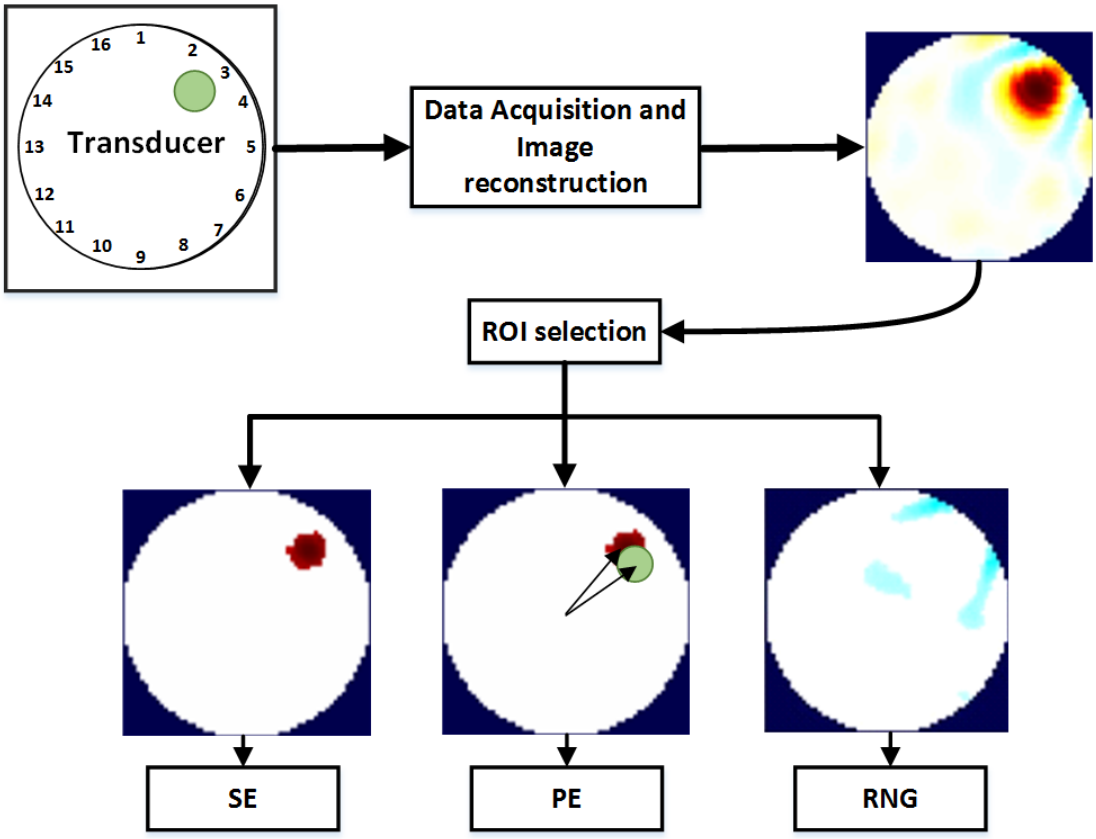

Figure 4.2: Performance metrics for the reconstructed image. On the top left, the tomography sensor, and in green the target placed over it. After the voltage data is acquired, the image of the conductivity change is reconstructed (top right, ($\hat{x_O}$)). Then the ROI is selected and the SE, PE and RNG metrics are calculated from the post-processed image ($\hat{x_P}$).

4.3.4 Experimental Scenario

The sensor system used for performing experimentation is the one introduced in Chapter 3. A 3D-printed circular frame is used to firmly hold the conductive sheet. 16 extrusions on the frame present conductive copper stripes to create the electrodes. This setup minimises the effects of noise, electrode misplacement or motion artefacts. Our custom PCB, together with a DAQ and a PC workstation are used to perform the current injection and voltage measurements. In particular, our PCB design and multiplexing management system allows us to easily switch between different injection and measurement protocols when performing our experiments. This is especially advantageous for the goal of this study. The image reconstruction is performed following our approach which is discussed in Section 3.3.2.

Five different experimental scenarios are considered. Figure 4.3 shows the scenario presenting 4 one-point inputs, and the scenario with a two-point simultaneous input. Each scenario corresponds to an input target applied at on of the following positions $x = 0.75, x = 0.5, x = 0.25, x = 0$ with a constant $y = 0$. The last experiment is the simultaneous two-point touch inputs at locations $x1 = -0.5$ and $x2 = 0.5$. The input target is 1.46% the size of the conductive medium and corresponds to an applied pressure of 20 kPa.
Each one of these scenarios has been tested with the three current injection and voltage measurement protocols presented in Section 4.3.2. The goal of these experiments is to show that the protocols respond differently for different positions of the ROI, affecting the overall performance of the tomography sensor system.

Although some studies are conducted with the purpose of finding the correct choice of the threshold factor (146, 187), heuristic selection is still very common. Also different protocols behave differently, and so using a post-processing technique is needed to fairly compare the performance of one protocol with the others when considering their dependency on the ROI, as is the case in this study. Therefore in our experimentation the selected threshold factors are $f = 0.10$, 0.08 and 0.05 for AD, PP and PP-PP protocols respectively. These values are the ones that performed best on average in terms of size detection of the ROI.

4.3.5 Simulation Studies

A simulation study using the EIDORS benchmark software is carried out to obtain a baseline for the experimental results. We considered a 16-electrodes circular

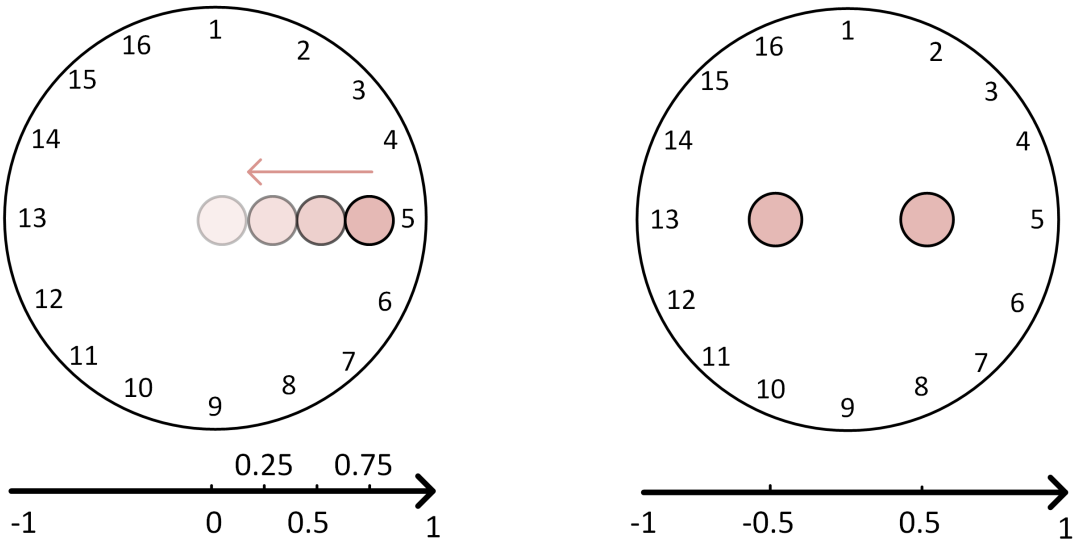

Figure 4.3: The experiments are conducted with the target applied each time step at x= 0.75, x= 0.5, x= 0.25 and finally at x= 0. The last experiment is the simultaneous two-point touch inputs at locations x1= -0.5 and x2= 0.5.

shaped phantom which models our sensor system. A FE mesh structure is used to solve the forward and inverse problems, and is constructed using the physical characteristics of the Eeonyx fabric sample.

The input targets are generated by simulating a change in conductivity inside the material for each experimental scenario, as described in the previous section. The simulated boundary voltages consist of V_0 and V_1, before and after the simulated conductivity change has taken place. These data sets are then used to reconstruct the tomographic image. The performance metrics are then calculated from each reconstructed image.

Table 4.1 summarises the response of SE, PE and RNG for different target locations for each injection and measurement protocol resulting from the simulated data. The SE and PE metrics are shown in % relatively to the size of the sensor. For better visualisation, the results in the case of single point contact location are additionally shown in Figure 4.4.

	AD			PP			PP-PP		
Position	SE	PE	RNG	SE	PE	RNG	SE	PE	RNG
x= 0.75	1.4%	0.7%	0.204	3.5%	2.3%	0.301	4.6%	7.8%	0.411
x= 0.5	1.6%	0.7%	0.197	2.8%	1.7%	0.423	3.2%	4.2%	0.401
x= 0.25	3.0%	0.8%	0.340	1.6%	1.7%	0.471	3.3%	6.3%	0.432
x= 0	4.2%	1.1%	0.370	1.1%	1.1%	0.465	3.7%	2.5%	0.402
x1= 0.5, x2= 0.5	4.4%	23.4%	0.451	2.5%	22.6%	0.472	1.5%	14.4%	0.428

Table 4.1: Performance metrics from simulated data

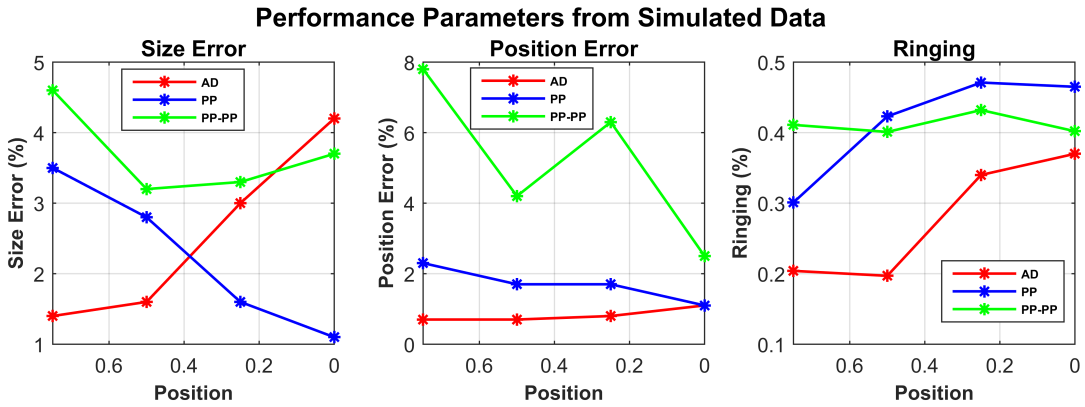

Figure 4.4: Performance metrics from simulated data are shown in the case if single point input positions.

	Protocol		
	AD	PP	PP-PP
SNR	54.98	58.93	76.06

Table 4.2: Signal to Noise Ratio (dB) for the three different current injection and voltage measurement protocols

	Protocol		
Position	AD	PP	PP-PP
x= 0.75	55	182	587
x= 0.5	52	156	900
x= 0.25	49	273	547
x= 0	16	368	697
x1 =0.5 and x2 =0.5	129	1324	1487

Table 4.3: Boundary Voltage Changes (mV) for the three different drive patterns at different target locations

4.4 Results

4.4.1 Voltage Data Metrics

Table 4.2 shows the SNR for the three current injection and voltage measurement protocols. As expected, the PP-PP protocol produces the highest signal to noise ratio. This is because the current is flowing crosswise in the sensor, and therefore through a higher number of fibres and contact points. Also, the readings are taken over an ample section of the material. The results show that the PP-PP protocol contains more information when compared to the other protocols.

The BVC values of the three protocols are shown in Table 4.3. A protocol with small BVC is more likely to be negatively influenced by the presence of noise. From the results, we can see that the BVC values for the AD protocol are small, confirming the work of (184). The PP and PP-PP protocols present higher BVC values, and thus should be considered in the case of noisy systems. These results confirm our theoretical considerations, and show that all the protocols have higher BVC values in the case of two-point contact locations. This is a result of the increased conductivity change inside the medium.

4.4.2 Image Performance Metrics

Figure 4.5 shows the reconstructed images from the experimental voltage data. It is already possible to visually identify that each protocol determines different reconstructions for the same target input location. The performance metrics are then calculated from each reconstructed image.

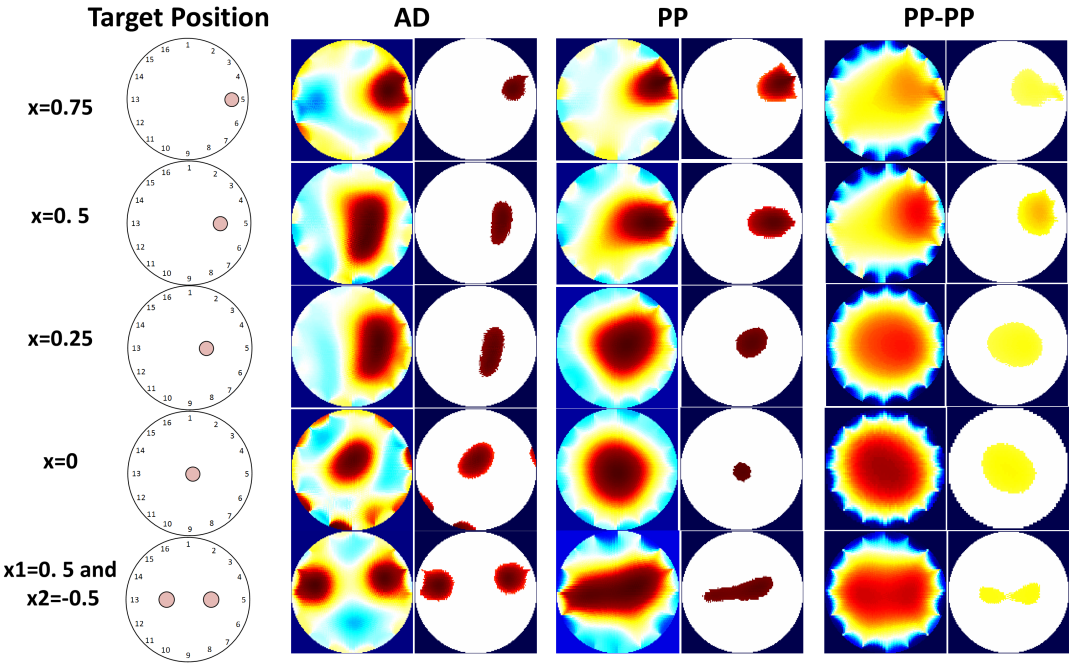

Figure 4.5: On the left, the real contact locations are shown, and for each one the reconstructed and processed images in the case of AD, PP and PP-PP protocol are presented.

Table 4.4 displays the performance metrics. For better visualisation, the results for single point contact location are also plotted in Figure 4.6. The first result to consider is that the position of the target does not influence the RNG metric, which was already visible in the results from the simulation. In fact, since the ringing effect is caused by the linear filter behaviour of the system, RNG is mainly affected by the protocol choice, rather than the position of the ROI. Also, it is known that high RNG values might cause an incorrect interpretation of the reconstructed image; this is the case for PP and PP-PP protocols, however in the case of the AD protocol we observe the lowest RNG values.

In both simulation and experimental tests the AD protocols perform better for SE and PE when the target position is close to the electrodes (x= 0.75 and x= 0.5). The PE also presents smaller variability between the different experimental

	AD			PP			PP-PP		
Position	SE	PE	RNG	SE	PE	RNG	SE	PE	RNG
x=0.75	1.8%	2.2%	0.263	3.2%	3.6%	0.332	3.1%	6.7%	0.324
x=0.5	2.0%	3.3%	0.299	2.5%	3.1%	0.313	2.3%	6.5%	0.318
x=0.25	2.6%	3.7%	0.328	1.6%	2.5%	0.396	3.4%	1.4%	0.355
x=0	3.3%	3.9%	0.300	0.6%	2.4%	0.380	5.3%	4.4%	0.369
x1=0.5, x2=0.5	1.7%	38.0%	0.353	1.3%	22.5%	0.372	1.0%	20.0%	0.361

Table 4.4: Performance metrics from experimental data

scenarios, making the interpretation of the results more reliable. This is also true for the PP protocol.

The PP protocol presents a good response for SE and PE when the target is placed in the central areas of the conductive medium (x= 0.25 and x= 0). This demonstrates its improved performance when compared to the other protocols in the same scenarios, and therefore its good sensitivity in the centre of the sensor. Lastly, when compared with the other protocols, PP-PP performs better in terms of SE and PE in the presence of two simultaneous input targets. In the other cases, the response of this protocol is quite poor. This behaviour makes the PP-PP protocol unfeasible and unstable for all scenarios but simultaneous contact locations.

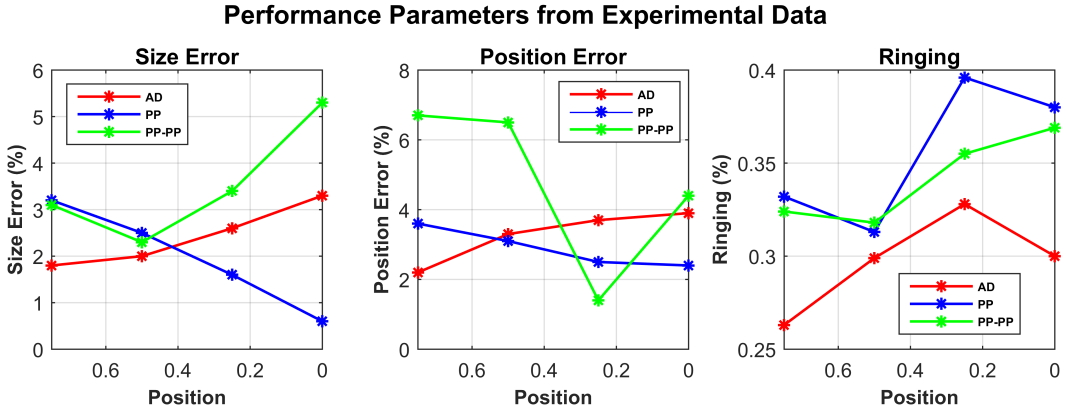

Figure 4.6: Performance metrics from experimental data are shown in the case if single point input positions.

4.4.3 Analysis

The above experimental results are in line with the simulations and follow our predictions derived from our theoretical considerations. This confirms that the response of a current injection and voltage measurement protocol depends on the position of ROI. This is also qualitatively confirmed by Figure 4.5.

Both simulation and experimental results show that the AD protocol would be preferable in the case where the ROI is positioned close to the electrodes. The reason is that this protocol has the highest current density in those areas, therefore the conductivity changes are more easily detected. Also, the response of the AD protocol is reliable in terms of PE, although the BVC values show that this protocol would not perform well in the case of noisy systems. Nevertheless, as the highest current density is found in the region close to the electrodes, this results in more sensitivity to errors in the boundary conditions. In Figure 4.5 for x=0 and x=0.75, some sort of extensive pre-stretching in the fabric material caused by our 3D printed fixture causes errors that appear in the reconstructed image. The same errors do not appear in the images from the other 2 protocols.

We have seen that the PP protocol performs better in the case where the ROI is positioned towards the centre of the sensor. By injecting current from electrodes that are almost 180° apart, the current density into the central areas of the sensor is increased. In fact, during the different injections, this protocol creates current that flows through the ROI in as many directions as possible, while also increasing the current density magnitude within it. Nonetheless, this protocol did not show a good capability in the reconstructing for multiple ROI positions.

Finally, the capability of reading ample sections of the material while increasing the magnitude of current density in the central regions of the sensor makes the PP-PP protocol useful in the case of multiple touch points, since the conductivity change is more distributed. Therefore, despite its poor response in other scenarios, this protocol can still offer advantages in the case of multiple contacts.

4.4.4 Proposed Algorithm

As a consequence of the above mentioned results, we believe that in order to improve target size detection and position accuracy of an electrical tomography sensor, it would be desirable to switch in real time between the AD, PP or PP-PP protocols depending on the position of the ROI over the sensor. This should be

done immediately upon the first detection of the ROI.

Our proposed approach is shown as a flowchart in Figure 4.7, and is detailed next.

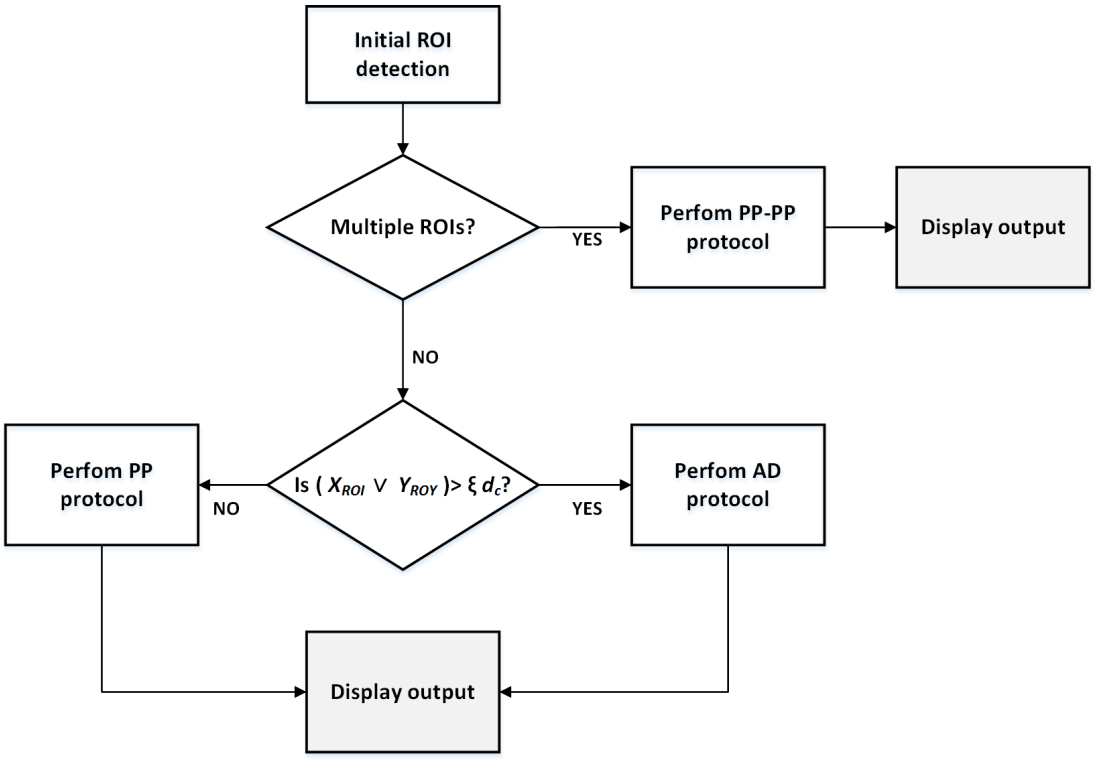

Figure 4.7: Our proposed method for dynamically adapting the current injection and voltage measurement protocols, following the identification of the ROI on the sensor

We propose that an initial ROI detection should be performed with an AD protocol. In fact, the AD protocol has shown to be the one presenting an acceptable performance in all the studied cases. Moreover, electrical tomography systems with a good temporal resolution can greatly benefit from using such an approach. This is because it will be necessary to switch between different protocols as soon as a first detection of ROI is achieved. And as shown in Chapter 3, switching between protocols and the reconstruction of a new image can be performed in less than 0.03 s, which would negligibly affect the real-time reconstruction speed of the sensor. Also, in contact sensor applications where sensory data from different sources are used, in the likes of vision systems (122, 193); the contact sensor system can be provided with information of the expected activity location over the contact sensor, our approach would then augment the precision of the overall system. Another potential application is medicine, the reason here is that knowl-

edge regarding the location of the expected ROI is generally available (202); also in such a scenario the ROI does not present quick dynamic changes.

After the initial detection of ROI, we then propose to divide the sensor area in two main sections. We define d_c as the distance between the centre of the sensor and its boundary electrodes. Therefore, a ROI that is considered in the central region of the sensor will have coordinates $x_{ROI} \vee y_{ROI} < \xi d_c$, otherwise a ROI is considered to be close to the sensor boundaries if $x_{ROI} \vee y_{ROI} \geq \xi d_c$. We propose that $\xi = 0.5$, of course a more detailed study can be imagined where the specific value of ξ is optimised.
Following this, one of the three protocols is applied: if multiple touch inputs are present, the protocol should be dynamically adapted to the PP-PP, and an image of the touch input is displayed; In the case where ROI falls in the region close to the electrodes, the AD protocol is applied. Finally, if the ROI location is closer to the central region of the sensor, the PP protocol should be applied.

Although such an approach would provide multiple advantages, some challenges arise and need to be addressed. Of these, the main ones are: How can multiple ROI positions be detected automatically? What are the consequences if the initial ROI detection is not accurate?

4.5 Discussion

A common issue in electrical tomography sensors is their low spatial resolution. It is shown through the literature that the spatial resolution is affected by the choice of current injection and voltage measurement protocols. In our work we introduced a novel type of protocol, and studied its performance along with two other commonly used protocols in electrical tomography imaging. We conducted a comparative analysis on the performance of these three protocols with regards to different ROI locations. The response of the protocols was evaluated using performance metrics that were obtained from data generated using simulation, and our sensor system.

Based on the results, both the simulations and experimentation confirmed that: a) although the AD protocol is less tolerant to noise and has a lower dynamic range, it performs better when the ROI is close to the electrodes; b) the PP protocol is preferable when the ROI is close to the central area of the sensor; and c) our proposed PP-PP protocol is mainly suitable for the detection of multiple touch inputs.

These findings can be visualised through the reconstructed images of the touch inputs, and confirm our theoretical considerations. Finally, and in light of these findings, we proposed an approach for dynamically selecting the current injection and voltage measurement protocols. This however requires further study and validation.

Chapter 5

Touch Position Identification using Discriminant Analysis

Contents

5.1 Chapter Summary

This chapter presents a method for touch position identification in an electrical tomography contact sensor. This is done by means of a supervised machine learning algorithm for performing classification, namely discriminant analysis. This approach provides accurate touch location identification, increasing the detection speed and sensor versatility when compared to traditional electrical tomography approaches.

We propose a novel data collection process for robust training of the learning algorithm. We then present a detailed study on how the system performance are dependent from parameters like number of training data, number of electrodes, dimension of the sensor, and touch position distance from the electrodes. The sensor is then applied in real world scenarios over different surfaces to show and validate the efficiency of the proposed approach.

5.2 Introduction

As discussed in previous chapters, the aim of this thesis is to develop a practical contact sensor system that can be widely used and easily integrated. We have already identified the advantages of using tomographic techniques for this purpose, see Chapter 2 for more detail. Moreover, when considering tomographic imaging, the inverse problem is traditionally solved through constructing a FE model of the system, which subsequently allows for the reconstruction of the internal conductivity of the body under examination. This creates disadvantages which were already discussed in Chapters 2 and 3.

Furthermore, relying on the FE model for solving the inverse problem greatly deteriorates the time resolution of the system. In fact, as already discussed in Chapter 3, the image reconstruction frame rates of our electrical tomography system is less than half the system's sensing rate. This is because the image reconstruction rate heavily depends on the computation time of the inverse solution. Also, as a consequence of using this approach, the reconstruction results are greatly influenced by: small variations in the measured data caused by electrical noise and electrode movements; and modelling errors which include contact impedance, electrode size, boundary shape of the sensor, and electrode misplacement. This is reported in the literature by many authors, see for example (83, 11, 104, 72). Particularly, in the context of electrical tomography flexible

sensors, modelling errors can be introduced when placing the sensor over curved, irregular or moving surfaces. For example, the boundary electrodes might be moved to positions that were not expected in the initial system model. This creates reconstruction errors in touch input position detection. Therefore, such drawbacks hinder the application of these sensors in real world scenarios.

Consequently, although traditional approaches to tomographic imaging are robust and well studied, their disadvantages stand in the way when considering the applicability aspect and wide use of flexible contact sensors. In this chapter, we propose to identify contact location on an electrical tomography sensor using an ML algorithm. This is used to classify voltage data collected that is measured by our sensor system which is presented in Chapter 3. This approach does not rely on the system FE model, thus it provides accurate touch location identification, and improved detection speed. It also promotes the application of these sensors in real world scenarios, as later shown in this chapter. ML has been recently gaining an increasing amount of attention by the tomography research community as shown in Section 2.5.2. A detailed discussion of our methodologies and developments are presented next.

5.3 Methods

5.3.1 Design Goals

Our aim is to develop an electrical tomography sensor system that is practical to implement in real world scenarios. We especially consider the possible utilisation of the contact sensor in human-interactive applications. Therefore, we determine the necessary specifications of our contact flexible sensor system as follows.

- The main objective of the sensor is to provide accurate positions for contacts on its surface.
- Essential requirements for the fabric sensor are low cost and the ability to be manufactured with commonly available tools and materials. For good integration on arbitrarily shaped surfaces, the material must be flexible, thin and light weight. Also, it should be possible to customise the shape and spatial resolution of the sensor.
- The training process for contact location identification should be easy and quick.

- The sensor needs to be able to detect touch contacts as small as the human fingertip, between 10 to 15 mm.
- Next, we consider the working range: the sensor needs to work properly under both medium- (10-100 kPa, suitable for object manipulation) and low-pressure regimes (under 10 kPa, comparable to gentle touch (132, 154)).

5.3.2 Piezoresistive Fabric Sensor

In this work we are using the piezoresistive fabric sensor from Eeonyx Corp. already presented in Chapters 2 and 3. However, compared to our previous set-up, we do not employ the 3D-printed circular frame that was used to house the conductive sheet and keep the electrodes fixed.

Here in fact, we do not use any rigid support and we directly place the electrodes for current injection and voltage readings on the fabric material. The reason behind this choice is that the resulting sensor is truly flexible and can be built with low cost, widely available materials, and low effort. Also, without the rigid frame, the position of the electrodes is not necessarily fixed, which can cause small electrode movements. This is done intentionally to further take into consideration errors that might appear in real world scenarios when placing the sensor on different surfaces.

For the electrodes, we use commonly available clip electrodes connected to the data acquisition system through a 3-ply stainless steel thread.

We also manufacture and test different sensor prototypes which are a 13x13 cm square sensor and a 17x17 cm square sensor. Each sensor is tested using 16 and 8 boundary electrodes.

5.3.3 Classification via Discriminant Analysis

Our aim is to accurately detect the position of an input touch on the sensor. Here, we approach this problem using machine learning, specifically using supervised learning for performing classification, see Section 2.5 for more detail. This is done by first acquiring data from the sensor. We then treat the surface of the sensor as a grid, whereby each cell in the grid points to a specific position on the sensor. These cell components define different touch position classes $c = 1, \ldots, C$ where C denotes the total number of classes. Moreover, when working with a sensor system, we usually acquire data with some uncertainty. These occur

mainly due to measurement error, and unforeseen changes to the system. It is therefore necessary to account for this uncertainty, and we do so by approaching our classification problem from a probabilistic point of view. This is done by using discriminant analysis, whereby a data observation X is treated as an p-dimensional random vector $X = [X_1, X_2, \ldots, X_p]$ which is assumed to be drawn from a multivariate Gaussian distribution, and where p denotes the number of features. We proceed by modelling the distribution of X in each class separately. The multivariate Gaussian density for each class is defined as:

$$f_c(x) = \frac{1}{\sqrt{(2\pi)^p |\mathbf{\Sigma}_c|}} exp(\frac{1}{2}(x - \mu_c)^T |\mathbf{\Sigma}_c|^{-1}(x - \mu_c)) \tag{5.1}$$

where μ_c denotes the p-dimensional mean vector, and Σ_c denotes the $p \times p$ covariance matrix.

The two most typical uses of discriminant analysis are Linear Discriminant Analysis (LDA), and Quadratic Discriminant Analysis (QDA) (64). The difference between these two approaches lies in the shape of the decision boundaries that is used to separate the classes. For LDA and QDA these are linear and quadratic decision boundaries respectively. This difference results from the covariance matrices that are used. If the covariance matrix is shared between all the classes, i.e. $\Sigma_c = \Sigma \, \forall \, c$, then we are discussing the case of LDA and we can therefore estimate the parameters of Eq 5.1 using our training data and the following:

$$\hat{\mu_c} = \frac{1}{n_c} \sum_{i=1}^{n_c} x_i \tag{5.2}$$

$$\hat{\Sigma} = \frac{1}{n-k} \sum_{c=1}^{C} \sum_{i;y_i=c} (x_i - \hat{\mu_k})(x_i - \hat{\mu_k})^T \tag{5.3}$$

where n_c denotes the number of observations in each class c, and n denotes the total number of observations in the training data. In the case of QDA the difference is that the covariance matrix is instead estimated for each class separately.

Afterwards, we use Bayes theorem to obtain the posterior $Pr(Y|X)$, where Y represents a random variable that takes on a specific class c.

$$Pr(Y = c|X = x) = \frac{Pr(X = x|Y = c)Pr(Y = c)}{Pr(X = x)} \tag{5.4}$$

$Pr(Y = c)$ represents the prior probability for class c, we refer to it as π_c, and

we estimate it from the training data using the following:

$$\hat{\pi}_c = \frac{n_c}{n} \tag{5.5}$$

An objective function can then be derived from Eq 5.4, see (91). In the case of LDA, the following form is obtained:

$$\delta_c(x) = x^T\Sigma - 1\mu_c - \frac{1}{2}\mu_c^T\Sigma - 1\mu_c + log(\pi_c) \tag{5.6}$$

we can see that the objective is linear in x in this case. However, for QDA the derived objective function is quadratic in x as seen in the following:

$$\delta_c(x) = x^T\Sigma_c - 1\mu_c - \frac{1}{2}\mu_c^T\Sigma_c - 1\mu_c + log(\pi_c) - \frac{1}{2}x^T\Sigma_c^{-1}x - \frac{1}{2}log(|\Sigma_c|) \tag{5.7}$$

Now can now classify new data by using $\hat{c} = argmax_c\,\delta_c(x)$. The decision boundary between each pair of classes c_i and c_j is then described by an equation $\{x : \delta_i(x) = \delta_j(x)\}$

5.3.4 Data Collection and Feature Extraction

In this work, we employ the opposite protocol for current injection and voltage measurements, in Figure 5.1. Here, the current injecting electrodes are 180° apart, while adjacent electrode pairs are used for performing voltage readings. This approach increases the current spread inside the material, and also reduces the number of independent measurements (treated in this work as features) due to the reciprocity principle (73). While a reduction in the number of independent measurements is usually considered a drawback (184), in our case this results in a dimensionality reduction of the features, and is very useful when training the ML classifier, since complexity and training time of the classification model are reduced. This has direct implications in the specific case of QDA, where the covariance matrices are of size $p \times p$.
Using an opposite protocol, the total number of independent features is $p = L\,(L-4)/2$, where L stands for the number of electrodes. Therefore when considering 16 and 8 electrode sensor systems, we have $p = 96$ and $p = 32$ respectively.

The tests presented here are performed using our custom PCB, together with the DAQ and a PC workstation, as described in Chapter 3. A flat circular target representing the human fingertip was used to apply a touch input over the classes

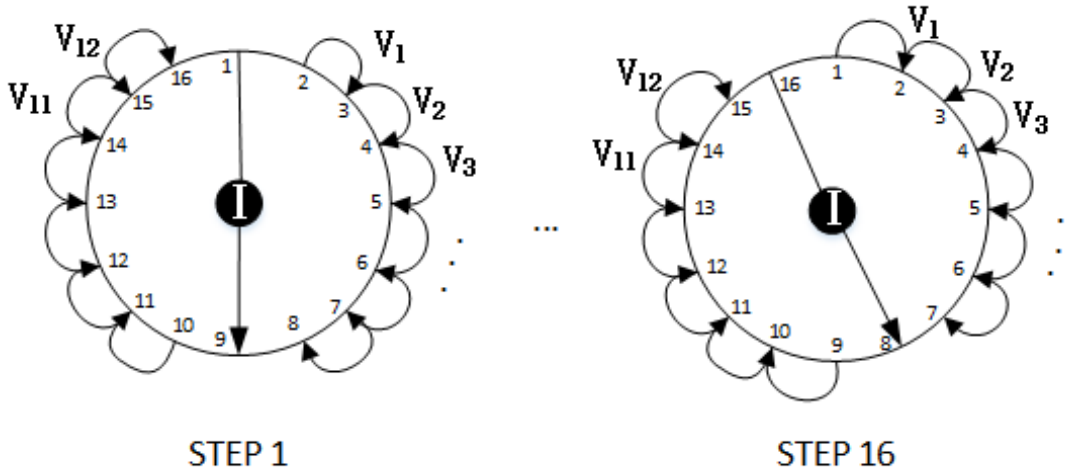

Figure 5.1: A typical electrical tomography current injection and voltage measurement cycle in the opposite pattern.

to be tested. Two different targets of size 15 mm and 10 mm were used during the tests resulting in respectively 49 and 100 classes, as shown in 5.2. This is performed for the two different sensor dimensions and in the case of 16 and 8 electrodes. The target classes are precisely defined on the sensor by placing a paper grid on the fabric.

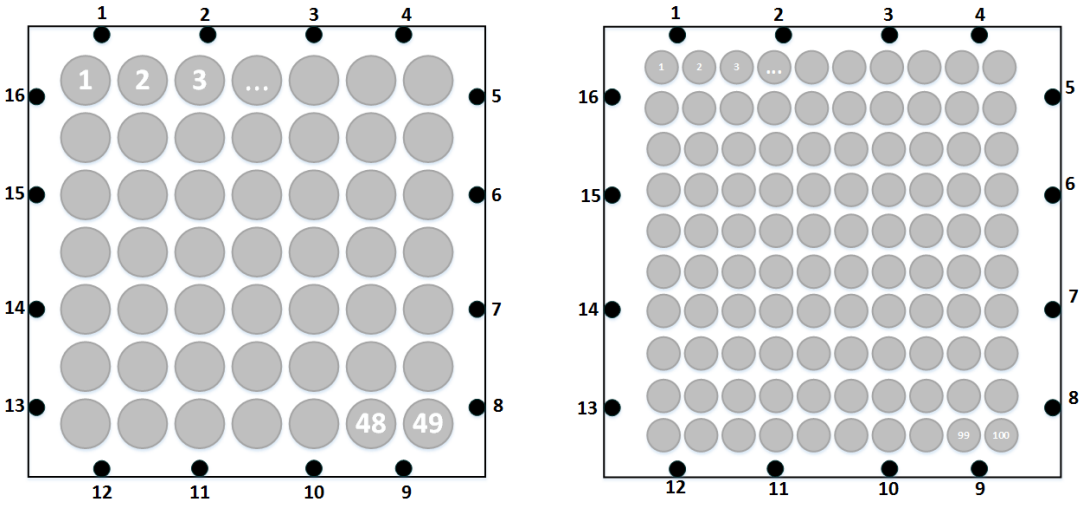

Figure 5.2: On the left, touch inputs for a 1.5 cm target (49 classes) and on the right, a 1 cm target (100 classes) in the case of 16 electrodes.

During the tests, for each touch input presented to the sensor, we acquire S_{num}=20 number of scans, with S=3200 samples for each scan at 10kHz sampling rate. Even if the acquisition could be performed at higher sampling rate, we have

limited it to 10kHz in order to ensure a good SNR. This process takes less than 15 seconds for each class.
During this time period, the target is used to apply a variable pressure touch input. First, a small weight is placed on top of the target to guarantee that a minimum pressure of less than 10 kPa is achieved. Then, the applied pressure over each class is varied manually. At this step we are not searching for a high precision because we want to have a high variety of data. This allows the resulting trained ML algorithm to identify touch input locations independently of their pressure values. The purpose behind this choice is that we are trying to cover a certain range of pressure sensitivity (Section 5.3.1).
Then, after S_{num} scans are completed, the target is applied on the next class and the process is repeated until all the input classes are tested. The full process is finally repeated for T=6 times. The entire data acquisition takes about 1 hour.

In order to form the training matrix, once the raw data are collected, we then divide the samples in S_{sub} subsections of 160 samples each and perform the median as described in Chapter 3. This step provides further robustness to the classification algorithm as it is able to train on a even higher variety of data, giving stability to noise. Also it helps taking into account small dynamic issues as elastic return, or hysteresis effect that are present between the application of variable pressures. Finally, the number of observations n_c per each class becomes:

$$n_c = TS_{num}S_{sub}. \tag{5.8}$$

In our case, n_c= 2400. The process described above is reported in Algorithms 2 and 3.
For the test data, 20 test data for each class were acquired 1 day after the training process. Each test data is acquired following Algorithm 1 described in Chapter 3 and is a touch input over the sensor with an unknown pressure. This is performed to test and show that the final ML algorithm is able to identify touch input locations independently of their pressure values. Also, this training technique can be easily performed by any user, without requiring sophisticated hardware.

5.3.5 Training

During the training process of the ML algorithm, a segment of validation data set is divided from the training data and used to validate the model. This estimates how well the model has been trained and its properties.

Algorithm 2: Training data algorithm, first part

S *number of collected samples per scan*;
S_{num} *number of scans per test*;
C *number of position classes*;
T *number of tests*;
L *number of electrodes*;
S_{sub} constant used for dividing samples into sub sections;

input : $1 \times (C * T)$ vector container $data_{con}$ of all readings, where each element consists of a $(S_{num} * S) \times L$ measurement matrix

output: $1 \times C$ vector container $median_{cont}$, where each element represents a class, and consists of a $(S_{sub} * S_{num} * T * L) \times L$ matrix of sample medians

Stacking tests per class;
for $j \leftarrow 1$ **to** C **do**
    $cnt \leftarrow 1$;
    for $j \leftarrow i$ **to** $C * T$ **by** C **do**
        $data_{pc}\{cnt, j\} \leftarrow C\{i\}$;
        $cnt \leftarrow cnt + 1$;
    end
end
Computing a container of median values;
$div_{ratio} \leftarrow S/S_{sub}$;
for $j \leftarrow 1$ **to** C **do**
    $tmp3 \leftarrow$empty;
    for $i \leftarrow 1$ **to** T **do**
        $tmp1 \leftarrow$ empty;
        $tmp2 \leftarrow$ empty;
        for $k \leftarrow 1$ **to** $S_{num} * S$ **by** div_{ratio} **do**
            $tmp \leftarrow$ compute column wise median of
              $data_{pc}\{i, j\}(k$ **to** $k + div_{ratio} - 1)$;
            $tmp2 \leftarrow$ stack tmp horizontally;
        end
        $tmp3 \leftarrow$ stack $tmp2$ horizontally;
    end
    $median_{cont}\{j\} \leftarrow tmp3$;
end

Algorithm 3: Training data algorithm, second part

S *number of collected samples per scan*;
C *number of position classes*;
T *number of tests*;
S_{num} *number scans per test*;
k_{select} logical vector for selecting useful boundary measurements;
S_{sub} constant used for dividing samples into sub sections;

input : $1 \times L$ vector container $median_{cont}$, where each element represents a class, and consists of a $(S_{sub} * S_{num} * T * L) \times L$ matrix of sample medians

output: $(C * T * S_{num} * S_{sub}) \times (k_{select}/2)$ matrix used for training the classifier ml_{mat}

Computing a container of features;
for $j \leftarrow 1$ **to** C **do**
  $tmp1 \leftarrow$ empty;
  $tmp2 \leftarrow$ empty;
  for $i \leftarrow 1$ **to** S_{sub} **do**
    for $k \leftarrow 1$ **to** $S * S_{num}$ **by** S_{sub} **do**
      $tmp1 \leftarrow$ stack $median_{cont}\{j\}(k, all)$ vertically;
      if *length*$(tmp1)$ *is equal to* L^2 **then**
        $tmp2 \leftarrow$ stack $tmp1$ horizontally;
        $tmp1 \leftarrow$ empty;
      end
    end
  end
  $feature_{cont}\{j\} \leftarrow tmp2(all, k_{select}/2)$;
end
Computing the machine learning matrix;
for $j \leftarrow 1$ **to** C **do**
  $tmp \leftarrow$ a $(S_{sub} * S_{num} * T) \times 1$ column vector of $1 * j$;
  $tmp \leftarrow$ stack $feature_{cont}\{j\}$ vertically;
  $ml_{mat} \leftarrow$ stack tmp horizontally;
  $tmp \leftarrow$ empty;
end

When having adequate training data, the validation segment is expected to be a good statistical representation of the entire data set. If not, the results will greatly depend on how the data was divided.
To avoid this, in this work we have used cross validation. Each time, during the training phase, the data is partitioned into k-folds, one of this is held-out for validation, the remaining are used for training. This process is then repeated k times until all the folds are used. After, the k-fold average loss is from all the folds is computed, and is used to efficiently compare the different learning algorithms. In this work, a 10-fold cross-validation is used, as it is the most common approach in data mining and machine learning (167).

It is worth mentioning that a high number of features in the data affects the training time and memory consumption, creating computationally intensive learning algorithms. Using an opposite protocol for current injection and voltage measurement reduces the number of features. Therefore our approach brings significant benefits during the training process and also results in a simple ML algorithm (26).

To sum up, the training and test data used in this work consist of: $p = 96$ features in the case of a sensor presenting $L = 16$ electrodes, and $p = 32$ features in the case of a sensor with $L = 8$ electrodes; $C = 49$ and $C = 100$ classes in the case of a target size of 1.5 cm and 1 cm respectively; $n_c = 2400$ observations for each class for training; 20 observations for each class for testing.
Our framework for training and classification for touch input identification is shown in Figure 5.3.

5.3.6 Average Euclidean Error

In this work we are dealing with a physical sensor system where the separation between each class is a 2-D distance. Therefore, only considering the training and test data classification errors might not be enough to judge the quality of the ML algorithm. This is particularly meaningful in applications where it is acceptable to misclassify two neighbour classes. Euclidean error is a good way to weight the total classification error by considering the 2-D distance between each class. The Euclidean distance between two points s and q is the length of the line segment connecting them.
We define $s = (s_1, s_2, ..., s_n)$ and $q = (q_1, q_2, ..., q_n)$ two points in the Euclidean n-space. The distance d from s to q, or from q to s is given by the Pythagorean

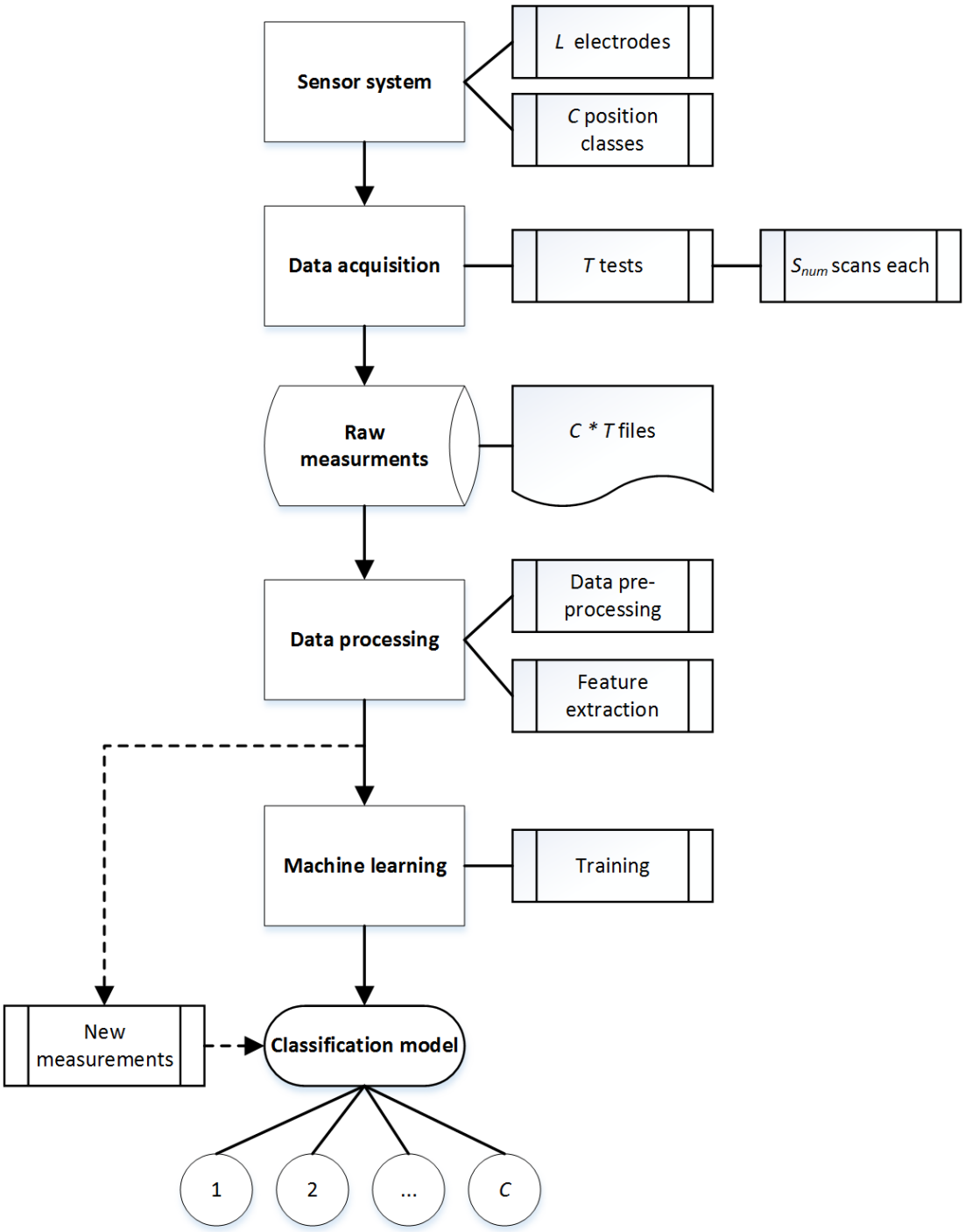

Figure 5.3: Proposed approach for touch position identification using ML

formula:

$$d(s,q) = d(q,s) = \sqrt{\sum_{i=1}^{n}(q_i - s_i)^2}. \tag{5.9}$$

We apply Eq 5.9 to each class for computing the Euclidean distance between that class and the remaining others.

The Euclidean Error EE_{tr} for each true class tr is then calculated as the Euclidean distance of the other classes from that true class, times the number of misclassifications. Given C the number of classes, and n_{pc} number of predictions per each class, we compute:

$$EE_{tr} = \sum_{c \neq tr, c=1}^{C} \left(d(tr,c) n_{pc_c}\right) \tag{5.10}$$

$$AEE = \frac{\sum EE_{tr}}{C} \tag{5.11}$$

where AEE is the Average Euclidean Error.

5.4 Results

5.4.1 Classification Methods

Before conducting our work, we have compared the performance of different learning algorithms in terms of training accuracy Tr_a and training time Tr_t. This is performed in the case of different numbers of training observations for each class: $n_c = 24$, $n_c = 240$ and $n_c = 2400$. The training observations data used to make this comparison are related to the tests conducted on $C = 49$ classes for the sensor with size 13x13 cm. The results of the comparison are shown in Table 5.1. The results show that LDA and QDA present the best performance in terms of training accuracy and time when presented with enough training data. In the other tests, their accuracy can be still considered satisfying. Also, they show short training time.

The other learning algorithms are either too slow, with up to 2.5 h training time in the case of $n_c = 2400$, or less efficient, as for example classification trees. In the next sections however, we show that the AEE on the test data is negatively affected by the number of training data already when $n_c = 240$. Therefore, using

	$n_c = 24$		$n_c = 240$		$n_c = 2400$	
ML Algorithm	Tr_a	Tr_t	Tr_a	Tr_t	Tr_a	Tr_t
Classification Trees	78.1%	3	78.8%	17	72%	74
LDA	92.1%	92	94%	9	93.8%	88
QDA	66.8%	2	99%	10	100%	81
SVM Linear	83.8%	52	99.5%	257	98.2%	2761
SVM Quadratic	92.8%	156	99%	302	99.1%	3247
KNN Classification	94.1%	181	99%	304	100%	7422
Ensamble Boosted Trees	68.8%	253	71.6%	555	73.3%	8500
Ensamble Bagged Trees	92.7%	244	99.9%	414	100%	8172
Ensamble Subspace Discriminant	91.2%	251	91.1%	412	91.2%	8172

Table 5.1: Training accuracy and training time (in seconds) for different ML classification algorithms

$n_c = 24$ is in reality of no practicality when presenting the ML algorithm with unseen data.
Based on the above results, in this work we have applied quadratic discriminant analysis.

5.4.2 Test Accuracy

First, in order to characterise the response of the QDA learner algorithm in different scenarios, we report its training accuracy Tr_a and test accuracy Te_a when changing the number of electrodes and sensor sizes.

$L = 16$ **electrodes, 13x13 cm sensor** When performing the training for $n_c = 49$ classes (1.5 cm target), QDA shows $Tr_a = 100\%$ and $Te_a = 91.6\%$.
Instead, when performing the training for $n_c = 100$ classes (1 cm target), QDA shows $Tr_a = 88.2\%$ and $Te_a = 77.8\%$. The results on the test data are shown in Figure 5.4.

$L = 16$ **electrodes, 17x17 cm sensor** In this case, when performing the training for $n_c = 49$ classes (1.5 cm target), QDA shows $Tr_a = 96.2\%$ and

$Te_a = 88.7\%$.
Instead, when performing the training for $n_c = 100$ classes (1 cm target), QDA presents $Tr_a = 95\%$ and $Te_a = 80.6\%$. This is shown in Figure 5.4.

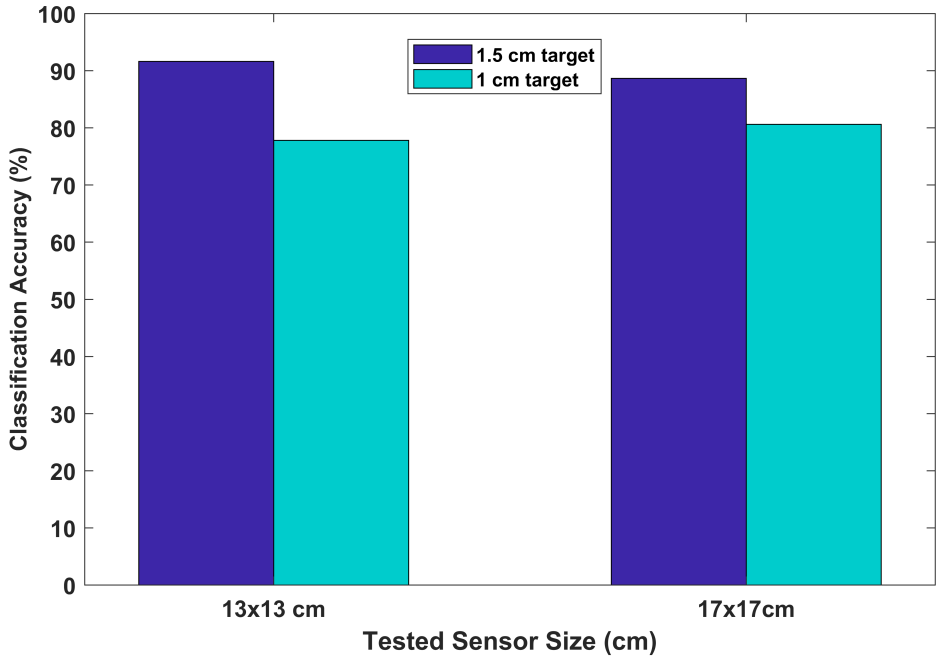

Figure 5.4: Classification accuracy on test data when changing the sensor the size for 16 electrodes.

$L = 8$ electrodes , 13x13 cm sensor When performing the training for $n_c = 49$ classes (1.5 cm target), QDA shows $Tr_a = 66.5\%$ and $Te_a = 68.98\%$
Instead, when performing the training for $n_c = 100$ classes (1 cm target), QDA shows $Tr_a = 53.0\%$ and $Te_a = 29.9\%$. This is shown in Figure 5.5.

$L = 8$ electrodes, 17x17 cm sensor Here, when performing the training for $n_c = 49$ classes (1.5 cm target), QDA shows $Tr_a = 75.2\%$ and $Te_a = 56.8\%$.
In the case of $n_c = 100$ classes (1 cm target), QDA shows $Tr_a = 66.9\%$ and $Te_a = 37.4\%$. This is shown in Figure 5.5.

5.4.3 Number of Training Data

Previously, we have compared the results of training accuracy for different learner algorithms when changing the number of training observations for each class.

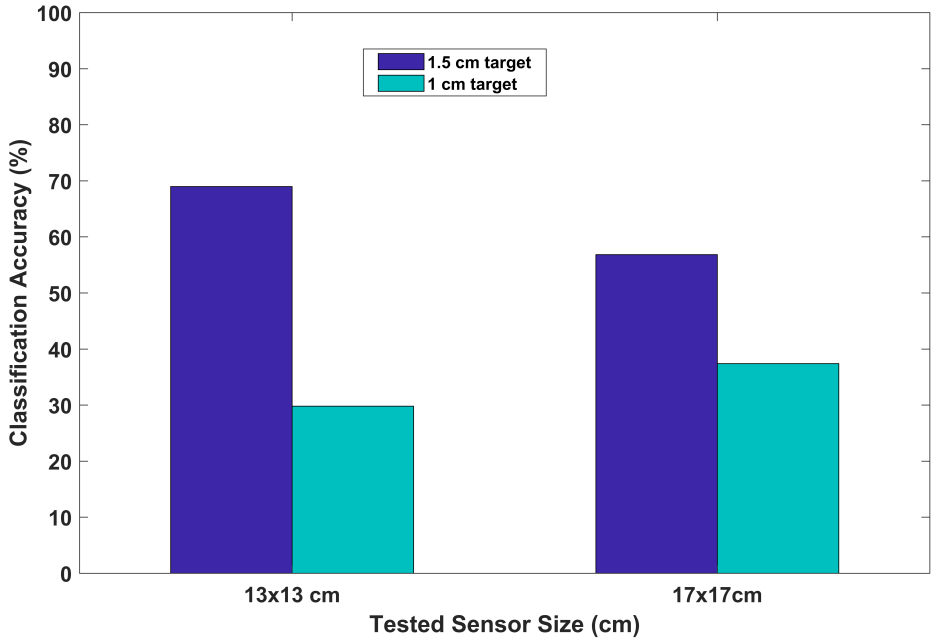

Figure 5.5: Total classification accuracy when changing the sensor size for 8 electrodes

However, it is interesting to know how the AEE changes depending on the number of training data n_c. The AEE is calculated following Eq. 5.11. For the sake of clarity, we only present here the results the sensor with size 13x13 cm with a 1.5 cm target in the case of $L = 16$ and $L = 8$ electrodes. In fact, we believe it is unnecessary to run a full test considering all our variables (sensor size, target size, number of electrodes, training data). The results are shown in Figure 5.6 and use 3 sets of observation: $n_c = 2400$, $n_c = 1200$ and $n_c = 240$. When employing less then $n_c = 240$, the results are unsatisfactory.

5.4.4 Distance from the Electrodes

AEE can be used as metric to show how the distance between each class and the boundary electrodes affects the quality of the touch input identification. For better visualisation, in Figure 5.7 the various classes are grouped with different colours based on their distance from the electrodes.

The AEE for each distance group is computed and shown in Figure 5.8. We note that the AEE tends to increase and reaches up to 10 mm the more the classes are far from the electrodes. This behaviour demonstrates an error that is not stable all over the whole sensing area and depends on the position of the

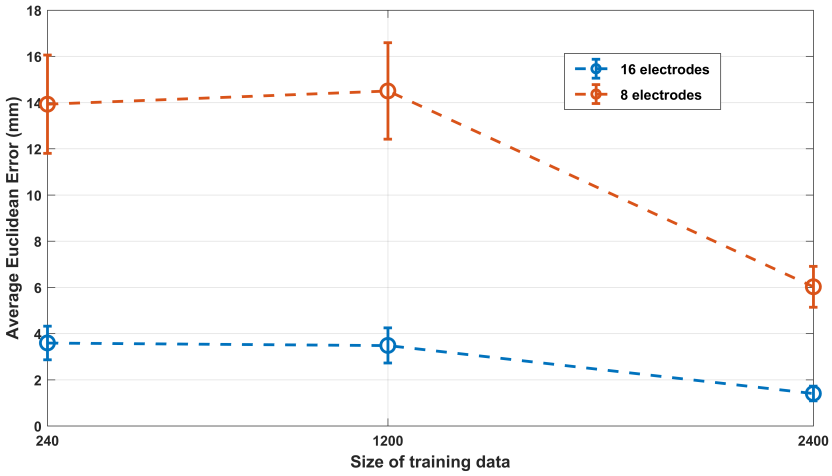

Figure 5.6: Average Euclidean Error function of different training data

target on the sensor. The AEE values range from 1 to 10 mm. This is a drawback in electrical tomography sensors, where the information content tends to decrease when the target is far from the electrodes, as a result of a reduction in the SNR. However, it is worth noticing that in Figure 5.8, the error slightly decreases in the most central region of the sensor. This is due to a a higher current density flowing in that region. This also confirms our results presented in Chapter 4.

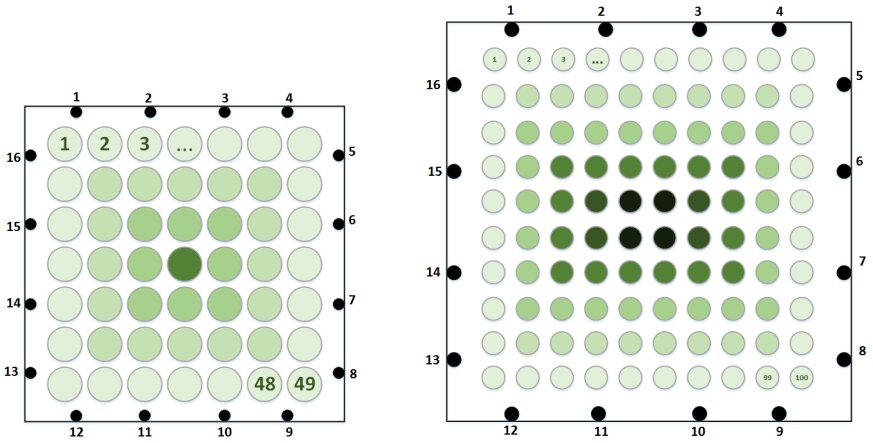

Figure 5.7: Representation of the various distances from the electrodes for the two different tested sensor sizes.

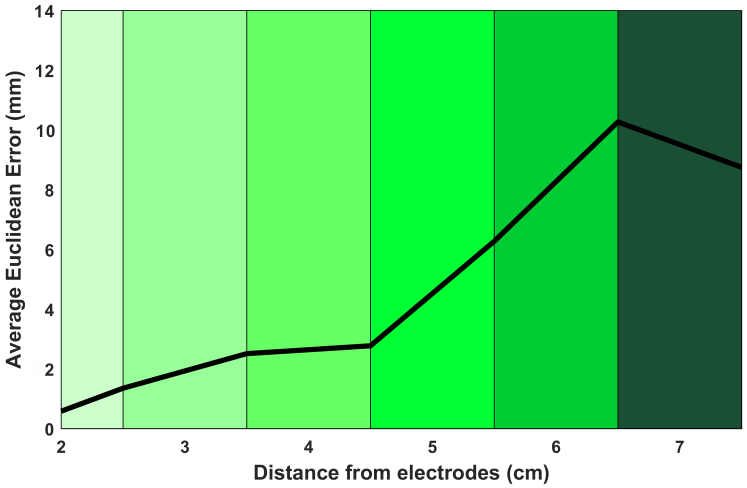

Figure 5.8: Average Euclidean Error function of the distance from the electrodes.

5.4.5 Sensor Size

The *AEE* is calculated in the case of our two different tested sensor sizes. The results are shown in Figure 5.9. From the results, it is important to note that the *AEE* does not change much in relation to the sensor size. In this case, a large error bar is indication of the high AEEs variance between the different classes, as demonstrated in Figure 5.8. These results show that, for studying the sensor's performance, it is in fact more meaningful to consider the distance between the classes and the electrodes (Figure 5.8), and not the whole sensing area. In fact, by analysing the sensitivity of the error with respect to the distance from the electrodes, we obtain a more meaningful understanding of the sensor's behaviour. This is useful when dealing with different and non symmetrical sensor shapes.

5.4.6 Number of Electrodes

The *AEE* is calculated in respect of the number of electrodes considering our two tested target and sensor sizes, and it is shown in Figure 5.10. Here, the error decreases considerably when switching from $L = 8$ to $L = 16$ electrodes, for all the considered experiments. This result was already expected. This is because when using only 8 electrodes for performing current injection and voltage measurement, there is a great decrease of information for the learning algorithm, given by the reduced features from $p = 96$ to $p = 32$.

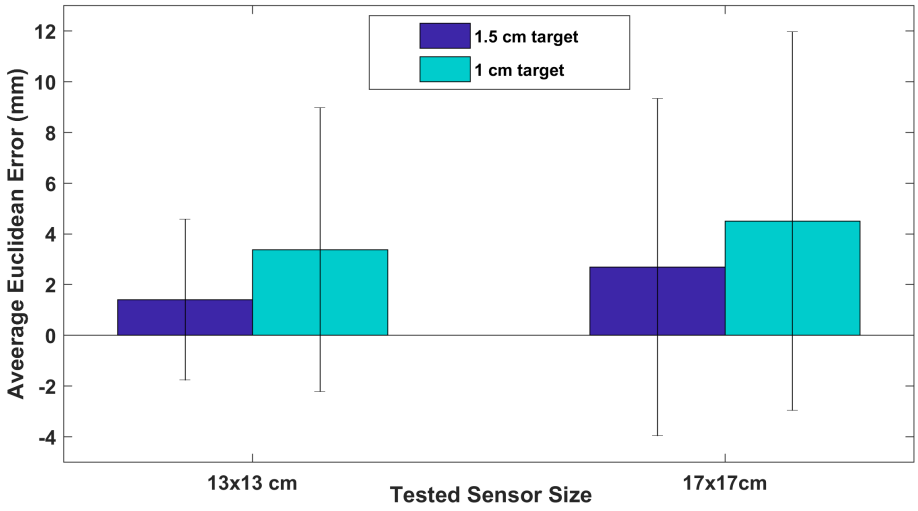

Figure 5.9: Average Euclidean Error and standard deviation when increasing the sensor size.

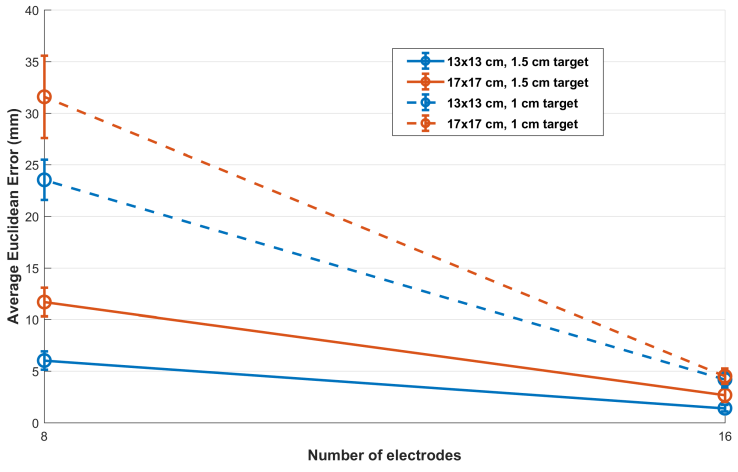

Figure 5.10: Average Euclidean Error when changing the number of electrodes.

5.5 Applications on Real Systems

In this section, apply our approach in two real world scenarios. The sensor setup and the ML classification algorithm have been implemented in two cases: when the sensor is wrapped around a curved surface; and the when sensor is placed around a robotic arm.

5.5.1 Application over a Curved Surface

The sensor is implemented over a curved surface (Figure 5.11) that has bending radius of 3 cm. Training data from $C = 14$ touch input classes are collected with the procedure explained in this chapter. Then, QDA algorithm is trained resulting in a training classification accuracy $Tr_a = 100\%$. After that, sensor data is acquired at 30 Hz sensing rate and presented to the trained classifier. The results are shown in real-time on a PC screen in the form of a matrix and can be seen in Figure 5.12. Each time a touch input class is recognised, the section the matrix corresponding to that class is illuminated with a different colour. The results confirm that the sensor is able to perform efficiently when bent over a curved surface.

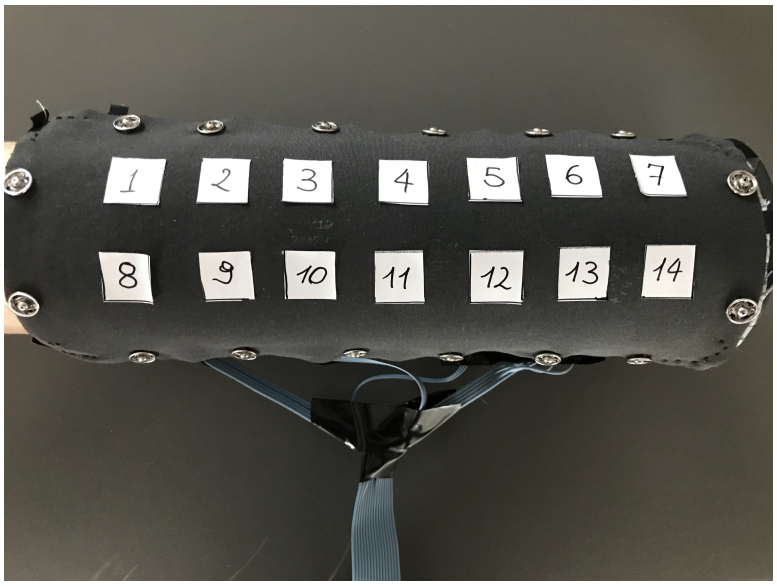

Figure 5.11: Electrical tomography flexible fabric sensor implemented over a curved surface with bending radius of 3 cm, and presenting $C = 14$ touch input classes

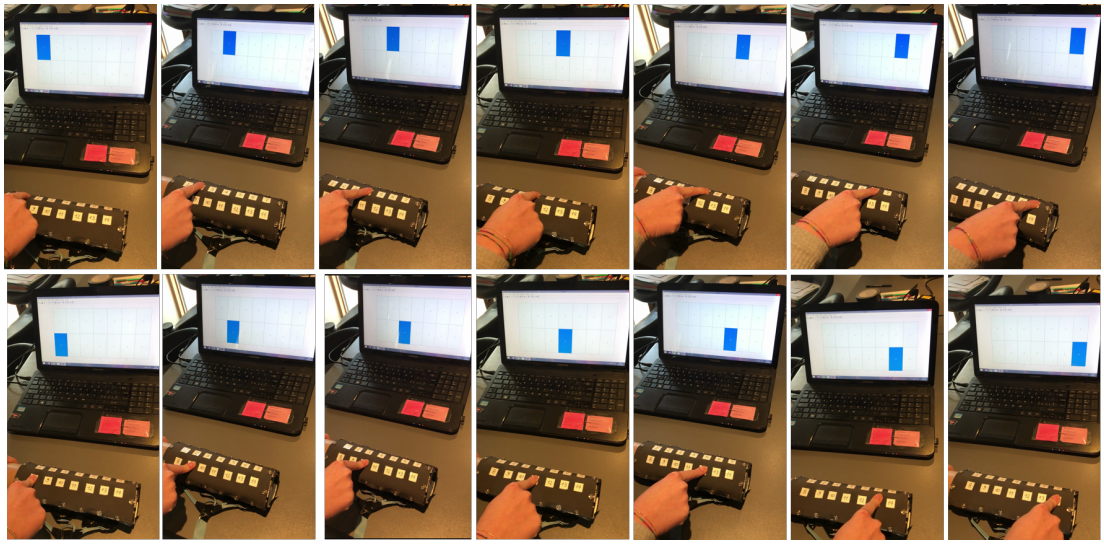

Figure 5.12: Results from test data. The trained algorithm is able to recognise correctly the different input classes.

5.5.2 Application over a Robotic Arm

The sensor is implemented over a robotic arm. The system is proposed in Figure 5.13 and comprise of:the hardware setup described in Chapter 3 with our custom PCB and a DAQ card for current injection and voltage readings, and a workstation PC for data analysis; a Kuka KR10 robotic arm which can be controlled via Matlab commands; and a 22x10 cm fabric flexible sensor with $L = 16$ electrodes. The sensor is intentionally placed with some discontinuities, to test the effective robustness of the approach.
We conducted two experiments explained below.

1. Experiment 1: training data from $C = 5$ classes are collected with the procedure explained in this chapter. Then, QDA algorithm is trained resulting in a training classification accuracy $Tr_a = 99.7\%$. The 5 classes that have been used for training are: 1 no-touch class and 4 touch classes over the sensor. After training, sensor data is acquired at 30 Hz sensing rate and presented to the trained classifier. The results are shown in real-time on a PC screen in the form of a matrix. In Figure 5.14, a full light blue matrix indicates no touch recognised. Then each time a touch input class is recognised, the section of the matrix corresponding to that class is illuminated with a different colour. The results show that the sensor is able to perform efficiently when bent over a curved surface and is able to recognise no-touch inputs.

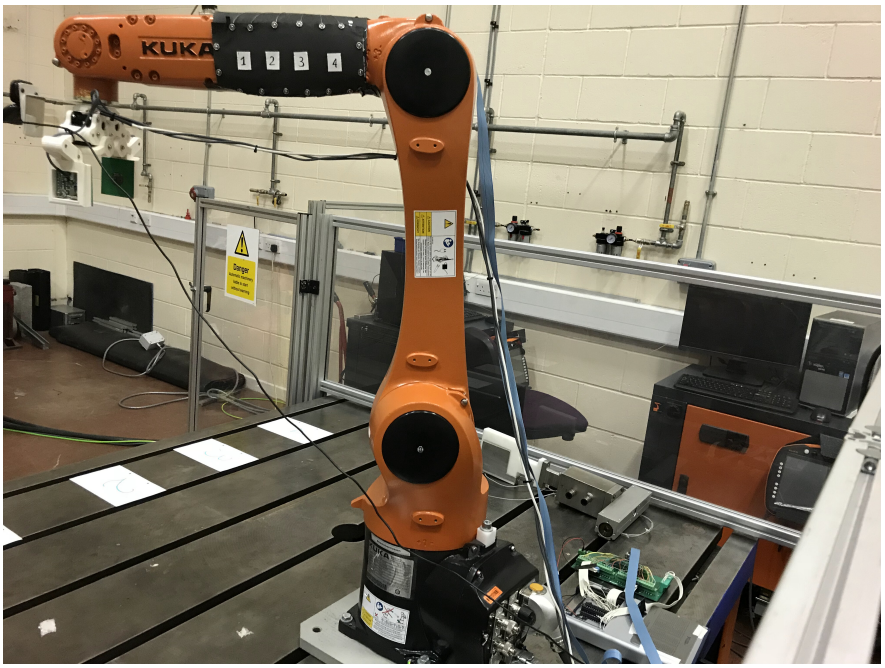

Figure 5.13: Electrical tomography flexible fabric sensor implemented over a robotic arm.

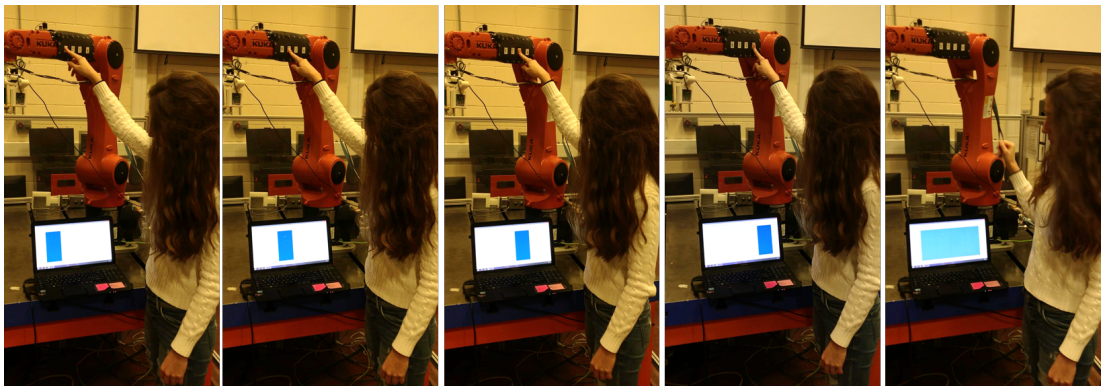

Figure 5.14: Identification of no-touch and 4 touch inputs over the Kuka robotic arm

2. Experiment 2: The Kuka robot is controlled using $C = 4$ touch inputs, which are used to send the robot to four different locations on its workbench, this is shown in Figure 5.15. The classification output is sent to the Kuka robot, where the inverse kinematics are computed to allow it to achieve the desired behaviour. The results show that the sensor can be easily placed over a robotic arm without losing its functionality, and without impeding the robot's dexterity.

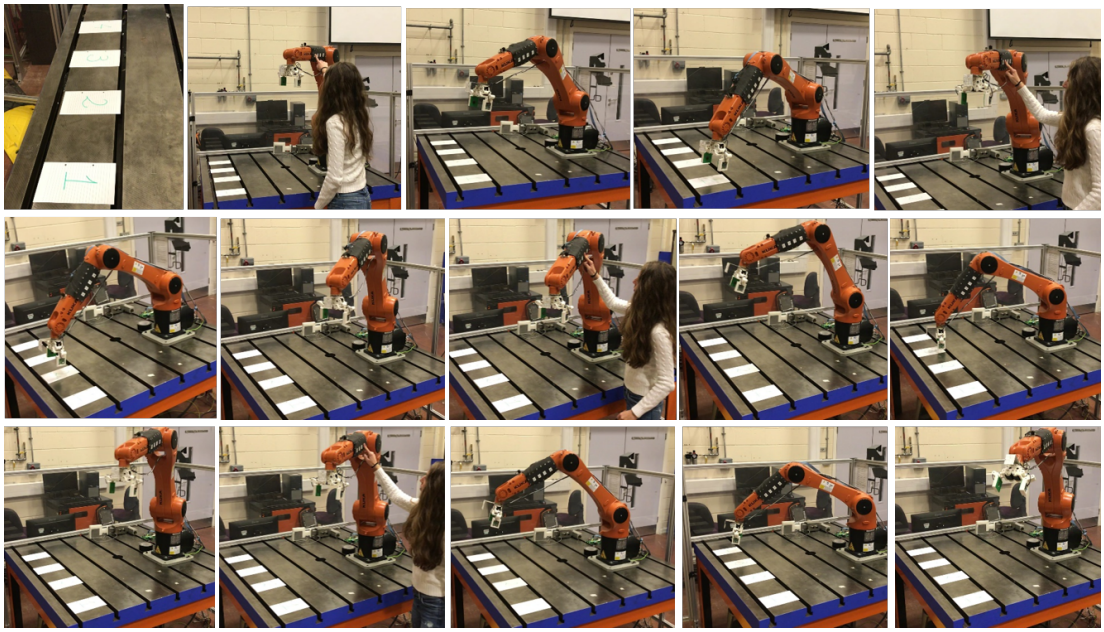

Figure 5.15: The kuka robot moving to four different locations on its workbench, being controlled by 4 touch inputs

5.6 Discussion

Electrical tomography techniques require a construction of a FE model of the sensing element for the reconstruction of the internal conductivity of the sensor. This greatly deteriorates the time resolution of the system. Also, the reconstruction results are greatly influenced by small variations in the measured data caused by electrical noise, electrode movements and modelling errors. This particularly happens when applying the sensor in real world applications. Suck drawbacks jeopardise the practicality and usage of these sensors.

To address this limitation, we use a state of the art method for accurately identifying touch positions using electrical tomography sensors. This is achieved

using supervised machine learning for performing classification, namely quadratic discriminant analysis. In this chapter, we first started by presenting our the design goals. We then described our approach to the classification problem using discriminant analysis. Next, we proposed: a novel data collection process for robustly training the machine learning algorithm; and our algorithm for feature extraction. Then, we presented a detailed study on how the system performance are dependent on the following parameters: number of electrodes; number of training data; dimension of the sensor; and distance of the touch position from the electrodes. The approach is then applied in real world applications. It is important to note that the future sensor integration in industrial workcells, is not fully addressed here, as the experiments have been carried out without protection for the operator. Therefore, future studies should be carried out in order to implement a real-time, sensor fusion approach for guaranteeing the safety of operators in close proximity to robots.

In common electrical tomography sensors, the system's frame rate greatly deteriorates due to the computation time required for the inverse solution. This drawback has been already shown in Chapter 3, where our system's speed (in terms of frame rate) is more than halved with respect to the sensing rate. Similar results are reported in (144, 187). The methodology proposed in this chapter increases detection speed. In fact, our approach potentially reaches a detection speed of 78Hz which is our system's sensing rate. This is due to the fact that once the classification algorithm is trained, the computation time for classifying new data collected by the sensor is almost instantaneous.

In addition, our approach demonstrated accurate contact location identification. When applied over curved surfaces, the flexible sensor system was also able to robustly deal with problems such as inaccurate sensor placement, electrode discontinuities, movements of the host.

As a consequence of the results shown in this work, and driven by the aim of providing a framework for a practical and easy to customise flexible sensor, we can conclude that:

- A correct number of training data is of necessary for the learning algorithm to perform accurate classification. This is already known in the ML literature. In our case, the amount of training data needed depends on parameters such as: the number of touch input classes; the algorithm chosen; and the number of features.

- If developing arbitrary sensor shapes, it is suggested to particularly focus on the maximum distance from the furthest touch input class to the electrodes, rather than just on the sensor size. In our experimental results, when a class exceeds a distance from the electrodes of 6-7 cm, the touch identification error increases greatly.

- The above behaviour confirms the idea that in electrical tomography sensors the error is not stable throughout the whole sensing area. Practitioners designing contact sensors based on electrical tomography need to be aware of this.

- In general, a number of electrodes $L = 16$ is desirable for reaching a good compromise between model complexity, data collection time and good results.

- The average error in touch input identification can be as small as 1 mm when choosing the correct design parameters. However, when the sensor and system designs are not correct, these errors can reach up to 31 mm.

Chapter 6

Conclusion

6.1 Contributions

The main thrust of this thesis is to conduct research and to develop a practical flexible contact sensor system. The research and development are detailed throughout the thesis, and are performed through means of an interdisciplinary approach whereby electronics, system engineering, electrical tomography, and machine learning have been considered.

The main body of the thesis begins with Chapter 2. This chapter plays an essential role in motivating our work, and points out the drawbacks of existing flexible tactile sensor systems. We find that these are often associated with high costs; present low accuracy and low reliability; and can have a complex structure which hinders their wide use and integration. In fact we find that the implementation of such sensor systems remains largely impractical. Also, in this chapter we identify that electrical tomographic techniques present advantages when considering such sensors. This is mainly due to the fact that electrical tomography is an imaging technique where the conductivity distribution of the body under study is reconstructed from measurements taken at electrodes placed at the boundary. This is important since it allows for eliminating the presence of wires from within the active sensing area, which enables the sensor to be easily conformable to different surfaces, without potentially losing their functionality. However, electrical tomography imaging techniques are considered ill-posed non linear inverse problems, and are very sensitive to small changes in potential at the boundary measurements. The general approach to compensate for such drawbacks is to develop systems that are precise, whereby they present a good Signal to Noise

Ratio (SNR), exhibit consistent measurements and present a high temporal resolution. Furthermore, in order to develop practical flexible contact sensors it is also desired to develop low cost uncomplicated systems that require low power consumption.

The approaches present in the literature do not address all the above mentioned requirements. In Chapter 3, we present our development of an electrical tomography sensor system which aims at addressing all these needs. We show our methods which include our sensor system along with all its elements: a custom Printed Circuit Board (PCB) for performing adjustable current injection and voltages measurements; data acquisition and multiplexing; and the transducer element. Moreover, our image reconstruction and data processing approach, along with a simulation study are presented. Experimental results are provided with a discussion about system performance. We conclude that our system allows for the implementation of a uncomplicated hardware which reduces power consumption. It also provides consistent measurements, and image reconstruction frame rate that is adequate for dynamic scenarios which can be found in real time tactile applications.

Chapter 4 is dedicated to improve the low spatial resolution of electrical tomography sensors. It is shown through the literature that the spatial resolution is affected by the choice of current injection and voltage measurement protocols. However, the relationship between the performance of a protocol and the Region Of Interest (ROI) is never examined. Therefore, with a particular focus on electrical tomography-based fabric sensors, in this chapter we show that protocols respond differently to different positions of the ROI, consequently affecting the overall performance of the tomography-based sensor system. We introduce a novel type of protocol, and along with two other commonly used protocols, we conduct a comparative analysis on their performance with regards to different ROI locations. The response of the protocols is evaluated using performance metrics that are obtained from data generated using i) a benchmark simulation software, and ii) our sensor system which is presented in Chapter 3. The findings of this chapter confirm that choosing the correct protocol can improve the performance of an electrical tomography system. We conclude the chapter with a recommendation for conducting future works, where we propose to dynamically switch between different protocols following the identification of the ROI on the sensor.

Although traditional approaches to tomographic imaging which consider the

usage of a system FE model are robust and well studied, they still present some disadvantages that stand in the way when considering the applicability aspect and wide use of flexible contact sensors. In Chapter 5, we consider a machine learning approach for detecting the contact location over the sensor. ML has been gaining popularity in the research community as we show in Section 2.5.2, and is considered to be state of the art. We present our approach that uses discriminant analysis for performing classification of different contact locations over the sensor. We propose a data collection process that allows for robust training of the learning algorithm. In addition, we present a detailed study on how the system performance is dependent on: the number of training data; the number of electrodes; the dimension of the sensor; and the distance of the touch position from the electrodes. The sensor is then applied over different surfaces to show and validate the efficiency of our approach for practical flexible contact sensor systems. The main finding of this work is that this approach provides accurate contact location identification, and increases the detection speed and sensor versatility when compared to traditional electrical tomography techniques.

6.2 Limitations and Future Perspectives

Although we present multiple contributions to the field of flexible contact sensing technologies, some challenges and issues remain as an open research topic. This opens up perspectives that can be addressed in future works.

1. Further enhancements to the electrical tomography sensor system that is presented in Chapter 3 should be considered. For example, a miniaturisation of the system, together with wireless communication could be studied for achieving better integration in real world scenarios.

2. The sensor presented in this work aims at detecting accurate contact positions over the sensor surface. However, future works should investigate techniques which can detect other stimuli such as contact force. This can be done by employing transducers that exhibit changes in conductivity due to these stimuli.

3. PPY coated fabrics are also thermos-resistive. In this particular work, temperature was almost constant during the experiments, so compensation was

not incorporated. This is necessary to be considered in practical applications where temperature compensation methods should be devised and implemented.

4. The findings in Chapter 4 led us to propose a future extension of our work, whereby dynamic protocol selection can be investigated. However, other protocol configurations can be studied, along with automatic techniques for detecting multiple inputs. Also, sensor fusion approaches should be considered.

5. Chapter 5 proposes a classification learner that discriminates between different contact positions over the sensor. This work can be further improved by integrating the capability to absolute positioning, and the detection of multiple inputs. This can be achieved using regression techniques.

6. Algorithms for mapping the tactile sensory data into artificial somatosensory representations should be investigated in future works. This step can be crucial for the effective application and utilisation of tactile information by the host system.

6.3 Closing Remarks

We strongly believe that there will be a need for integrating our work within a tactile sensing framework, whereby sensor fusion techniques can provide different types of information. It is also foreseeable that Artificial Intelligence will be the main driver for the next generation of research, and will contribute to developing a system which behaves more intelligently and can improve its knowledge of the world around it. This becomes particularly important in light of the recent demand for artificial systems which are capable of autonomously and safely operating in unstructured environments alongside humans. These systems in fact do not only need to behave intelligently, but also seamlessly co-exist, cooperate and communicate with humans.

References

[1] Electrical Conductivity in Textiles. https://spinoff.nasa.gov/Spinoff2006/ip_7.html. Accessed: 2018-03-20.

[2] Andy Adler and Robert Guardo. A neural network image reconstruction technique for electrical impedance tomography. *IEEE Transactions on Medical Imaging*, 13(4):594–600, 1994.

[3] Andy Adler and Robert Guardo. Electrical impedance tomography: regularized imaging and contrast detection. *IEEE Transactions on Medical Imaging*, 15(2):170–179, 1996.

[4] Andy Adler and William RB Lionheart. Uses and abuses of eidors: an extensible software base for eit. *Physiological Measurement*, 27(5):S25, 2006.

[5] Andy Adler, John H Arnold, Richard Bayford, Andrea Borsic, Brian Brown, Paul Dixon, Theo JC Faes, Inéz Frerichs, Hervé Gagnon, Yvo Gärber, et al. Greit: a unified approach to 2d linear eit reconstruction of lung images. *Physiological Measurement*, 30(6):S35, 2009.

[6] Andy Adler, Pascal Olivier Gaggero, and Yasheng Maimaitijiang. Adjacent stimulation and measurement patterns considered harmful. *Physiological Measurement*, 32(7):731, 2011.

[7] Hassan Alirezaei, Akihiko Nagakubo, and Yasuo Kuniyoshi. A highly stretchable tactile distribution sensor for smooth surfaced humanoids. In *7th IEEE-RAS International Conference on Humanoid Robots, 2007*, pages 167–173. IEEE, 2007.

[8] Hassan Alirezaei, Akihiko Nagakubo, and Yasuo Kuniyoshi. A tactile distribution sensor which enables stable measurement under high and dynamic

stretch. In *IEEE Symposium on 3D User Interfaces, 2009.*, pages 87–93. IEEE, 2009.

[9] Shigeru Ando and Hiroyuki Shinoda. Ultrasonic emission tactile sensing. *IEEE Control Systems*, 15(1):61–69, 1995.

[10] Karl H Andres and Monika von Düring. Morphology of cutaneous receptors. In *Somatosensory System*, pages 3–28. Springer, 1973.

[11] Yednek Asfaw and Andy Adler. Automatic detection of detached and erroneous electrodes in electrical impedance tomography. *Physiological Measurement*, 26(2):S175, 2005.

[12] Ozgur Atalay and William Richard Kennon. Knitted strain sensors: Impact of design parameters on sensing properties. *Sensors*, 14(3):4712–4730, 2014.

[13] Ozgur Atalay, William Richard Kennon, and Muhammad Dawood Husain. Textile-based weft knitted strain sensors: Effect of fabric parameters on sensor properties. *Sensors*, 13(8):11114–11127, 2013.

[14] Howard Austerlitz. *Data acquisition techniques using PCs*. Academic press, 2002.

[15] Jamshid Avloni. Electroconductive woven and non-woven fabric, December 23 2008. US Patent 7,468,332.

[16] Shiv S Baishya and Berthold Bäuml. Robust material classification with a tactile skin using deep learning. In *IEEE/RSJ International Conference on Intelligent Robots and Systems (IROS), 2016*, pages 8–15. IEEE, 2016.

[17] David C Barber and Andrew D Seagar. Fast reconstruction of resistance images. *Clinical Physics and Physiological Measurement*, 8(4A):47, 1987.

[18] David C Barber, Brian H Brown, and Ian L Freeston. Imaging spatial distributions of resistivity using applied potential tomography—apt. In *Information Processing in Medical Imaging*, pages 446–462. Springer, 1984.

[19] DC Barber and BH Brown. Recent developments in applied potential tomography-apt. In *Information Processing in Medical Imaging*, pages 106–121. Springer, 1986.

[20] Woodrow Barfield. *Fundamentals of wearable computers and augmented reality*. CRC Press, 2015.

[21] Maurice S Beck et al. *Process tomography: principles, techniques and applications*. Butterworth-Heinemann, 2012.

[22] Tushar Kanti Bera and J Nagaraju. Studying the resistivity imaging of chicken tissue phantoms with different current patterns in electrical impedance tomography (eit). *Measurement*, 45(4):663–682, 2012.

[23] Keni Bernardin, Koichi Ogawara, Katsushi Ikeuchi, and Ruediger Dillmann. A sensor fusion approach for recognizing continuous human grasping sequences using hidden markov models. *IEEE Transactions on Robotics*, 21 (1):47–57, 2005.

[24] Stephen J Bisset and Bernard Kasser. Multiple fingers contact sensing method for emulating mouse buttons and mouse operations on a touch sensor pad, October 20 1998. US Patent 5,825,352.

[25] D Bloor, Kenneth Donnelly, PJ Hands, P Laughlin, and D Lussey. A metal–polymer composite with unusual properties. *Journal of Physics D: Applied Physics*, 38(16):2851, 2005.

[26] Avrim L Blum and Pat Langley. Selection of relevant features and examples in machine learning. *Artificial Intelligence*, 97(1-2):245–271, 1997.

[27] Marc Bodenstein, Matthias David, and Klaus Markstaller. Principles of electrical impedance tomography and its clinical application. *Critical Care Medicine*, 37(2):713–724, 2009.

[28] Bernhard Brandstatter. Jacobian calculation for electrical impedance tomography based on the reciprocity principle. *IEEE Transactions on Magnetics*, 39(3):1309–1312, 2003.

[29] BH Brown and AD Seagar. The sheffield data collection system. *Clinical Physics and Physiological Measurement*, 8(4A):91, 1987.

[30] PR t Burgess and ER Perl. Cutaneous mechanoreceptors and nociceptors. In *Somatosensory System*, pages 29–78. Springer, 1973.

[31] Gereon Büscher, Risto Kõiva, Carsten Schürmann, Robert Haschke, and Helge J Ritter. Tactile dataglove with fabric-based sensors. In *12th IEEE-RAS International Conference on Humanoid Robots (Humanoids), 2012*, pages 204–209. IEEE, 2012.

[32] Gereon H Büscher, Risto Kõiva, Carsten Schürmann, Robert Haschke, and Helge J Ritter. Flexible and stretchable fabric-based tactile sensor. *Robotics and Autonomous Systems*, 63:244–252, 2015.

[33] Alec Cameron and Hugh Durrant-Whyte. A bayesian approach to optimal sensor placement. *The International Journal of Robotics Research*, 9(5): 70–88, 1990.

[34] Giorgio Cannata, Simone Denei, and Fulvio Mastrogiovanni. Tactile sensing: Steps to artificial somatosensory maps. In *RO-MAN, 2010 IEEE*, pages 576–581. IEEE, 2010.

[35] Lina M Castano and Alison B Flatau. Smart fabric sensors and e-textile technologies: a review. *Smart Materials and Structures*, 23(5):053001, 2014.

[36] Min Chen, Yin Zhang, Yong Li, Mohammad Mehedi Hassan, and Atif Alamri. Aiwac: Affective interaction through wearable computing and cloud technology. *IEEE Wireless Communications*, 22(1):20–27, 2015.

[37] Margaret Cheney, David Isaacson, Jonathan C Newell, S Simske, and J Goble. Noser: An algorithm for solving the inverse conductivity problem. *International Journal of Imaging Systems and Technology*, 2(2):66–75, 1990.

[38] Vladimir Cherepenin, A Karpov, A Korjenevsky, V Kornienko, A Mazaletskaya, D Mazourov, and D Meister. A 3d electrical impedance tomography (eit) system for breast cancer detection. *Physiological Measurement*, 22(1): 9, 2001.

[39] Vladimir A Cherepenin, Alexander Y Karpov, Alexander V Korjenevsky, Valdimir N Kornienko, Yury S Kultiasov, Mikhail B Ochapkin, Olga V Trochanova, and J David Meister. Three-dimensional eit imaging of breast tissues: system design and clinical testing. *IEEE Transactions on Medical Imaging*, 21(6):662–667, 2002.

[40] Jean-Baptiste Chossat, Hee-Sup Shin, Yong-Lae Park, and Vincent Duchaine. Soft tactile skin using an embedded ionic liquid and tomographic imaging. *Journal of Mechanisms and Robotics*, 7(2):021008, 2015.

[41] M Bishop Christopher. *PATTERN RECOGNITION AND MACHINE LEARNING.* Springer-Verlag New York, 2016.

[42] A Cirillo, F Ficuciello, C Natale, S Pirozzi, and L Villani. A conformable force/tactile skin for physical human–robot interaction. *IEEE Robotics and Automation Letters*, 1(1):41–48, 2016.

[43] Gregory E Collins and LJ Buckley. Conductive polymer-coated fabrics for chemical sensing. *Synthetic Metals*, 78(2):93–101, 1996.

[44] Martin D Cooney, Shuichi Nishio, and Hiroshi Ishiguro. Recognizing affection for a touch-based interaction with a humanoid robot. In *IEEE/RSJ International Conference on Intelligent Robots and Systems (IROS), 2012*, pages 1420–1427. IEEE, 2012.

[45] Omar Costilla-Reyes, Patricia Scully, and Krikor B Ozanyan. Deep neural networks for learning spatio-temporal features from tomography sensors. *IEEE Transactions on Industrial Electronics*, 65(1):645–653, 2018.

[46] MJ Da Silva, E Schleicher, and U Hampel. Capacitance wire-mesh sensor for fast measurement of phase fraction distributions. *Measurement Science and Technology*, 18(7):2245, 2007.

[47] Ravinder S Dahiya, Giorgio Metta, Maurizio Valle, and Giulio Sandini. Tactile sensing—from humans to humanoids. *IEEE Transactions on Robotics*, 26(1):1–20, 2010.

[48] Ravinder S Dahiya, Philipp Mittendorfer, Maurizio Valle, Gordon Cheng, and Vladimir J Lumelsky. Directions toward effective utilization of tactile skin: A review. *IEEE Sensors Journal*, 13(11):4121–4138, 2013.

[49] Javad Dargahi and Siamak Najarian. Advances in tactile sensors design/-manufacturing and its impact on robotics applications–a review. *Industrial Robot: An International Journal*, 32(3):268–281, 2005.

[50] D De Rossi, A Della Santa, and A Mazzoldi. Dressware: wearable hardware. *Materials Science and Engineering: C*, 7(1):31–35, 1999.

[51] Danilo De Rossi and Enzo Pasquale Scilingo. Skin-like sensor arrays. *Encyclopedia of Sensors*, 10:1–22, 2006.

[52] Danilo De Rossi, Federico Carpi, Federico Lorussi, R Paradiso, EP Scilingo, and A Tognetti. Electroactive fabrics and wearable man-machine interfaces. *Wearable Electronics and Photonics*, pages 59–80, 2005.

[53] John R Deller Jr, John G Proakis, and John H Hansen. *Discrete time processing of speech signals*. Prentice Hall PTR, 1993.

[54] Eugene Demidenko, Alex Hartov, Nirmal Soni, and Keith D Paulsen. On optimal current patterns for electrical impedance tomography. *IEEE Transactions on Biomedical Engineering*, 52(2):238–248, 2005.

[55] Simone Denei, Fulvio Mastrogiovanni, and Giorgio Cannata. Towards the creation of tactile maps for robots and their use in robot contact motion control. *Robotics and Autonomous Systems*, 63:293–308, 2015.

[56] Thomas G Dietterich. Ensemble methods in machine learning. In *International Workshop on Multiple Classifier Systems*, pages 1–15. Springer, 2000.

[57] Aaron M Dollar, Leif P Jentoft, Jason H Gao, and Robert D Howe. Contact sensing and grasping performance of compliant hands. *Autonomous Robots*, 28(1):65, 2010.

[58] Pedro Domingos. A few useful things to know about machine learning. *Communications of the ACM*, 55(10):78–87, 2012.

[59] Eoghan Dunne, Adam Santorelli, Brian McGinley, Geraldine Leader, Martin O'Halloran, and Emily Porter. Supervised learning classifiers for electrical impedance-based bladder state detection. *Scientific Reports*, 8(5363): 1–12, 2018.

[60] Nebojsa Duric, Peter Littrup, Alex Babkin, David Chambers, Stephen Azevedo, Arkady Kalinin, Roman Pevzner, Mikhail Tokarev, Earle Holsapple, Olsi Rama, et al. Development of ultrasound tomography for breast imaging: Technical assessment. *Medical Physics*, 32(5):1375–1386, 2005.

[61] Marc O Ernst and Martin S Banks. Humans integrate visual and haptic information in a statistically optimal fashion. *Nature*, 415(6870):429, 2002.

[62] Ronald S Fearing. Tactile sensing mechanisms. *The International Journal of Robotics Research*, 9(3):3–23, 1990.

[63] Tiffany Field. *Touch*. MIT press, 2014.

[64] Jerome Friedman, Trevor Hastie, and Robert Tibshirani. *The elements of statistical learning*, volume 1. Springer series in statistics New York, 2001.

[65] Hervé Gagnon, Martin Cousineau, Andy Adler, and Alzbeta E Hartinger. A resistive mesh phantom for assessing the performance of eit systems. *IEEE Transactions on Biomedical Engineering*, 57(9):2257–2266, 2010.

[66] Alberto Gallace and Charles Spence. The science of interpersonal touch: an overview. *Neuroscience & Biobehavioral Reviews*, 34(2):246–259, 2010.

[67] Alberto Gallace and Charles Spence. *In touch with the future: The sense of touch from cognitive neuroscience to virtual reality*. OUP Oxford, 2014.

[68] Alberto Gallace, Hong Z Tan, and Charles Spence. The body surface as a communication system: The state of the art after 50 years. *Presence: Teleoperators and Virtual Environments*, 16(6):655–676, 2007.

[69] Gerard J Gallo and Erik T Thostenson. Spatial damage detection in electrically anisotropic fiber-reinforced composites using carbon nanotube networks. *Composite Structures*, 141:14–23, 2016.

[70] Paolo Gastaldo, Luigi Pinna, Lucia Seminara, Maurizio Valle, and Rodolfo Zunino. A tensor-based approach to touch modality classification by using machine learning. *Robotics and Autonomous Systems*, 63:268–278, 2015.

[71] Francine Gemperle, Chris Kasabach, John Stivoric, Malcolm Bauer, and Richard Martin. Design for wearability. In *Wearable Computers, 1998. Digest of Papers. Second International Symposium on*, pages 116–122. IEEE, 1998.

[72] E Gersing, B Hofmann, and M Osypka. Influence of changing peripheral geometry on electrical impedance tomography measurements. *Medical and Biological Engineering and Computing*, 34(5):359–361, 1996.

[73] David B Geselowitz. An application of electrocardiographic lead theory to impedance plethysmography. *IEEE Transactions on Biomedical Engineering*, BME-18(1):38–41, 1971.

[74] Dirk Goger, Nicolas Gorges, and Heinz Worn. Tactile sensing for an anthropomorphic robotic hand: Hardware and signal processing. In *IEEE International Conference on Robotics and Automation, ICRA 2009.*, pages 895–901. IEEE, 2009.

[75] BM Graham and Andy Adler. Objective selection of hyperparameter for eit. *Physiological Measurement*, 27(5):S65, 2006.

[76] Yair Granot, Antoni Ivorra, and Boris Rubinsky. Frequency-division multiplexing for electrical impedance tomography in biomedical applications. *International Journal of Biomedical Imaging*, 2007, 2007.

[77] RV Gregory, WC Kimbrell, and HH Kuhn. Electrically conductive nonmetallic textile coatings. *Journal of Coated Fabrics*, 20(3):167–175, 1991.

[78] Jayavardhana Gubbi, Rajkumar Buyya, Slaven Marusic, and Marimuthu Palaniswami. Internet of things (iot): A vision, architectural elements, and future directions. *Future Generation Computer Systems*, 29(7):1645–1660, 2013.

[79] Isabelle Guyon, Steve Gunn, Masoud Nikravesh, and Lofti A Zadeh. *Feature extraction: foundations and applications*, volume 207. Springer, 2008.

[80] Eva Håkansson, Andrew Amiet, and Akif Kaynak. Electromagnetic shielding properties of polypyrrole/polyester composites in the 1–18 ghz frequency range. *Synthetic metals*, 156(14-15):917–925, 2006.

[81] Mallory L Hammock, Alex Chortos, Benjamin C-K Tee, Jeffrey B-H Tok, and Zhenan Bao. 25th anniversary article: the evolution of electronic skin (e-skin): a brief history, design considerations, and recent progress. *Advanced Materials*, 25(42):5997–6038, 2013.

[82] Alexander Hartov, Robert A Mazzarese, Fred R Reiss, Todd E Kerner, K Sunshine Osterman, Dinise B Williams, and Keith D Paulsen. A multichannel continuously selectable multifrequency electrical impedance spectroscopy measurement system. *IEEE Transactions on Biomedical Engineering*, 47(1):49–58, 2000.

[83] David S Holder. *Electrical impedance tomography: methods, history and applications*. CRC Press, 2004.

[84] Robert D Howe and Mark R Cutkosky. Integrating tactile sensing with control for dextrous manipulation. In *IEEE International Workshop on Intelligent Motion Control*, pages 369–374, 1990.

[85] Robert D Howe and Mark R Cutkosky. Dynamic tactile sensing: Perception of fine surface features with stress rate sensing. *IEEE Transactions on Robotics and Automation*, 9(2):140–151, 1993.

[86] Chao-Tsung Hsiao, Georges Chahine, and Nail Gumerov. Application of a hybrid genetic/powell algorithm and a boundary element method to electrical impedance tomography. *Journal of Computational Physics*, 173(2): 433–454, 2001.

[87] Jiang Hsieh et al. Computed tomography: principles, design, artifacts, and recent advances. SPIE Bellingham, WA, 2009.

[88] David Isaacson. Distinguishability of conductivities by electric current computed tomography. *IEEE Transactions on Medical Imaging*, 5(2):91–95, 1986.

[89] Bernard Jaffe. *Piezoelectric ceramics*, volume 3. Elsevier, 2012.

[90] Nawid Jamali and Claude Sammut. Majority voting: Material classification by tactile sensing using surface texture. *IEEE Transactions on Robotics*, 27(3):508–521, 2011.

[91] Gareth James, Daniela Witten, Trevor Hastie, and Robert Tibshirani. *An introduction to statistical learning*, volume 112. Springer, 2013.

[92] RS Johansson and G Westling. Roles of glabrous skin receptors and sensorimotor memory in automatic control of precision grip when lifting rougher or more slippery objects. *Experimental Brain Research*, 56(3):550–564, 1984.

[93] Magnus Johnsson and Christian Balkenius. Sense of touch in robots with self-organizing maps. *IEEE Transactions on Robotics*, 27(3):498–507, 2011.

[94] Rhawn Joseph. *Neuropsychiatry, neuropsychology, and clinical neuroscience: Emotion, evolution, cognition, language, memory, brain damage, and abnormal behavior*. Williams & Wilkins Co, 1996.

[95] Simon J Julier and Jeffrey K Uhlmann. New extension of the kalman filter to nonlinear systems. In *Signal processing, sensor fusion, and target recognition VI*, volume 3068, pages 182–194. International Society for Optics and Photonics, 1997.

[96] Yo Kato, Toshiharu Mukai, Tomonori Hayakawa, and Tetsuyoshi Shibata. Tactile sensor without wire and sensing element in the tactile region based on eit method. In *Sensors, 2007 IEEE*, pages 792–795. IEEE, 2007.

[97] Dov Katz, Jacqueline Kenney, and Oliver Brock. How can robots succeed in unstructured environments. In *In Workshop on Robot Manipulation: Intelligence in Human Environments at Robotics: Science and Systems*. Citeseer, 2008.

[98] Haruhisa Kawasaki, Tsuneo Komatsu, and Kazunao Uchiyama. Dexterous anthropomorphic robot hand with distributed tactile sensor: Gifu hand ii. *IEEE/ASME Transactions on Mechatronics*, 7(3):296–303, 2002.

[99] Akif Kaynak, Lijing Wang, Chris Hurren, and Xungai Wang. Characterization of conductive polypyrrole coated wool yarns. *Fibers and Polymers*, 3(1):24–30, 2002.

[100] Oliver Kerpa, Karsten Weiss, and Heinz Worn. Development of a flexible tactile sensor system for a humanoid robot. In *IEEE/RSJ International Conference on Intelligent Robots and Systems, IROS 2003*, volume 1, pages 1–6. IEEE, 2003.

[101] MS Kim, HK Kim, SW Byun, SH Jeong, YK Hong, JS Joo, KT Song, JK Kim, CJ Lee, and JY Lee. Pet fabric/polypyrrole composite with high electrical conductivity for emi shielding. *Synthetic Metals*, 126(2-3):233–239, 2002.

[102] Nikolay V Kirianaki, Sergey Y Yurish, Nestor O Shpak, and Vadim P Deynega. *Data Acquisition and Signal Processing for Smart Sensors*. Wiley Online Library, 2002.

[103] RA Knight and RT Lipczynski. The use of eit techniques to measure interface pressure. In *Proceedings of the 12th Annual International Conference of the IEEE Engineering in Medicine and Biology Society, 1990.*, pages 2307–2308. IEEE, 1990.

[104] V Kolehmainen, M Vauhkonen, PA Karjalainen, and JP Kaipio. Assessment of errors in static electrical impedance tomography with adjacent and trigonometric current patterns. *Physiological Measurement*, 18(4):289, 1997.

[105] Daphne Koller and Nir Friedman. *Probabilistic graphical models: principles and techniques*. MIT press, 2009.

[106] Jelizaveta Konstantinova, Allen Jiang, Kaspar Althoefer, Prokar Dasgupta, and Thrishantha Nanayakkara. Implementation of tactile sensing for palpation in robot-assisted minimally invasive surgery: A review. *IEEE Sensors Journal*, 14(8):2490–2501, 2014.

[107] Hans H Kuhn and William C Kimbrell Jr. Electrically conductive textile materials and method for making same, February 7 1989. US Patent 4,803,096.

[108] Yann LeCun, Yoshua Bengio, and Geoffrey Hinton. Deep learning. *Nature*, 521(7553):436, 2015.

[109] Mark H Lee. Tactile sensing: new directions, new challenges. *The International Journal of Robotics Research*, 19(7):636–643, 2000.

[110] Mark H Lee and Howard R Nicholls. Review article tactile sensing for mechatronics—a state of the art survey. *Mechatronics*, 9(1):1–31, 1999.

[111] Ossi Lehtikangas, Kimmo Karhunen, and Marko Vauhkonen. Reconstruction of velocity fields in electromagnetic flow tomography. *Philosophical Transactions of the Royal Society of London A: Mathematical, Physical and Engineering Sciences*, 374(2070):20150334, 2016.

[112] Li Li, Wai Man Au, Kam Man Wan, Sai Ho Wan, Wai Yee Chung, and Kwok Shing Wong. A resistive network model for conductive knitting stitches. *Textile Research Journal*, 80(10):935–947, 2010.

[113] Zexiang Li, Ping Hsu, and Shankar Sastry. Grasping and coordinated manipulation by a multifingered robot hand. *The International Journal of Robotics Research*, 8(4):33–50, 1989.

[114] Andy Liaw, Matthew Wiener, et al. Classification and regression by randomforest. *R news*, 2(3):18–22, 2002.

[115] Martin Liggins II, David Hall, and James Llinas. *Handbook of multisensor data fusion: theory and practice*. CRC press, 2017.

[116] Tong Lin, Lijing Wang, Xungai Wang, and Akif Kaynak. Polymerising pyrrole on polyester textiles and controlling the conductivity through coating thickness. *Thin Dolid Films*, 479(1-2):77–82, 2005.

[117] William RB Lionheart. Developments in eit reconstruction algorithms. Technical report, 2003.

[118] William RB Lionheart. Eit reconstruction algorithms: pitfalls, challenges and recent developments. *Physiological Measurement*, 25(1):125, 2004.

[119] Darren J Lipomi, Benjamin C-K Tee, Michael Vosgueritchian, and Zhenan Bao. Stretchable organic solar cells. *Advanced Materials*, 23(15):1771–1775, 2011.

[120] Hongbin Liu, Juan Greco, Xiaojing Song, Joao Bimbo, Lakmal Seneviratne, and Kaspar Althoefer. Tactile image based contact shape recognition using neural network. In *IEEE Conference on Multisensor Fusion and Integration for Intelligent Systems (MFI), 2012*, pages 138–143. IEEE, 2012.

[121] Huan Liu and Hiroshi Motoda. *Feature extraction, construction and selection: A data mining perspective*, volume 453. Springer Science & Business Media, 1998.

[122] Huaping Liu, Yuanlong Yu, Fuchun Sun, and Jason Gu. Visual–tactile fusion for object recognition. *IEEE Transactions on Automation Science and Engineering*, 14(2):996–1008, 2017.

[123] Andrew Craig Long. *Design and manufacture of textile composites*. Elsevier, 2005.

[124] José Miguel López-Higuera. *Handbook of optical fibre sensing technology*. Wiley, 2002.

[125] David G Lowe. Distinctive image features from scale-invariant keypoints. *International journal of computer vision*, 60(2):91–110, 2004.

[126] Vladimir J Lumelsky. *Sensing, intelligence, motion: how robots and humans move in an unstructured world*. John Wiley & Sons, 2005.

[127] Ren C. Luo. Guest editorial. *IEEE Transactions on Industrial Electronics*, 43(3):345–, June 1996. ISSN 0278-0046. doi: 10.1109/TIE.1996.499805.

[128] Shan Luo, Wenxuan Mou, Kaspar Althoefer, and Hongbin Liu. Novel tactile-sift descriptor for object shape recognition. *IEEE Sensors Journal*, 15(9):5001–5009, 2015.

[129] Lu Ma, Andy Hunt, and Manuchehr Soleimani. Experimental evaluation of conductive flow imaging using magnetic induction tomography. *International Journal of Multiphase Flow*, 72:198–209, 2015.

[130] Emma Malone, Markus Jehl, Simon Arridge, Timo Betcke, and David Holder. Stroke type differentiation using spectrally constrained multifrequency eit: evaluation of feasibility in a realistic head model. *Physiological Measurement*, 35(6):1051, 2014.

[131] Steve Mann. Wearable computing: A first step toward personal imaging. *Computer*, 30(2):25–32, 1997.

[132] Stefan CB Mannsfeld, Benjamin CK Tee, Randall M Stoltenberg, Christopher V HH Chen, Soumendra Barman, Beinn VO Muir, Anatoliy N Sokolov, Colin Reese, and Zhenan Bao. Highly sensitive flexible pressure sensors with microstructured rubber dielectric layers. *Nature materials*, 9(10):859, 2010.

[133] James Manyika, Michael Chui, Brad Brown, Jacques Bughin, Richard Dobbs, Charles Roxburgh, and Angela H Byers. Big data: The next frontier for innovation, competition, and productivity. 2011.

[134] Sébastien Martin and Charles TM Choi. Nonlinear electrical impedance tomography reconstruction using artificial neural networks and particle swarm optimization. *IEEE Transactions on Magnetics*, 52(3):1–4, 2016.

[135] Sébastien Martin and Charles TM Choi. A novel post-processing scheme for two-dimensional electrical impedance tomography based on artificial neural networks. *PloS One*, 12(12):e0188993, 2017.

[136] Jan Meyer, Paul Lukowicz, and Gerhard Troster. Textile pressure sensor for muscle activity and motion detection. In *10th IEEE International Symposium on Wearable Computers, 2006*, pages 69–72. IEEE, 2006.

[137] Philipp Mittendorfer and Gordon Cheng. Humanoid multimodal tactile-sensing modules. *IEEE Transactions on Robotics*, 27(3):401–410, 2011.

[138] Philipp Mittendorfer and Gordon Cheng. Integrating discrete force cells into multi-modal artificial skin. In *12th IEEE-RAS International Conference on Humanoid Robots (Humanoids), 2012*, pages 847–852. IEEE, 2012.

[139] Philipp Mittendorfer, Emmanuel Dean, and Gordon Cheng. 3d spatial self-organization of a modular artificial skin. In *IEEE/RSJ International Conference on Intelligent Robots and Systems IROS 2014.*, pages 3969–3974. IEEE, 2014.

[140] J Mohamad-Saleh and BS Hoyle. Determination of multi-component flow process parameters based on electrical capacitance tomography data using artificial neural networks. *Measurement Science and Technology*, 13(12): 1815, 2002.

[141] Toshiharu Mukai, Masaki Onishi, Tadashi Odashima, Shinya Hirano, and Zhiwei Luo. Development of the tactile sensor system of a human-interactive robot "ri-man". *IEEE Transactions on Robotics*, 24(2):505–512, 2008.

[142] Kouji Murakami, Kazuya Matsuo, Tsutomu Hasegawa, and Ryo Kurazume. A decision method for placement of tactile elements on a sensor glove for the recognition of grasp types. *IEEE/ASME Transactions on Mechatronics*, 15(1):157–162, 2010.

[143] K Murphy. Machine learning: a probabilistic approach. *Massachusetts Institute of Technology*, pages 1–21, 2012.

[144] Akihiko Nagakubo, Hassan Alirezaei, and Yasuo Kuniyoshi. A deformable and deformation sensitive tactile distribution sensor. In *IEEE International Conference on Robotics and Biomimetics, ROBIO 2007*, pages 1301–1308. IEEE, 2007.

[145] Anish S Naidu, Rajni V Patel, and Michael D Naish. Low-cost disposable tactile sensors for palpation in minimally invasive surgery. *IEEE/ASME Transactions on Mechatronics*, 22(1):127–137, 2017.

[146] Alamgir Naushad, Ahmar Rashid, and Suleman Mazhar. Analysing the performance of eit images using the point spread function. In *International*

Conference on Emerging Technologies (ICET), 2014, pages 36–41. IEEE, 2014.

[147] Martin Nilsson. Tactile sensors and other distributed sensors with minimal wiring complexity. *IEEE/ASME transactions on mechatronics*, 5(3):253–257, 2000.

[148] Ziad Obermeyer and Ezekiel J Emanuel. Predicting the future—big data, machine learning, and clinical medicine. *The New England Journal of Medicine*, 375(13):1216, 2016.

[149] Yoshiyuki Ohmura, Yasuo Kuniyoshi, and Akihiko Nagakubo. Conformable and scalable tactile sensor skin for curved surfaces. In *Proceedings IEEE International Conference on Robotics and Automation, ICRA 2006.*, pages 1348–1353. IEEE, 2006.

[150] Nurhan Onar, Aysun Cireli Akşit, M Faruk Ebeoglugil, Isil Birlik, Erdal Celik, and Ismail Ozdemir. Structural, electrical, and electromagnetic properties of cotton fabrics coated with polyaniline and polypyrrole. *Journal of Applied Polymer Science*, 114(4):2003–2010, 2009.

[151] Keat Ghee Ong, Mahaveer K Jain, Casey Mungle, Stefan Schmidt, and Craig A Grimes. Magnetism-based sensors. In *Complex Mediums II: Beyond Linear Isotropic Dielectrics*, volume 4467, pages 158–173. International Society for Optics and Photonics, 2001.

[152] Makoto Ono, Buntarou Shizuki, and Jiro Tanaka. Touch & activate: adding interactivity to existing objects using active acoustic sensing. In *Proceedings of the 26th annual ACM Symposium on User Interface Software and Technology*, pages 31–40. ACM, 2013.

[153] Kenneth Jackson Overton. The acquisition, processing, and use of tactile sensor data in robot control. 1984.

[154] Lijia Pan, Alex Chortos, Guihua Yu, Yaqun Wang, Scott Isaacson, Ranulfo Allen, Yi Shi, Reinhold Dauskardt, and Zhenan Bao. An ultra-sensitive resistive pressure sensor based on hollow-sphere microstructure induced elasticity in conducting polymer film. *Nature communications*, 5:3002, 2014.

[155] Florian Pantke and Stefan Bosse. An artificial intelligence approach towards sensorial materials.

[156] Steve Park, Hyunjin Kim, Michael Vosgueritchian, Sangmo Cheon, Hyeok Kim, Ja Hoon Koo, Taeho Roy Kim, Sanghyo Lee, Gregory Schwartz, Hyuk Chang, et al. Stretchable energy-harvesting tactile electronic skin capable of differentiating multiple mechanical stimuli modes. *Advanced Materials*, 26(43):7324–7332, 2014.

[157] A Persichetti, F Vecchi, and MC Carrozza. Optoelectronic-based flexible contact sensor for prosthetic hand application. In *Rehabilitation Robotics, 2007. ICORR 2007. IEEE 10th International Conference on*, pages 415–420. IEEE, 2007.

[158] Anna Petrovskaya, Oussama Khatib, Sebastian Thrun, and Andrew Y Ng. Bayesian estimation for autonomous object manipulation based on tactile sensors. In *Proceedings IEEE International Conference on Robotics and Automation, ICRA 2006.*, pages 707–714. IEEE, 2006.

[159] Bernd J Pichler, Hans F Wehrl, Armin Kolb, and Martin S Judenhofer. Positron emission tomography/magnetic resonance imaging: the next generation of multimodality imaging? In *Seminars in Nuclear Medicine*, volume 38, pages 199–208. Elsevier, 2008.

[160] Nick Polydorides and William RB Lionheart. A matlab toolkit for three-dimensional electrical impedance tomography: a contribution to the electrical impedance and diffuse optical reconstruction software project. *Measurement Science and Technology*, 13(12):1871, 2002.

[161] Ivan Poupyrev, Chris Harrison, and Munehiko Sato. Touché: touch and gesture sensing for the real world. In *Proceedings of the 2012 ACM Conference on Ubiquitous Computing*, pages 536–536. ACM, 2012.

[162] Ivan Poupyrev, Nan-Wei Gong, Shiho Fukuhara, Mustafa Emre Karagozler, Carsten Schwesig, and Karen E Robinson. Project jacquard: interactive digital textiles at scale. In *Proceedings of the 2016 CHI Conference on Human Factors in Computing Systems*, pages 4216–4227. ACM, 2016.

[163] M Prato and L Zanni. Inverse problems in machine learning: an application to brain activity interpretation. *Journal of Physics: Conference Series*, 135 (1):012085, 2008.

[164] Halley P Profita, James Clawson, Scott Gilliland, Clint Zeagler, Thad Starner, Jim Budd, and Ellen Yi-Luen Do. Don't mind me touching my wrist: a case study of interacting with on-body technology in public. In *Proceedings of the 2013 International Symposium on Wearable Computers*, pages 89–96. ACM, 2013.

[165] Robert Puers. Capacitive sensors: when and how to use them. *Sensors and Actuators A: Physical*, 37:93–105, 1993.

[166] Ganna Pugach, Alexandre Pitti, and Philippe Gaussier. Neural learning of the topographic tactile sensory information of an artificial skin through a self-organizing map. *Advanced Robotics*, 29(21):1393–1409, 2015.

[167] Payam Refaeilzadeh, Lei Tang, and Huan Liu. Cross-validation. In *Encyclopedia of Database Systems*, pages 532–538. Springer, 2009.

[168] Christian Robert. Machine learning, a probabilistic perspective, 2014.

[169] Stefania Russo, Tommaso Ranzani, Hongbin Liu, Samia Nefti-Meziani, Kaspar Althoefer, and Arianna Menciassi. Soft and stretchable sensor using biocompatible electrodes and liquid for medical applications. *Soft Robotics*, 2(4):146–154, 2015.

[170] Stefania Russo, Nicola Carbonaro, Alessandro Tognetti, and Samia Nefti-Meziani. A quantitative evaluation of drive patterns in electrical impedance tomography. In *International Conference on Wireless Mobile Communication and Healthcare*, pages 337–344. Springer, 2016.

[171] Stefania Russo, Samia-Nefti Meziani, Tauseef Gulrez, Nicola Carbonaro, and Alessandro Tognetti. Towards the development of an eit-based stretchable sensor for multi-touch industrial human-computer interaction systems. In *International Conference on Cross-Cultural Design*, pages 563–573. Springer, 2016.

[172] Stefania Russo, Samia Nefti-Meziani, Nicola Carbonaro, and Alessandro Tognetti. Development of a high-speed current injection and voltage measurement system for electrical impedance tomography-based stretchable sensors. *Technologies*, 5(3):48, 2017.

[173] Stefania Russo, Samia Nefti-Meziani, Nicola Carbonaro, and Alessandro Tognetti. A quantitative evaluation of drive pattern selection for optimizing eit-based stretchable sensors. *Sensors*, 17(9):1999, 2017.

[174] Fadil Santosa and Michael Vogelius. A backprojection algorithm for electrical impedance imaging. *SIAM Journal on Applied Mathematics*, 50(1): 216–243, 1990.

[175] Gary J Saulnier. Eit instrumentation. *Electrical Impedance Tomography: Methods, History and Applications*, pages 65–104, 2005.

[176] Andrew Schmeder and Adrian Freed. Support vector machine learning for gesture signal estimation with a piezo-resistive fabric touch surface. In *NIME*, pages 244–249, 2010.

[177] Alexander Schmitz, Perla Maiolino, Marco Maggiali, Lorenzo Natale, Giorgio Cannata, and Giorgio Metta. Methods and technologies for the implementation of large-scale robot tactile sensors. *IEEE Transactions on Robotics*, 27(3):389–400, 2011.

[178] Alexander Schneider, Jürgen Sturm, Cyrill Stachniss, Marco Reisert, Hans Burkhardt, and Wolfram Burgard. Object identification with tactile sensors using bag-of-features. In *Intelligent Robots and Systems, 2009. IROS 2009. IEEE/RSJ International Conference on*, pages 243–248. IEEE, 2009.

[179] Andrew Donald Seagar. *Probing with low frequency electric currents.* PhD thesis, University of Canterbury. Department of Electrical Engineering, 1983.

[180] Tsuyoshi Sekitani, Ute Zschieschang, Hagen Klauk, and Takao Someya. Flexible organic transistors and circuits with extreme bending stability. *Nature Materials*, 9(12):1015, 2010.

[181] Serguei Semenov. Microwave tomography: review of the progress towards clinical applications. *Philosophical Transactions of the Royal Society of London A: Mathematical, Physical and Engineering Sciences*, 367(1900): 3021–3042, 2009.

[182] Lucia Seminara, Luigi Pinna, Ali Ibrahim, Luca Noli, Stefano Caviglia, Paolo Gastaldo, and Maurizio Valle. Towards integrating intelligence in electronic skin. *Mechatronics*, 34:84–94, 2016.

[183] DH Sheingold. Impedance & admittance transformations using operational amplifiers. *Lightning Empiricist*, 12(1):1–8, 1964.

[184] Xuetao Shi, Xiuzhen Dong, Wanjun Shuai, Fusheng You, Feng Fu, and Ruigang Liu. Pseudo-polar drive patterns for brain electrical impedance tomography. *Physiological Measurement*, 27(11):1071, 2006.

[185] Lin Shu, Tao Hua, Yangyong Wang, Qiao Li, David Dagan Feng, and Xiaoming Tao. In-shoe plantar pressure measurement and analysis system based on fabric pressure sensing array. *IEEE Transactions on Information Technology in Biomedicine*, 14(3):767–775, 2010.

[186] David Silvera Tawil, David Rye, and Mari Velonaki. Interpretation of the modality of touch on an artificial arm covered with an eit-based sensitive skin. *The International Journal of Robotics Research*, 31(13):1627–1641, 2012.

[187] David Silvera-Tawil, David Rye, Manuchehr Soleimani, and Mari Velonaki. Electrical impedance tomography for artificial sensitive robotic skin: a review. *IEEE Sensors Journal*, 15(4):2001–2016, 2015.

[188] David Silvera-Tawil, David Rye, and Mari Velonaki. Artificial skin and tactile sensing for socially interactive robots: A review. *Robotics and Autonomous Systems*, 63:230–243, 2015.

[189] Robert WM Smith, Ian Leslie Freeston, and Brian Hilton Brown. A real-time electrical impedance tomography system for clinical use-design and preliminary results. *IEEE Transactions on Biomedical Engineering*, 42(2): 133–140, 1995.

[190] Jae S Son, Mark R Cutkosky, and Robert D Howe. Comparison of contact sensor localization abilities during manipulation. *Robotics and autonomous systems*, 17(4):217–233, 1996.

[191] Charles Spence and Alberto Gallace. Recent developments in the study of tactile attention. *Canadian Journal of Experimental Psychology/Revue canadienne de psychologie expérimentale*, 61(3):196, 2007.

[192] Matteo Stoppa and Alessandro Chiolerio. Wearable electronics and smart textiles: a critical review. *Sensors*, 14(7):11957–11992, 2014.

[193] Fuchun Sun, Chunfang Liu, Wenbing Huang, and Jianwei Zhang. Object classification and grasp planning using visual and tactile sensing. *IEEE Transactions on Systems, Man, and Cybernetics: Systems*, 46(7):969–979, 2016.

[194] Z Suo, EY Ma, H Gleskova, and S Wagner. Mechanics of rollable and foldable film-on-foil electronics. *Applied Physics Letters*, 74(8):1177–1179, 1999.

[195] Felix Sygulla, Felix Ellensohn, Arne-Christoph Hildebrandt, Daniel Wahrmann, and Daniel Rixen. A flexible and low-cost tactile sensor for robotic applications. In *Advanced Intelligent Mechatronics (AIM), 2017 IEEE International Conference on*, pages 58–63. IEEE, 2017.

[196] TN Tallman, S Gungor, KW Wang, and CE Bakis. Damage detection and conductivity evolution in carbon nanofiber epoxy via electrical impedance tomography. *Smart Materials and Structures*, 23(4):045034, 2014.

[197] Mami Tanaka. Development of tactile sensor for monitoring skin conditions. *Journal of Materials Processing Technology*, 108(2):253–256, 2001.

[198] Mengxing Tang, Wei Wang, James Wheeler, Malcolm McCormick, and Xiuzhen Dong. The number of electrodes and basis functions in eit image reconstruction. *Physiological Measurement*, 23(1):129, 2002.

[199] Mika Tarvainen, Marko Vauhkonen, Tuomo Savolainen, and Jari P Kaipio. Boundary element method and internal electrodes in electrical impedance tomography. *International Journal for Numerical Methods in Engineering*, 50(4):809–824, 2001.

[200] David Silvera Tawil. *Artificial skin and the interpretation of touch for human-robot interaction*. PhD thesis, School Aerosp., Mech. Mechatron., Univ. Sydney, New South Wales, Australia, 2012.

[201] David Silvera Tawil, David Rye, and Mari Velonaki. Improved image reconstruction for an eit-based sensitive skin with multiple internal electrodes. *IEEE Transactions on Robotics*, 27(3):425–435, 2011.

[202] AT Tidswell, Adam Gibson, RH Bayford, and David S Holder. Electrical impedance tomography of human brain activity with a two-dimensional ring of scalp electrodes. *Physiological Measurement*, 22(1):167, 2001.

[203] M Tokarska, M Frydrysiak, and J Zieba. Electrical properties of flat textile material as inhomegeneous and anisotropic structure. *Journal of Materials Science: Materials in Electronics*, 24(12):5061–5068, 2013.

[204] Tito Pradhono Tomo, Sophon Somlor, Alexander Schmitz, Lorenzo Jamone, Weijie Huang, Harris Kristanto, and Shigeki Sugano. Design and characterization of a three-axis hall effect-based soft skin sensor. *Sensors*, 16(4): 491, 2016.

[205] Robert A van den Berg, Huub CJ Hoefsloot, Johan A Westerhuis, Age K Smilde, and Mariët J van der Werf. Centering, scaling, and transformations: improving the biological information content of metabolomics data. *BMC genomics*, 7(1):142, 2006.

[206] Alessio Varesano, Lorenzo Dall'Acqua, and Claudio Tonin. A study on the electrical conductivity decay of polypyrrole coated wool textiles. *Polymer Degradation and Stability*, 89(1):125–132, 2005.

[207] Marko Vauhkonen, Pasi A Karjalainen, and Jari P Kaipio. A kalman filter approach to track fast impedance changes in electrical impedance tomography. *IEEE Transactions on Biomedical Engineering*, 45(4):486–493, 1998.

[208] D Vogt, Yigit Menguc, Yong-Lae Park, Michael Wehner, RK Kramer, Carmel Majidi, LP Jentoft, Yaroslav Tenzer, RD Howe, and Robert J Wood. Progress in soft, flexible, and stretchable sensing systems. In *Proceedings of the International Workshop on Research Frontiers in Electronics Skin Technology at ICRA*, volume 13, 2013.

[209] Hongbo Wang, Greg de Boer, Junwai Kow, Ali Alazmani, Mazdak Ghajari, Robert Hewson, and Peter Culmer. Design methodology for magnetic field-based soft tri-axis tactile sensors. *Sensors*, 16(9):1356, 2016.

[210] Ernst Heinrich Weber. *EH Weber: The sense of touch.* Academic Pr, 1978.

[211] Rolf H Weber and Romana Weber. *Internet of things*, volume 12. Springer, 2010.

[212] John G Webster and Halit Eren. *Measurement, instrumentation, and sensors handbook: spatial, mechanical, thermal, and radiation measurement.* CRC press, 2017.

[213] Mark Weiser. The computer for the 21st century. *Mobile Computing and Communications Review*, 3(3):3–11, 1999.

[214] Andrew J Wilkinson, EW Randall, JJ Cilliers, DR Durrett, T Naidoo, and T Long. A 1000-measurement frames/second ert data capture system with real-time visualization. *IEEE Sensors Journal*, 5(2):300–307, 2005.

[215] Ian H Witten, Eibe Frank, Mark A Hall, and Christopher J Pal. *Data Mining: Practical machine learning tools and techniques*. Morgan Kaufmann, 2016.

[216] Eung Je Woo, Ping Hua, John G Webster, and Willis J Tompkins. A robust image reconstruction algorithm and its parallel implementation in electrical impedance tomography. *IEEE Transactions on Medical Imaging*, 12(2):137–146, 1993.

[217] Robert Xiao, Chris Harrison, and Scott E Hudson. Worldkit: rapid and easy creation of ad-hoc interactive applications on everyday surfaces. In *Proceedings of the SIGCHI Conference on Human Factors in Computing Systems*, pages 879–888. ACM, 2013.

[218] Canhua Xu, Xiuzhen Dong, Xuetao Shi, Feng Fu, Wanjun Shuai, Ruigang Liu, and Fusheng You. Comparison of drive patterns for single current source eit in computational phantom. In *Bioinformatics and Biomedical Engineering, 2008. ICBBE 2008. The 2nd International Conference on*, pages 1500–1503. IEEE, 2008.

[219] A Yao and Manuchehr Soleimani. A pressure mapping imaging device based on electrical impedance tomography of conductive fabrics. *Sensor Review*, 32(4):310–317, 2012.

[220] Mamatjan Yasin, Stephan Böhm, Pascal O Gaggero, and Andy Adler. Evaluation of eit system performance. *Physiological Measurement*, 32(7):851, 2011.

[221] Sang Ho Yoon, Ke Huo, Yunbo Zhang, Guiming Chen, Luis Paredes, Subramanian Chidambaram, and Karthik Ramani. isoft: A customizable soft sensor with real-time continuous contact and stretching sensing. In *Proceedings of the 30th Annual ACM Symposium on User Interface Software and Technology*, pages 665–678. ACM, 2017.

[222] Thomas J Yorkey, John G Webster, and Willis J Tompkins. Comparing reconstruction algorithms for electrical impedance tomography. *IEEE Transactions on Biomedical Engineering*, BME-34(11):843–852, 1987.

[223] Guoqiang Zhang, B Eddy Patuwo, and Michael Y Hu. Forecasting with artificial neural networks:: The state of the art. *International Journal of Forecasting*, 14(1):35–62, 1998.

[224] Hui Zhang, Xiaoming Tao, Tongxi Yu, and Shanyuan Wang. Conductive knitted fabric as large-strain gauge under high temperature. *Sensors and Actuators A: Physical*, 126(1):129–140, 2006.

[225] Li Zhang and Jeffrey C Trinkle. The application of particle filtering to grasping acquisition with visual occlusion and tactile sensing. In *IEEE International Conference on Robotics and Automation (ICRA), 2012*, pages 3805–3812. IEEE, 2012.

[226] Yang Zhang and Chris Harrison. Tomo: Wearable, low-cost electrical impedance tomography for hand gesture recognition. In *Proceedings of the 28th Annual ACM Symposium on User Interface Software & Technology*, pages 167–173. ACM, 2015.

[227] Yang Zhang, Gierad Laput, and Chris Harrison. Electrick: Low-cost touch sensing using electric field tomography. In *Proceedings of the 2017 CHI Conference on Human Factors in Computing Systems*, pages 1–14. ACM, 2017.

[228] Qingsheng Zhu, WRB Lionheart, FJ Lidgey, CN McLeod, KS Paulson, and MK Pidcock. An adaptive current tomograph using voltage sources. *IEEE Transactions on Biomedical Engineering*, 40(2):163–168, 1993.